From Waveforms to Source: Applications of Finite-Fault Modeling in Earthquake Characterization and Early Warning Systems

by

Margarita M. Solares-Colón

A dissertation accepted and approved in partial fulfillment of the

requirements for the degree of

Doctor of Philosophy

in Earth Sciences

Dissertation Committee:

Diego Melgar, Chair

Brittany Erickson, Core Member

Valerie Sahakian, Core Member

Ben Farr, Institutional Representative

University of Oregon

Fall 2025

DISSERTATION ABSTRACT

Margarita M. Solares-Colón

Doctor of Philosophy in Earth Sciences

Title: From Waveform to Source: Applications of Finite-Fault Modeling in Earthquake Characterization and Early Warning Systems

This dissertation centers on source characterization of moderate to large earthquakes. We investigate how modeling and inversion techniques can be used to extract information about earthquake properties. One approach involves the use of finite-fault models, which provide estimates of slip distribution and insight into the spatial and temporal evolution of ruptures. Advancements in technology and modeling approaches have lowered the threshold for resolving smaller earthquakes in greater detail with the use of geodetic observations as complement to seismological inversions. This dissertation focuses on seismogeodetic techniques, integrating geodetic observations (GNSS continuous and static offsets, and InSAR observations), with seismic data to better characterize earthquake sources. First, we present a joint inversion model of a moderate earthquake (**M**6.4) using a nonlinear approach that allows for a more detailed characterization of the rupture process and resolve source parameters typically simplified in linearized models. As more finite-fault models are compiled, we can develop a catalog from which general patterns of earthquake behavior can be inferred. This leads to the second component of the dissertation, which builds on a finite-fault model database to revisit assumptions about source scaling, from general trends to local (subfault) scale. By understanding these patterns, we can contribute to the development of more sophisticated tools—such as modern earthquake early warning systems—that support faster, more effective responses. This forms the final component of the dissertation, in which we generate synthetic waveforms from rupture scenarios produced by an earthquake cycle simulator to test the performance of geodetic early warning system. Ultimately, the goal of this dissertation is to improve our understanding of earthquake processes and hazards so that we can enhance preparedness and response efforts, with the overarching aim of reducing risk and saving lives.

This dissertation includes previously published and unpublished co-authored material.

CURRICULUM VITAE

NAME OF AUTHOR: Margarita M. Solares-Colón

GRADUATE AND UNDERGRADUATE SCHOOLS ATTENDED:

University of Oregon, Eugene, OR, USA
University of Puerto Rico, Mayagüez, PR
University of Puerto Rico, Río Piedras, PR

DEGREES AWARDED:

Doctor of Philosophy in Earth Sciences, 2025, University of Oregon
Master of Science in Geology, 2019, University of Puerto Rico, Mayagüez Campus
Bachelor of Arts in Physical Geography and Technological Applications, 2012, University of Puerto Rico, Río Piedras Campus

AREAS OF SPECIAL INTEREST:

Seismology
Geodesy
Earthquake and Tsunami Hazards
Earthquake Early Warning

PROFESSIONAL EXPERIENCE:

Pathways Intern, U.S. Geological Survey Geologic Hazards Science Center, 2022-2023

Research Assistant I, Puerto Rico Seismic Network, 2019-2021

GRANTS, AWARDS, AND HONORS:

Henry V. Howe Scholarship, University of Oregon Graduate School, 2024-2025

Johnston Scholarship, University of Oregon Department of Earth Sciences, 2022

Promising Scholar Award, University of Oregon Graduate School, 2021

PUBLICATIONS:

Solares-Colón, M. M., & Melgar, D. (202X). Earthquakes source scaling at subfault scale. *Manuscript in preparation.*

Solares-Colón, M. M., Melgar, D., Howell, A., Crowell, B., D'Anastasio, E., Caballero, E., & Fry, B. (2025). Using ruptures from earthquake cycle simulators to test geodetic early warning systems performance. *Seismica*, 2025. *Manuscript accepted for publication, below is the link to preprint.* https://doi.org/10.31223/X53J0V

Solares-Colón, M. M., Goldberg, D. E., Melgar, D., Vanacore, E. A., Sahakian, V. J., & Yeck, W. L., F. Hernández, & A. M. López-Venegas (2025). Slow rupture, long rise times, and multi-fault geometry: The 2020 M6.4 southwestern Puerto Rico mainshock. *Geophysical Research Letters*, 52, e2024GL109740. https://doi.org/10.1029/2024GL109740

López-Venegas, A. M., Mattioli, G. S., **Solares-Colón, M. M.,** Mencin, D., & Jansma, P. E. (2023). Estimating coseismic deformation of southwestern Puerto Rico from the 7 January 2020 Mw 6.4 earthquake: Constraints from campaign and continuous GPS. *Bulletin of the Seismological Society of America*, 113(1), 99–114. https://doi.org/10.1785/0120220115

ACKNOWLEDGMENTS

First, I wish to express my gratitude to my advisor, Diego Melgar, who has been instrumental in my academic formation and personal growth. I would not have made this far without his guidance, endless support, and inspiring example that reminds us we are more than scientists—that our work should be done with purpose and with impact. I also want to extend my gratitude to Valerie Sahakian and Brittany Erickson, whom I admire and look up to as women in science, for both your character and your scientific excellence. You are also both an inspiration. I also want to thank Ben Farr for being part of my committee and generously sharing his time and advice. As for my external collaborations, I would like to acknowledge Dara Goldberg, who at times felt like a co-advisor, along with William Yeck and Harley Benz, for their support that left an everlasting impact on me, helped me grow as a researcher, and made my summers in Golden truly memorable. I could not forget my international collaborators in New Zealand, or the many mixed time zones we worked across to make meetings happen. I enjoyed working with you all and learned so much. I specially thank Elisabetta D'Anstacio and Andrew Howell, with whom I worked more closely, for your support and valuable feedback. Finally, Brendan Crowell, my away/conference advisor and soon postdoctoral advisor, thank you for your support and encouragement as I take this next step. And of course, my family, friends, emotional support Ñaqui and Petit-pous—thank you for your unconditional support through the years and beyond my doctoral journey, for keeping me grounded and being there through every moment. I also cannot forget my lab members for their genuine feedback and all the discussions during our group meetings, and Marla Trox, our department's North Star who looks after all of us. This work would not have been possible without all of you, and to our natural lab, Earth, thank you.

DEDICATION

To the Big Bang.

TABLE OF CONTENTS

LIST OF FIGURES

Figure Page

LIST OF TABLES

Table Page

CHAPTER 1

INTRODUCTION

Earthquake! Do you know what to do? Drop, cover, and hold on. This simple phrase has become a widely adopted safety message, central to public education efforts aimed at promoting protective action during ground shaking. Effective earthquake preparedness begins well before a fault ruptures, generating seismic waves that travel through the Earth and produce the shaking we feel at the surface. During a traditional earthquake response, monitoring agencies initiate a series of workflows once an event is detected, either by seismic instrumentation or through local reports of felt shaking. The process begins with an automatic detection (seconds) to preliminary report (minutes), which includes an initial estimate of the earthquake's location, magnitude, and origin time, and continues with updated reports as additional data become available (tens of minutes to hours). In some cases, for offshore events that exceed specific magnitude and depth thresholds, tsunami warnings may also be issued as part of the response protocol. Therefore, every second counts as the monitoring agencies work to disseminate information as quickly and accurately as possible to the public and emergency management officials.

Understanding the physical processes behind earthquakes—how faults break, how ruptures evolve, and where strong ground motions are expected—is essential not only for the response part, but also for the development of more accurate hazard assessments and early warning systems. While model uncertainties remain, integrating multiple data source observations and analysis allows us to build a more comprehensive picture of seismic hazards and the seismotectonic behavior of a region, but requires more time (months to years). From waveforms to source and back, this dissertation focuses on earthquake source characterization, explores relationships between source parameters in earthquake modeling, and considers how these insights can be used to simulate rupture scenarios for testing performance of early earthquake algorithm.

1.1 Earthquake Source Characterization

By inverting earthquake observations, we estimate the spatial distribution of slip across the fault plane, resulting in what is known as a finite-fault model. While earthquakes are often simplified as point sources, the actual rupture process involves slip distributed over a finite area of the fault plane. The objective is to improve our understanding of earthquake evolution and propagation to better constrain rupture behavior in modeling. A fundamental challenge is that the fault cannot be directly observed during rupture; instead, we rely on seismic and geodetic observations to infer the underlying source process. As a result, the inversion is inherently non-unique and subject to uncertainty. Still, these models represent our best attempt to interpret rupture behavior and improve our understanding of future earthquake scenarios.

In Chapter 2, I present a refined slip model of the **M**6.4 mainshock that occurred on 7 January 2020 during the southwestern Puerto Rico seismic sequence. This work has been published previously and was a collaboration with the U. S. Geological Survey's (USGS) National Earthquake Information Center (NEIC) and the Puerto Rico Seismic Network. At the time of the mainshock rupture, I was working at the Puerto Rico Seismic Network (PRSN), where I witnessed the event firsthand. This experience triggered my interest in seismic network operations and earthquake response. Later during my internship at the NEIC, I had the opportunity to model the mainshock using the Wavelet and Simulated Annealing Slip (WASP) code for finite-fault modeling. WASP is an upgraded version of the NEIC finite-fault modeling code that now incorporates regional observations and used to produce the finite-fault database analyzed in Chapter 3.

The **M**6.4 mainshock was one of the most impactful modern earthquakes in the northeastern Caribbean that caused significant damage and felt across the Island. Due to its offshore location and a complex distribution of aftershocks make the rupture kinematics of this event challenging to resolve. The sequence illuminated a set of previously unrecognized structures, suggesting that multiple fault segments may have ruptured during the mainshock. To better constrain the rupture process, we perform a joint inversion of seismic and geodetic data to estimate the finite slip distribution of the mainshock and evaluate a multi-segment, yet geologically plausible, fault geometry. The resulting model reveals a lower rupture velocity and longer rise times than typical for an event of this magnitude, pointing to a slow-evolving rupture process with characteristics reminiscent of tsunami earthquakes. Although this normal/strike-slip event did not generate a tsunami, the slow rupture behavior may have important implications for future seismic hazard assessment and earthquake monitoring efforts in southwestern Puerto Rico.

1.2 Source Parameters Scaling

Finite-fault models provide a means of extracting information about earthquake source properties, contributing to our understanding of rupture processes. For decades, seismologists have sought to relate kinematic source parameters—such as slip, rupture dimensions, rupture velocity, and rise time—to earthquake size. These efforts to characterize earthquake physics are, to some extent, aimed at assessing the predictability of rupture behavior. However, establishing scaling laws for earthquakes is challenging as kinematic models are often produced with heterogenous methodologies and datasets. This makes the synthesis of general behaviors ambiguous. In Chapter 3, we build on that foundation by analyzing the global NEIC finite-fault database to investigate scaling relationships among source parameters, which in turn enable their use in rupture simulations and early warning applications. These latter topics are explored in greater detail in Chapter 4 of this dissertation.

The global NEIC finite-fault database dates to the 1990s and is produced using a consistent methodology. Historically, these models were generated using teleseismic data alone, but in recent years, regional observations have also been integrated. As the number of finite-fault models has grown to include a broader range of earthquake sizes and data types, we build on earlier work to revisit assumptions about general patterns of rupture behavior and improve our understanding of earthquake processes. However, capturing these relationships requires simplifying the complexity of rupture physics. One widely used framework is self-similar scaling, which assumes that the geometric and kinematic properties of earthquakes scale proportionally with event size—a concept rooted in fractal and chaos theory. Although we find that self-similarity is largely preserved, deviations do emerge, and the noise and scatter in the data could provide additional insight into rupture dynamics. We further analyze this systematic catalog at the local scale, as these details are critical for understanding and simulating realistic earthquake ruptures.

1.3 Earthquake Simulations and Waveform Generation

Large earthquakes are less frequent and the observational record available to study them is relatively short compared to the timescales of the earthquake cycles. To address this, we can either revisit well-recorded historical events or generate rupture scenarios. In Chapter 4, we expand on the second approach focus on New Zealand as case study. This work was previously published and is the result of an international collaboration with GNS Science (now Earth Sciences New Zealand), as part of their efforts to test and implement systems capable of providing earthquake early warning (EEW) alerts, or at least rapid notice of strong shaking, to areas that may be affected.

New Zealand's vulnerability to seismic hazards highlights the need for such systems capable of providing more timely and accurate earthquake alerts. Large offshore earthquakes along the subduction zone east of the North Island could also trigger catastrophic tsunamis, inundating coastal communities in under an hour. While New Zealand maintains a well-instrumented seismic and geodetic network that can monitor moderate-to-large events in real time, the limited observational record of large earthquakes poses challenges for EEW design and response. This case study evaluates the performance of G-FAST, an EEW algorithm that leverages Global Navigation Satellite System (GNSS) data to rapidly estimate earthquake magnitude. We analyze synthetic rupture scenarios along the Hikurangi subduction margin generated by the earthquake simulator Rate and State Earthquake Simulator (RSQSim). For each rupture, GNSS displacements are generated at each site and compared with Peak Ground Displacement (PGD) scaling relationships to test whether they replicate real earthquakes. While we also assess PGD values from rupture scenarios produced with simpler semi-stochastic kinematic modeling, those from RSQSim yield ground motions more consistent with expected values. Given these results, synthetic displacement data from RSQSim ruptures were ingested into G-FAST to evaluate performance for rapid earthquake characterization, finding that PGD-based estimates capture moment magnitude in most cases. This framework demonstrates the utility of synthetic catalogs for testing geodetic EEW performance in characterizing large subduction earthquakes in the North Island region and provides a pathway toward tsunami early warning procedures.

CHAPTER 2

SLOW RUPTURE, LONG RISE TIMES, AND MULTI-FAULT GEOMETRY: THE 2020 M6.4 SOUTHWESTERN PUERTO RICO MAINSHOCK

From Solares-Colón, M. M., Goldberg, D. E., Melgar, D., Vanacore, E. A., Sahakian, V. J., Yeck, W. L., Hernández, F. , and López-Venegas, A. M. (2025). Slow rupture, long rise times, and multi-fault geometry: The 2020 M6.4 southwestern Puerto Rico mainshock. *Geophysical Research Letters*, 52, e2024GL109740. https://doi.org/10.1029/2024GL109740

2.1 Introduction

The **M**6.4 earthquake in southwestern Puerto Rico on 7 January 2020, was the most impactful seismic event in the past century since the **M**7.2 tsunamigenic earthquake in northwestern Puerto Rico on 11 October 1918 (Doser et al., 2005). This seismic event was felt across the island of Puerto Rico with a maximum shaking intensity of VII ("very strong") on the Modified Mercalli intensity scale (**Figure 2.1**, Wald et al., 2012)—it caused power outages, and extensive infrastructure damage in the southwest region of the island (López-Venegas et al., 2020). The **M**6.4 event was the mainshock of the southwestern Puerto Rico seismic sequence (SWPRSS), which began with a strike-slip **M**4.7 event on 28 December 2019, and included two foreshocks: a strike-slip **M**5.8 event and an oblique-normal **M**4.9 event on 6 January 2020, leading up to the mainshock (**Figure 2.1**, Blasweiler et al., 2022; López-Venegas et al., 2022). Four years later, this ongoing seismic sequence continues to produce aftershocks of **M** > 3.5, with activity distributed across a complex set of geological structures within the Puerto Rico and Virgin Islands block, illuminating previously unrecognized faults in southern Puerto Rico (**Figure 2.1**, ten Brink et al., 2022; Yoon et al., 2023).

Modeling the mainshock presents challenges due to its location offshore and the likelihood that multiple causative faults were involved, as indicated by the distribution of foreshocks and aftershocks (**Figure 2.1**), which show a recurring pattern of normal and strike-slip motions (Blasweiler et al., 2022; Cromwell et al., 2022; Liu et al., 2020; ten Brink et al., 2022; Yoon et al.,

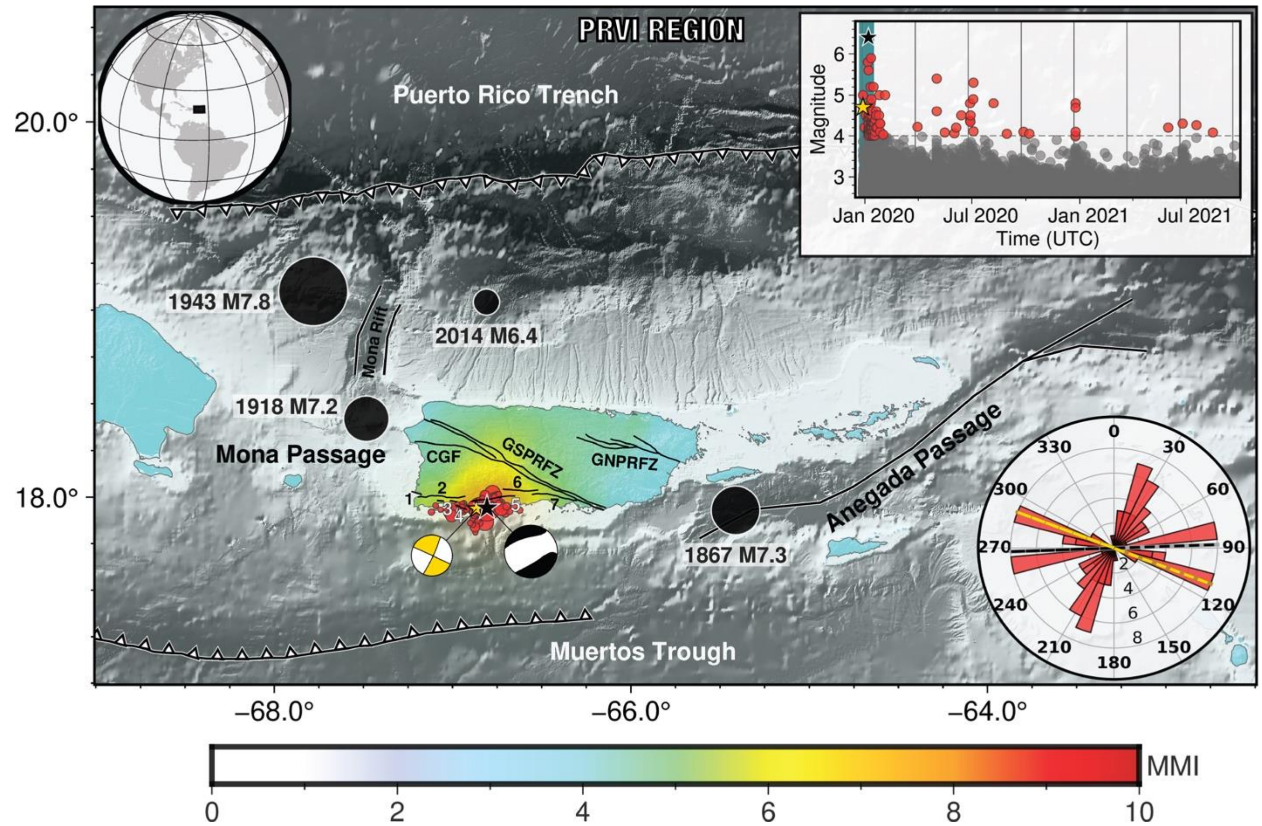

Figure 2.1. Overview of the seismotectonic setting of the Puerto Rico and Virgin Islands (PRVI) block with the major tectonic boundaries in northeastern Caribbean. The north (Puerto Rico Trench) and south (Muertos Trough) boundaries are transpressive margins of the PRVI block. The west (Mona Passage) and east (Anegada Passage) boundaries are extensional zones of the PRVI block. The black lines within Puerto Rico show known major inland faults (Thompson Jobe et al., 2024); Great Northern Puerto Rico fault zone, Great Southern Puerto Rico fault zone, Cerro Goden fault (CGF), (a) North Boquerón Bay fault, (b) South Lajas fault, (c) Parguera fault, (d) Punta Montalva fault, (e) San Francisco fault, (f) San Marcos fault, and (g) Salinas fault. Black circles show locations of historic events sized by magnitude. The colormap indicates the felt shaking intensity from USGS ShakeMap using the Modified Mercalli Intensity (MMI) scale, from Not Felt (0) to Extreme (10). The focal mechanism and epicenter corresponding to the M4.7 earthquake on 28 December 2019, that marks the start of the seismic sequence are in gold, whereas for the M6.4 mainshock on 7 January 2020, are shown in black. The inset figure (top right) shows the time series of magnitudes of events with M > 2.5 during the 2020–2021 southwestern Puerto Rico seismic sequence from 28 December 2019 to 1 October 2022. Red dots are events of M > 4.0. The black star shows the M6.4 mainshock event of this seismic sequence and the gold star marks the beginning of the seismic sequence. The teal shaded bar denotes the time frame of interferometric synthetic aperture radar scene used in this study. The inset rose plot (bottom right) shows the strike of principal nodal planes for M > 4.5 events with calculated moment tensors. The black dashed line shows the strike direction of the interpreted causative nodal plane of the M6.4 mainshock, and the gold dashed line shows the interpreted causative nodal plane strike of the event that initiated the seismic sequence. The inset globe map (top left) outlines the map area as a black rectangle.

2023). An indicator of this more complex rupture process is the low double-couple earthquake mechanism (52%) of the U.S. Geological Survey (USGS) moment tensor, which is diagnostic of this geometrical complexity (e.g., Rösler & Stein, 2022). This productive seismic sequence (van der Elst et al., 2022) could have also influenced data sources with substantial foreshock and aftershock events occurring close to the time of the mainshock (**Figure 2.1**). To address these challenges, we perform a non-linear inversion and solve for critical kinematic parameters such as rise time and onset of slip (correlated to rupture velocity) at each subfault using the finite-fault inversion software Wavelet and simulated Annealing SliP (WASP, Koch et al., 2019). This code integrates regional observations with traditional teleseismic data and is currently in use by the USGS National Earthquake Information Center (NEIC, Goldberg et al., 2022). We further developed efforts to model the mainshock as a multi-fault rupture, building upon the work of Liu et al. (2020), which indicated a shallow intraplate rupture on an oblique-normal fault with a high stress drop.

Considering the dense regional station coverage and the availability of remote sensing observations, we can attain sufficient resolution to analyze the kinematic properties (i.e., slip amplitude, direction, rise time, rupture onset time, and rupture velocity) of the **M**6.4 mainshock in Puerto Rico, despite its moderate magnitude. Our refined finite-fault model (FFM) indicates a preference for slow rupture velocity and long rise times, atypical for an earthquake of this size. These peculiar rupture kinematics are verified by a ground motion residual analysis—although shaking was still quite hazardous, it was substantially less intense than what is predicted by ground motion models (GMMs) for an earthquake of this magnitude and more consistent with a slow rupture. Results from this study will contribute to a better understanding of the seismotectonic characteristics and seismic hazard assessment in southwestern Puerto Rico that can be considered for future earthquakes in the region.

2.1.1. Seismotectonic Overview

Puerto Rico lies within a broad deformation zone (**Figure 2.1**) involving oblique convergence of the Caribbean and North America plates. Along the east-west striking Puerto Rico Trench, the North American plate is subducting to the southwest at a rate of ~20 mm/yr (DeMets et al., 2010). The Island of Puerto Rico is in the northeastern edge of the Caribbean plate and is physiographically bound by the Puerto Rico Trench to the north and the Muertos Trough to the south. The Muertos Trough is an elongated depression, where the island arc is thrusting over the interior of the Caribbean plate forming a back-arc retrowedge (Granja Bruña et al., 2009, 2015; ten Brink et al., 2009).

Puerto Rico and the Virgin Islands (PRVI) comprise a tectonic block that moves westward at a rate of ~2 mm/yr with respect to the Caribbean plate (Jansma & Mattioli, 2005; **Figure 2.1**). To the east and west, the PRVI block is delimited by extensional zones, the Anegada Passage and

Mona Passage, respectively (Chaytor & ten Brink, 2010; Laurencin et al., 2017). The motion of the PRVI block is primarily controlled by the interactions of the Caribbean and North American plates to the north at the Puerto Rico Trench. The remaining motion is partially accommodated by onshore faults in Puerto Rico. Recent findings from Global Navigation Satellite Systems (GNSS) observations indicate the existence of a detaching microblock within the PRVI block moving southwest in the southwestern part of Puerto Rico (Solares-Colón, 2019), where shallow seismicity is concentrated and where the seismic sequence later propagated (Asencio, 1980; Prentice & Mann, 2005). Further investigation could reevaluate the western boundary of the PRVI block and provide a more detailed understanding of how the motion is accommodated between Puerto Rico and Hispaniola, now referred to as the Western Puerto Rico Deformation Boundary (ten Brink et al., 2022).

Numerous onshore fault systems have been documented across Puerto Rico (**Figure 2.1**). These include the Great Southern Puerto Rico fault zone, the Great Northern Puerto Rico fault zone, the South Lajas fault, and the Salinas fault (Piety et al., 2018; Prentice & Mann, 2005). Recent works focused on southwestern Puerto Rico have identified the seismically active onshore Punta Montalva fault, which may intersect the South Lajas fault and connect to the North Boquerón Bay fault at depth (Adames-Corraliza, 2017; Addarich-Martínez, 2009; Roig-Silva et al., 2013; Weilert & Laó-Dávila, 2023; **Figure 2.1** for reference on fault mapping). However, field evidence is insufficient to support a definitive connection between the North Boquerón Bay fault and the Punta Montalva fault. Offshore in the Anegada Passage and Mona Passage, both regions have hosted damaging **M**7+ earthquakes and associated tsunamis in 1867 and 1918, respectively (McCann, 1985; **Figure 2.1**). The largest historical earthquake near Puerto Rico was a 1943 **M**7.8 (Doser et al., 2005) event off the northwest coast, which was widely felt but caused no damage or tsunami. Prior to the 7 January 2020, **M**6.4 mainshock in southwestern of Puerto Rico, the largest earthquakes to occur near land were the 1918 **M**7.2 (Doser et al., 2005) event off the northwest coast of Puerto Rico in the Mona Passage and the 2014 **M**6.4 event offshore north of Puerto Rico toward the Puerto Rico Trench.

The causative fault(s) of the 7 January 2020, mainshock have not been previously reliably determined. Initially, it was thought that the seismic sequence was initiated by an extension of the Punta Montalva fault, an east-west striking sinistral fault on a steep plane (López-Venegas et al., 2022), but the Punta Montalva fault was instead activated as the seismic sequence progressed westward (Weilert & Laó-Dávila, 2023; Yoon et al., 2023). Currently, a new potential seafloor fault system is under investigation in the Guayanilla canyon, located east of the Punta Montalva fault and south of the San Francisco fault, near the mainshock rupture zone (**Figure 2.1**). Geomorphological observations show evidence of repeated normal faulting, as well as submarine canyon meanders developed over geologic time, which may have been influenced by past seismic activity (ten Brink et al., 2022). This area is considered a diffuse deformation zone within the Western Puerto Rico Deformation Boundary that will likely continue to produce seismic sequences similar in magnitude to the SWPRSS (ten Brink et al., 2022). The complex network of multiple faults and the associated diffuse seismicity exhibit various orientations and fault mechanisms—including normal, sinistral, and dextral slip, indicating that it is an immature fault system (Yoon et al., 2023). Here, we use a combination of foreshock and aftershock distributions, moment tensor analysis, geodetic observations, and regional tectonics to provide some additional clarity on the orientation of the faults involved during the mainshock.

2.1.2. Significance of the Seismic Sequence and the M6.4 Mainshock

The SWPRSS is the first recorded and well-documented event of this magnitude with modern instrumentation in Puerto Rico, providing valuable insight into the complex deformation and impacts in the southwestern part of the island. This seismic sequence captured substantial public attention from governmental entities and civilians, thereby promoting awareness of earthquake risks and preparedness. Also, it propelled geophysical studies in Puerto Rico, ranging from collecting seismic profiles to mapping active onshore faults in the island and offshore faults in the southwest region, to conducting studies of the average shear wave velocity in the upper 30 m of the crust (Vs30), seismic lines, and immediate post-earthquake reconnaissance—such as the assessment of subsidence, reoccupation of GNSS campaign sites, and liquefaction effects. Ultimately, these efforts contribute toward reducing the impact of earthquake and tsunami hazards in Puerto Rico.

Moreover, the extensive data availability following the **M**6.4 mainshock enabled a more detailed study of the rupture process (**Figure 2.2**), revealing that moderate earthquakes can exhibit characteristics as complex as large earthquakes. Tackling events like this one, when dense data are available, not only contributes to our understanding of earthquakes in a region of interest but also facilitates further exploration of lower magnitude events and reduces the knowledge gap of event kinematics below **M**7.

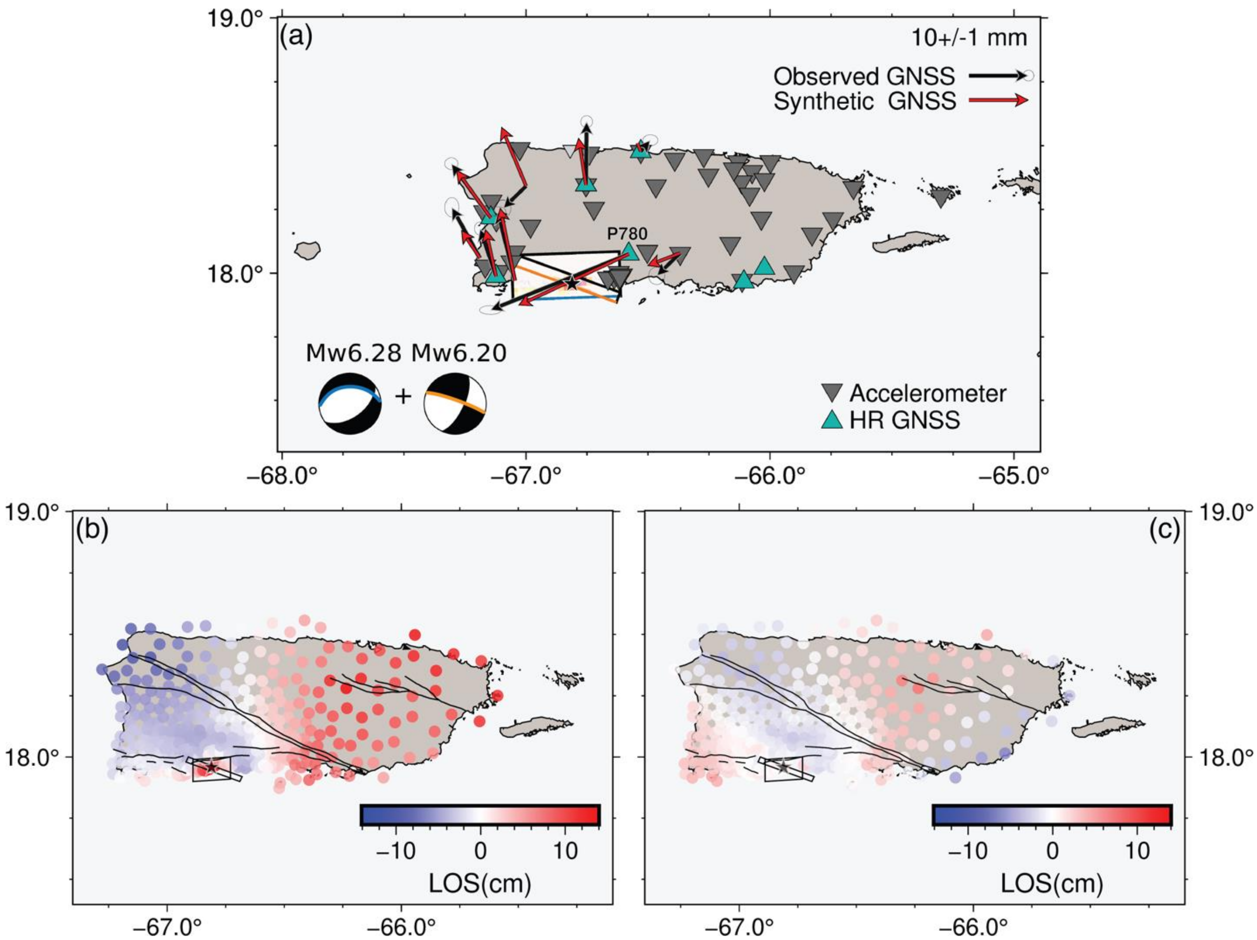

Figure 2.2. Data availability and fault model. (a) Multi-segment model for the M6.4 mainshock of the southwestern Puerto Rico seismic sequence; vectors denote static offsets (observations in black and model synthetics in red); aqua triangles represent the high-rate Global Navigation Satellite Systems station locations, and dark gray inverted triangles represent accelerometer locations. The two considered faults are outlined in black, with updip edges marked in blue and orange for the normal and strike-slip faults, respectively. The focal mechanisms for each segment are at the bottom left. (b) Observed interferometric synthetic aperture radar (InSAR) line of sight (LOS) and (c) InSAR LOS misfits after inversion, where negative values indicate motion toward the satellite and positive values indicate motion away from it.

2.2. Data

In this study, we model the finite slip of the mainshock considering data from 51 broadband teleseismic waveforms (14 P-waves, 13 SH-waves, and 24 long period surface waves), 67 regional strong-motion accelerometers, 7 high-rate (HR) GNSS stations, 9 GNSS static offsets, and 4 interferometric synthetic aperture radar (InSAR) pairs (refer to Data and Resources).

For teleseismic waveforms, we applied a band-pass filter between 0.01 and 1.0 Hz to body waves (i.e., P and SH), and a band-pass filter between 0.003 and 0.007 Hz for surface waves (i.e., Rayleigh and Love). For regional strong motion waveforms, we considered 41 accelerometers for inversion that had reliable metadata (**Figure 2.2**). We applied to each a band-pass filter between 0.02 and 0.125 Hz to remove baseline offsets. High-rate GNSS observations with a sampling rate of 1 Hz were processed to obtain positions using the software GipsyX (Bertiger et al., 2020). GNSS static offsets used are the ones published by López-Venegas et al. (2022). Finally, the InSAR interferograms from Sentinel-1, operated by the European Space Agency, were processed with the InSAR Sci- entific Computing Environment package (ISCE, Rosen et al., 2018), unwrapped, and down sampled to a tractable number of observation points for model computation using the QuadTree interpolation algorithm (Lohman & Simons, 2005). Of four InSAR scenes considered, we included one ascending InSAR scene based on the agreement between observed coseismic offsets at GNSS sites projected to the line of sight (LOS) and the InSAR acquisitions (e.g., Melgar et al., 2017; refer to **Figure 2.2** and **Figure 2.S1** in Supporting Information). Our assumption was that the magnitude of the LOS displacements at pixels close to GNSS sites should yield a similar amount of displacement as the three-dimensional GNSS offset projected onto the InSAR look direction. The remaining InSAR scenes, which had high discrepancies with the GNSS sites, particularly at the P780 site that had the largest offset (**Figure 2.2**), were disregarded based on this criterion. We also considered the timing of the repeat passes because delays after the mainshock could have contributed to discrepancies in the observations, due to the influence of aftershocks or postseismic displacements. Although the selected InSAR scene was acquired 9 days after the mainshock, it is consistent with coastal subsidence observed in southern Puerto Rico. All data considered in this study are available in a USGS data release (Solares-Colón et al., 2024; refer to Data and Resources).

2.3. Methods

2.3.1. Non-Linear Inversion Method for Finite-Fault Modeling

The FFM of the M6.4 earthquake was produced using WASP software as described in Goldberg et al. (2022). This code uses a nonlinear inversion following the methods of Ji et al. (2002) and Koch et al. (2019) to jointly invert teleseismic and regional observations. This method solves for slip amplitude, rake (slip direction), rise time, and rupture onset time on a discretized fault plane at each subfault. We also solve for an additional inversion parameter, a linear InSAR "ramp" in the InSAR data, which is often observed in interferograms and apparent in **Figure 2.2c** at greater distances from the mainshock epicenter. This latter effect is due to imprecise satellite orbit positions or unmodeled tropospheric contributions (Hanssen, 2001). The linear ramp coefficients are estimated simultaneously within the inversion, to reduce the potential to misidentify the atmospheric ramp signal as earthquake deformation, or vice versa.

We use the first nodal plane (strike = 267°, dip = 41°, and rake = -54°) from the Global Centroid Moment Tensor solution to define an initial fault plane orientation, relative to the NEIC hypocenter location. The focal mechanism associated with this event is consistent with normal faulting on a northward-dipping plane, as indicated by geomorphic observations and coastal subsidence in southern Puerto Rico from InSAR data as well (**Figures 2.1** and **2.2**, López-Venegas et al., 2022; ten Brink et al., 2022; Viltres et al., 2022). By default, WASP assumes a one-dimensional regional velocity model from LITHO1.0 at the hypocenter location (Pasyanos et al., 2014). How- ever, we replaced this model with a local velocity model provided by the Puerto Rico Seismic Network (PRSN) specific to the southwestern region of Puerto Rico (refer to Data and Resources). After successfully incorporating each data set into the inversion, we proceed to manually evaluate misfits to all sites and remove poorly fitting channels (refer to Data and Resources). We allowed rake values within a range of ±20°, following the fault plane orientation (strike = 268°, dip = 43°, and rake = -72°) in ten Brink et al. (2022), set rupture velocities values from 1.0 to 3.1 km/s, and used the PRSN hypocenter location, given that it is the authoritative regional network and provides a better fit to the data, as confirmed by similar location results from other studies as well (Liu et al., 2020; ten Brink et al., 2022). At this stage, given the high compensated linear vector dipole of the moment tensor (48%), we introduced a secondary fault plane oriented with a strike and dip (290° and 80°) similar to notable strike-slip events of **M** > 4.5 during the seismic sequence (**Figure 2.1**), allowing for the same varying ranges in the kinematic parameters.

While both sinistral and dextral motions fit the data, we opted for a left-lateral motion. This choice is supported by regional tectonics, which predominantly exhibit left-lateral motion, and similarity to the fault kinematics of active faults such as the Punta Montalva fault involved in the seismic sequence. Additionally, we reexamined regional waveforms to derive the focal mechanism from first motions using the PRSN solution polarities, comparing them with the USGS W-phase focal mechanism solution. Although there were not enough stations to obtain a fully reliable solution, the focal mechanism derived from PRSN first motions more closely resembles a strike-slip fault rather than a normal fault, as the **M**5.8 foreshock (**Figure 2.S2** in Supporting Information, Pugh et al., 2016; refer to Data and Resources for event information), which informed our choice for the second fault segment. This setup accounts for a more complex fault geometry, consistent with the regional active faults and event focal mechanisms.

2.3.2. Ground Motion Residuals

A ground motion residual, r_i, at station *i*, is the difference between an intensity measure observed at that site, obs_i, and the intensity predicted from a GMM, $pred_i$, in natural log space, such that:

$$r_i = ln\left(\frac{obs_i}{pred_i}\right). \tag{1}$$

Patterns in the ground motion residuals obtained from Equation 1 can be used to understand relative contributions from source, path, and site to the observed intensities (e.g., Sahakian et al., 2018). We use the peak ground acceleration (PGA) as a high-frequency intensity metric to evaluate ground shaking in the near field and to investigate whether they are consistent with the kinematics of the source described by the FFM. It has been observed that, for slow rupture, long-rise time events, high-frequency seismic energy radiates inefficiently and can manifest as very low ground motion residuals in the near field (Sahakian et al., 2019). The ground motion residuals analysis allows us to identify deviations from the mean behavior of earthquakes represented by GMMs.

The GMMs we considered for modeling shaking intensity of this event are from Boore et al. (2014), hereafter referred to as B14, for shallow crustal earthquake events and Parker et al. (2022), hereafter referred to as P22, for subduction interface earthquake events. The mainshock is a shallow event to a depth of ∼7 km, whereas the slab depth is ∼40 km (Hayes et al., 2018). Therefore, a GMM that considers this event as a shallow crustal earthquake is likely more suitable to model it. However, at present, no updated GMM for Puerto Rico is published, so we use these two different models to explore a range of possibilities.

2.4. Results & Discussion

2.4.1. Source Characterization of M6.4 Mainshock

Our refined FFM of the mainshock consists of two segments with different fault orientations (**Figure 2.2**). The first segment corresponds to the initial focal mechanism derived for the mainshock, which is an oblique-normal fault dipping north. The second segment is defined by the moment tensor analysis and distribution of foreshocks and aftershocks, which is an east-west striking sub-vertical strike-slip fault that intersects the first segment. These two fault orientations and faulting mechanisms repeat throughout the development of the SWPRSS and seem fit to model the mainshock (refer to rose plot in **Figure 2.1**). The resulting distributed slip model is given in **Figure 2.3**. Of note, the cumulative moment tensor of these two segments, contributing 57% and 43% to a total seismic moment of 5.74 × 1018 N-m, respectively, returns the preferred USGS solution (**Figure 2.3c**; refer to Data and Resources for the USGS moment tensor solution). This agreement accounts for the very low double-couple earthquake mechanism (52%) of the published USGS moment tensor and is consistent with prior hypotheses that this was a multi-segment rupture (Liu et al., 2020; ten Brink et al., 2022).

Separate seismic and geodetic inversions for both single and multi-segment rupture models were also performed to explore the contribution of different data sets in our slip models (refer to **Figure 2.S3** in Supporting Information and Data and Resources). The seismic inversion included teleseismic broadband and regional strong motion observations, while the geodetic inversion included HR GNSS observations, GNSS static offsets, and one InSAR scene. The key differences were that the geodetic inversions revealed a higher seismic moment release, greater peak slip, and surface rupturing compared to the seismic inversion. Despite variations in the number of segments, both scenarios showed a peak energy release at around 6–8 s, with a total duration of approximately 16 s. This duration is longer than anticipated for a **M**6.4 earthquake, where the expected source duration would be approximately 6–7 s for an event of this size (Melgar & Hayes, 2017; Somerville et al., 1999) and it is higher than 10–12 s found by previous studies (Liu et al., 2020; Viltres et al., 2022). Liu et al. (2020) and Viltres et al. (2022) used different methods—the first study using seismic data and two GNSS coseismic displacements with an inversion method similar to that of Ji et al. (2002, 2003), resulting in an estimated rupture duration of approximately 12 s, and the second study using a Bayesian inference method with a constant rupture velocity of 3.5 km/s, finding a rupture duration of 10.6 s. Even if we account for potential waveform noise or inversion artifacts causing the later slip (after the 10 s contours), the slip concentration near the surface in our model falls within the 10–12 s rupture duration, aligning more closely with previous studies—all of which identify durations longer than expected.

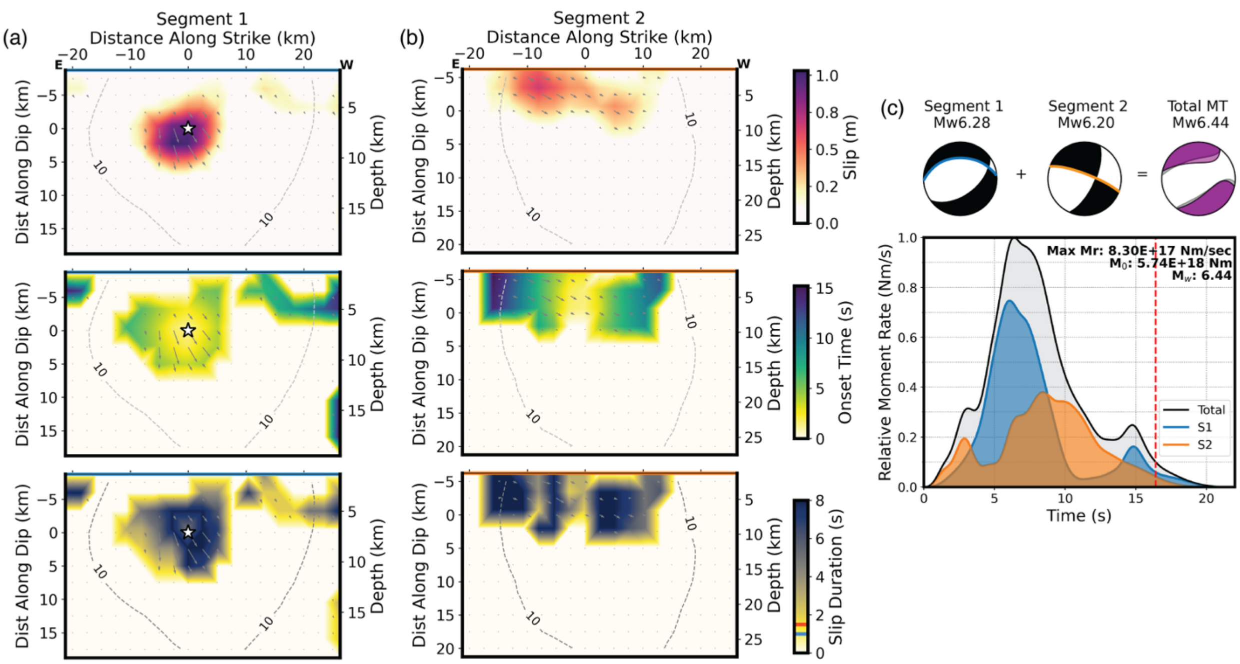

Figure 2.3. Multi-Segment Slip Model for the M6.4 mainshock. Panels (a, b) shows slip models for each segment, first row shows slip distribution; second row shows onset time, and third row shows rise times for subfaults with >10% maximum slip; the red and blue lines in the third row color bar represent the mean rise time expected for an event of M6.4, around 1 and 1.4 s, based on Somerville et al. (1999) and Melgar and Hayes (2017), respectively; rupture front contours are plotted every 10 s. Panel (c) shows decomposition of focal mechanism with preferred fault plane (blue for Segment 1 and orange for Segment 2) and their respective moment magnitude (Mw), which sum to produce the cumulative focal mechanism (magenta) plotted on top of the published U.S. Geological Survey moment tensor (MT) solution for the mainshock (gray; refer to Data and Resources for the MT solution) for comparison; below is the source time function with each segment's respective source time function; vertical dashed red line represents the interpreted end of the rupture (~16 s); maximum moment rate (Mr); seismic moment (Mo).

In the joint inversion, when incorporating regional data sets from both seismic and geodetic sources, the image of the source sharpens—the peak slip more than doubles from ~0.4 to ~1.0 m, the location of the main asperity moves up-dip, and it reduces in size, compared to the derived seismic models (refer to Data and Resources). Geodetic data, as observed from our separate inversions, contribute most to capture the actual seismic moment of the earthquake and allows for greater slip. This result supports earlier studies (e.g., Goldberg et al., 2022) that the addition of regional data reveals smaller-scale features of the slip distributions, including for an earthquake of lower magnitude (**M** < 7). In terms of kinematics, this refined model indicates a low rupture velocity, with an average speed of 1.8 km/s for the first segment and of 1.6 km/s for the second segment when considering only subfaults with slip >10% of peak slip. The former results are in agreement with the single oblique-normal fault plane inversion of Liu et al. (2020), who also found an average speed of 1.8 km/s. Worldwide, the average rupture speed for shallow earthquakes in databases of finite faults is considered to be much closer to 2.5 km/s (Melgar & Hayes, 2017; Ye et al., 2016), and so for this event, these values are markedly below average. Another way to view this is that "typical" rupture speeds are usually ∼80% of the local shear wave speed. For the velocity model at the depths of the largest slip patches that we used, these values represent ∼50% of shear wave speed. More interestingly, we also recover very long rise times for an event of this magnitude—on average we obtain 5.1 s for the first segment and 6.2 s for the second segment when considering again only subfaults with more than 10% of peak slip (**Figure 2.3**). In contrast, Liu et al. (2020) found rise times between 1.6 and 2.4 s. A typical M6.4 event is expected to have a mean rise time of only ∼1 s (Melgar & Hayes, 2017; Somerville et al., 1999). In short, we find rise times a factor of ∼5 and a source duration a factor of ∼3 longer than expected. This is very striking and similar to very shallow ruptures in megathrust where the same behavior is observed in so-called tsunami earthquakes (Kanamori, 1972; Satake & Tanioka, 1999).

2.4.2. Ground Motions Support Peculiar Source Kinematics for a Slow-Evolving Rupture

We conducted a ground motion residual analysis using PGA as an intensity metric to validate our refined model with a slow rupture velocity and longer rise times. Note that a positive residual, as defined by Equation 1, means that the observed value is higher than expected, or that the GMM is underpredicting the observations. A negative residual means that the observed value is lower than expected, or that the GMM is overpredicting the observations. **Figure 2.4** shows GMM residuals assuming a shallow crustal earthquake (B14). Due to the shallow depth, the B14 model is likely more applicable for this event than the P22 model assuming subduction interface earthquake. Regardless of the GMM used, when compared to the observed PGA values in the near field, residuals consistently remain negative (refer to **Figure 2.S4** in Supporting Information). The exception is in the northern central part of Puerto Rico, where the highest PGA values are observed.

This region experiences a site amplification effect—particularly in Utuado, Puerto Rico, leading to higher PGA values than expected from GMMs (refer to **Figure 2.S5** in Supporting Information).

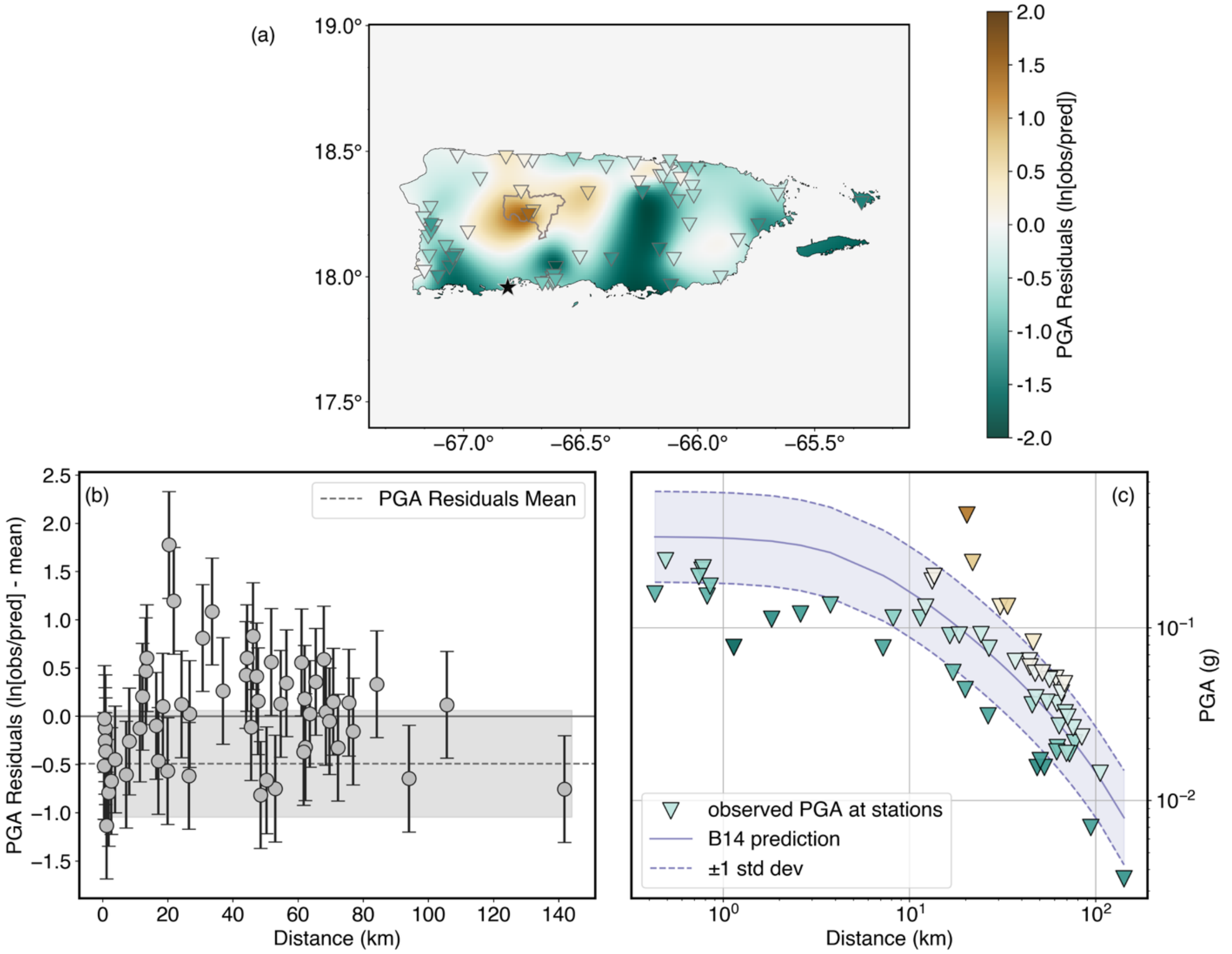

Figure 2.4. Residuals analysis using the Boore et al. (2014) (B14) ground motion model (GMM). (a) Map shows the location of strong-motion rock sites with colored peak ground acceleration (PGA) residuals; the gray polygon within Puerto Rico shows the municipality of Utuado (Puerto Rico), and the black star denotes the mainshock epicenter. (b) PGA residuals assuming mean as a function of rupture distance using the closest distance from the site to the surface projection of the rupture plane (RJB); gray dashed line shows mean PGA value, and gray area shows mean plus or minus one standard deviation. (c) PGA observed values with colored PGA residuals as a function of rupture distance in natural log space; purple area shows predicted PGA values plus or minus one standard deviation as dashed lines from GMM assuming hard rock site.

Although only a tsunami of 6 cm was generated by the mainshock (refer to Data and Resources), this shallow event in a transpressive margin above the Muertos Trough shares some characteristics reminiscent of tsunami earthquakes. Tsunami earthquakes generate a larger-than-expected tsunami for the magnitude of the earthquake (Kanamori, 1972; Satake & Tanioka, 1999). These types of earthquakes are infrequent, and the scarcity of data near the source poses a difficulty for studying these events. A well-documented example is the 2010 Mentawai earthquake, a shallow thrust event offshore Sumatra within the Sumatra-Java subduction zone (Sahakian et al., 2019). The comparison is relevant because events in this category typically rupture shallow parts of a subduction zone and radiate high-frequency energy ineffectively, resulting in abnormally low shaking compared to the earthquake magnitude as we observed in the case of the Puerto Rico mainshock. PGA residuals for the mainshock are not as remarkably low as those observed in the 2010 Mentawai earthquake example, which are centered around -2 natural log units when compared to the mean of PGA residual of the SWPRSS mainshock at -0.5 natural log units (**Figure 2.4b**). However, residuals are still consistently low, and the stations are substantially closer to the source of the mainshock (**Figure 2.4**) than in the case of the Mentawai strong motions sites reported by Sahakian et al. (2019). Low PGA values, particularly in the near-field, may explain the depletion or absence of high-frequency source content, as shaking at these near-field distances is more a function of source effects than path and attenuation effects (Baltay & Boatwright, 2015), but is inconsistent with average or higher static stress drops such as the stress drop of ~19 MPa reported by Liu et al. (2020), which is higher than the global average. Using the earthquake rupture length (*L*) and width (*W*) probabilistic scaling laws from Blaser et al. (2010), we obtained the mean expected dimensions for each segment of the mainshock (refer to **Text 2.S1** in Supporting Information). We find that the first segment is shorter (-1.4 standard deviations from the mean), and its width is as expected for a normal fault of **M**6.3. For the second segment, we observe a rupture that is longer than its width, indicating an elongated feature as expected for a strike-slip fault of **M**6.2. The first segment exhibits a more circular, condensed rupture, potentially transferring energy along the second plane. The net result is a compact source, and this could account for the high stress drop value.

A second metric for comparison with well-known energy deficient events such as tsunami earthquakes involves using the ratio of radiated seismic energy to seismic moment (Convers & Newman, 2011; Newman & Okal, 1998; Okal & Newman, 2001; Ye et al., 2016). This metric reflects the high-frequency characteristics of an earthquake source and is particularly useful for identifying deficiencies in moment release at high frequencies. These previous studies have also shown no dependence on the overall seismic moment. Based on teleseismic observations and scaling properties of megathrust ruptures, estimates of the energy-to-moment (E/M_o) ratio for tsunami earthquakes are notably below the global average of 1.06 × 10-5, as reported by Ye et al. (2016), and typically closer to a value of ~2.5 × 10-6. Likewise, this measure can be expressed as the discriminant $\Theta = \log10$ (E/Mo, Newman & Okal, 1998). Slow ruptures usually have values of about -5.7 (Okal & Newman, 2001 while the global average is closer to Θ = -4.59 with some deviations depending on type of faulting (Θ = -4.51 for normal events, Convers & Newman, 2011). When considering the mainshock, given E is equal to 9.9×10^{13} J (refer to Data Resources) and E/M_o is 1.72×10^{-5}, the resulting Θ value is -4.76, which is slightly below the mean for normal events. If we use E for a higher frequency range, Θ is equal to -5.12 tending toward what is characteristic of slow ruptures.

These teleseismic measures of energy-to-moment are somewhat at odds with the key findings that the mainshock exhibits longer duration (~16 s) and longer rise times (average of 6 s) than expected but are simultaneously consistent with the meaningfully low near-source ground motion residuals. We posit that this discrepancy may be due to the rupture complexity and the difference in frequency content of regional ground motion, which could be depleted but appears about average for the frequencies that are predominant in calculations of the discriminant Θ. Regardless, we find that the rupture kinematics share some characteristics of tsunami earthquakes, which concur with our refined model and support a slow-evolving rupturing process for this shallow event. Could the longer and slow rupture of the mainshock be a result of two independent sources (two seismic events), or is it one slow rupture that triggered the second event? It remains unclear, but the mainshock is almost certainly the result of a multi-segment rupture, contributing to the overall seismic event.

2.5. Conclusions

A multi-segment rupture caused the **M**6.4 mainshock of the SWPRSS. Insights from joint inversion adding regional seismogeodetic data increased model resolution to validate a complex and atypically slow-rupture process during the mainshock. Our findings show that rupture was slow (average of 1.7 km/s) and had anomalously long rise times (average of 5.7 s). These observations are supported by ground motion residuals that consistently show low PGA values indicating a slow and weak rupture that radiates high-frequency energy inefficiently. Therefore, these results can aid our understanding of earthquakes in southwestern Puerto Rico and in mitigation efforts for future events that could display tsunami earthquake-like behavior. The complication with this type of earthquake lies in the potential underestimation of earthquake hazards during the initial earthquake response. This is due to the magnitude registered by inertial instrumentation, which may not fully capture the earthquake size by the depletion or absence of high-frequency content.

A more detailed analysis is necessary to determine whether these kinematic characteristics are a common occurrence, specifically linked to the deformation in southwestern Puerto Rico, or if it represents a unique case for this event. This will involve examining ground motions for other aftershocks in the seismic sequence and significant events across the island to better characterize earthquakes in this region. Should this tsunami earthquake-like behavior be characteristic of earthquakes in the southwest of Puerto Rico, we can anticipate low PGA values for events and enhance preparedness for future earthquake responses.

Moderate earthquakes (~**M**6), such as the mainshock, can be devasting for the local community, having significant economic and human impact depending on their timing and location (e.g., Minson et al., 2021). In this study, we are not only extending the NEIC database of FFMs, but also our knowledge about earthquake processes for smaller events (**M** < 7) that are more frequent. Accounting for events such as the 2020 SWPRSS mainshock can also contribute to a more in-depth understanding of source scaling properties for lower magnitude events and improve earthquake modeling in the future.

2.6. Acknowledgments

We thank William Barnhart for providing InSAR data. We are also grateful to Harley Benz, Kirstie Haynie, David Shelly, and Michael Hearne for their valuable feedback and discussions. Additionally, we would like to acknowledge the support of PRSMP, PRSN, and NEIC, particularly the data analysts who produced the geophysical data, for the completion of this investigation. Finally, we thank Jessica Thompson Jobe, the GRL Editor, and three anonymous reviewers for their time and constructive comments on this paper. Any use of trade, firm, or product names is for descriptive purposes only and does not imply endorsement by the U.S. Government.

2.7. Open Research

The Wavelet and simulated Annealing SliP (WASP) inversion code to obtained slip models is publicly available at https://doi.org/10.5066/P1EKKUNW (Koch et al., 2024). All data considered in this study, inversion models, and model fits are available in a USGS data release at https://doi.org/10.5066/P1VBFP8B (Solares-Colón et al., 2024). Teleseismic waveform data used in the study were obtained from the Seismological Facility for the Advancement of Geoscience (SAGE) facility operated by the EarthScope Consortium (https://ds.iris.edu/ds/). Strong motion data were provided by the Puerto Rico Strong Motion Program (PRSMP) and the Puerto Rico Seismic Network (PRSN). High-rate GNSS data were retrieved from the Geodetic Facility for the Advancement of Geoscience (GAGE) facility operated by the EarthScope Consortium repository (https://www.unavco.org/ data/) and the PRSN archives. Tsunami maximum wave heights for this event were obtained from National Centers for Environmental Information/World Data Service's Global Historical Tsunami Database at https://www.ngdc.noaa.gov/hazel/view/hazards/tsunami/related-runups/5736 (last accessed on 11 March 2024; NCEI/ WDS, 2024). Earthquake energy values were obtained from the EarthScope Data Services Products: EQEnergy Earthquake energy & rupture duration at https://doi.org/10.17611/DP/18022068 (EarthScope Data Management Center, 2013). The U.S. Geological Survey moment tensor (MT) solution for the **M**6.4 mainshock is available at https://earthquake.usgs.gov/earthquakes/eventpage/us70006vll/moment-tensor (last accessed on 30 August 2024). The U.S. Geological Survey event page for the **M**5.8 foreshock is available at https://earthquake.usgs.gov/earthquakes/eventpage/pr2020006006/executive (last accessed on 30 August 2024). Sentinel-1 InSAR data were obtained from the Alaska Satellite Facility—Distributed Active Archive Center (ASF DAAC) (Copernicus Sentinel data, 2020).

2.8. Supporting Information

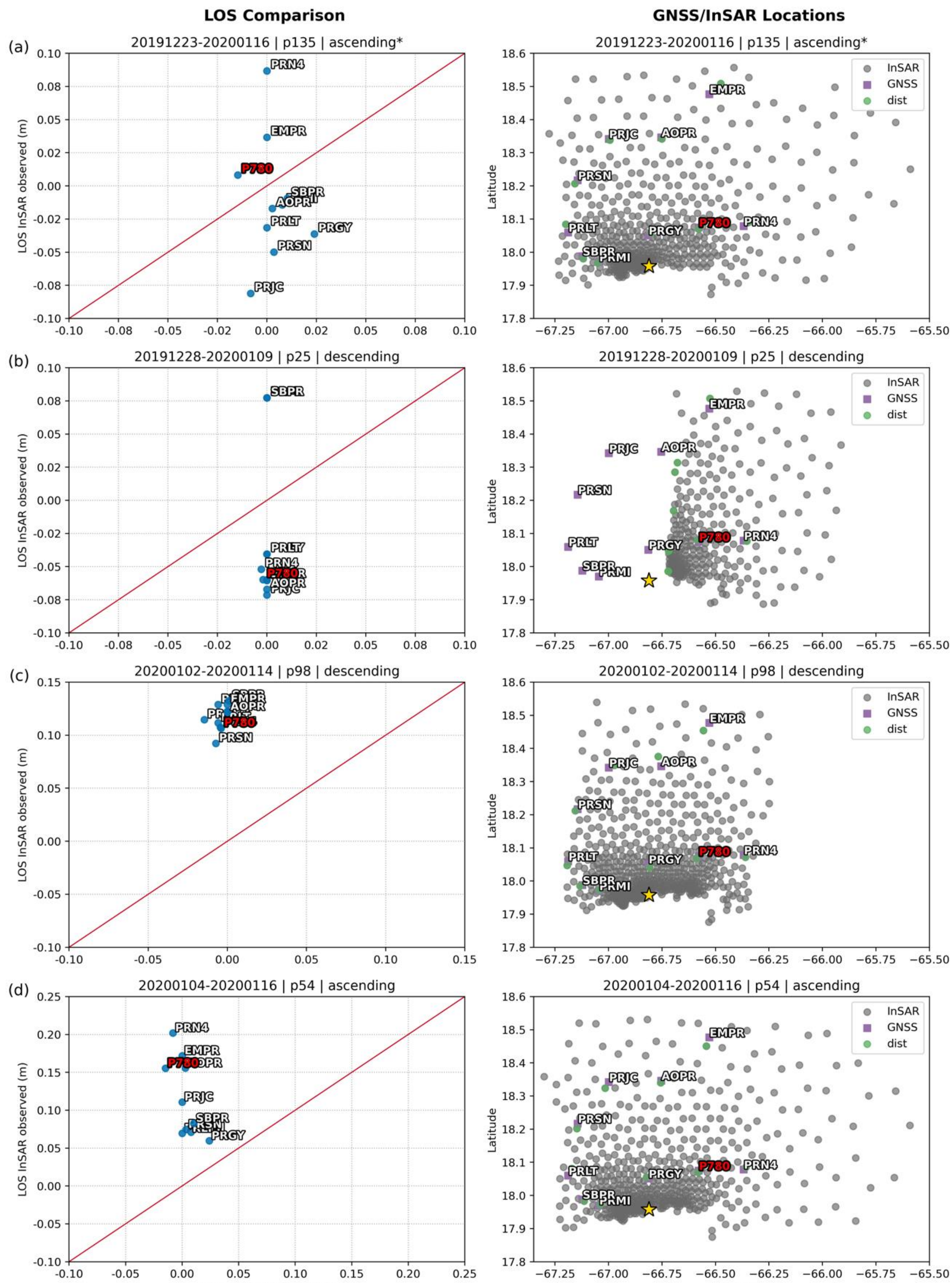

Figure 2.S1. Interferometric synthetic aperture radar (InSAR) scene selection for four InSAR interferograms from Sentinel-1. Comparison between InSAR LOS (line-of-sight) displacement and GNSS (Global Navigation Satellite Systems) offsets measurements for each InSAR scene, categorized from (a) to (d). The first column (LOS Comparison) shows comparison between GNSS offset projected onto InSAR LOS direction by taking the dot product of the corresponding vectors. The second column (GNSS/InSAR Locations) shows GNSS site locations as purple squares, InSAR scene coverage as gray circles, and InSAR pixel closest to GNSS station as green circles. The p135 ascending scene (marked with an asterisk (*)) was selected based on the agreement between InSAR LOS displacement and GNSS offset measurements, with consideration given to the P780 site, which had the largest coseismic offset and is located near the mainshock (gold star).

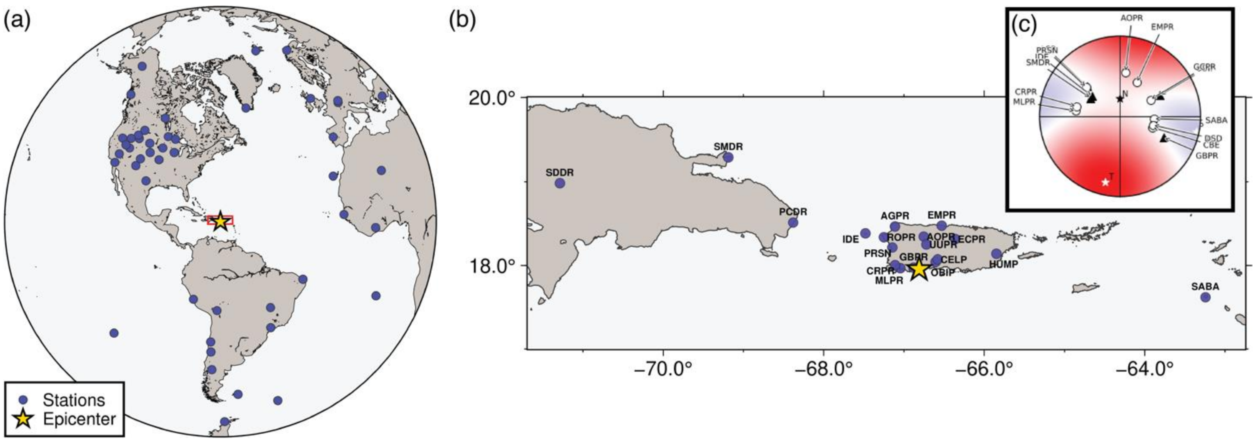

Figure 2.S2. Seismic station distribution and focal mechanism derived from Puerto Rico Seismic Network (PRSN) first motions. (a) Global map shows seismic station locations (blue circles); the red rectangle shows area in (b) with regional seismic station locations. (c) Focal mechanism derived from first motions using the PRSN solution polarities from regional seismic stations; red indicates positive polarity, and blue indicates negative polarity. This focal mechanism was compared with the U.S. Geological Survey W-phase focal mechanism solution, which indicates a normal fault mechanism and has a low double-couple component (52%). Although not enough stations were available to obtain a fully reliable solution, we found that the focal mechanism from PRSN first motions does not indicate a normal fault mechanism. Instead, it more closely resembles a strike-slip fault mechanism, similar to the precursor M5.8 and other significant strike-slip events with M>4.5 during the seismic sequence.

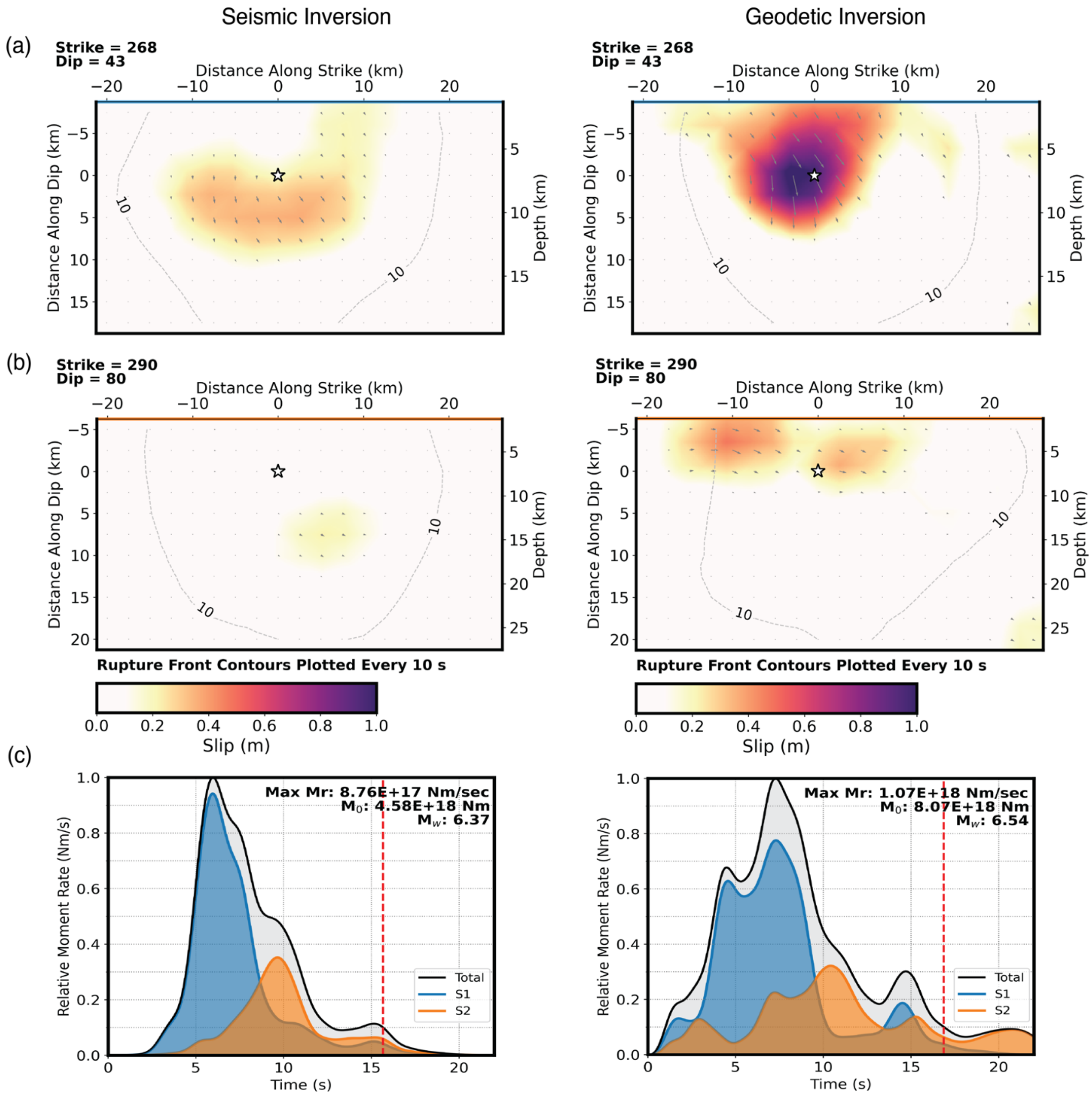

Figure 2.S3. Multi-segment slip model for the M6.4 mainshock: separate seismic and geodetic inversions. The first column (left) shows seismic inversion (teleseimic broadband and regional strong motion data), and the second column (right) shows geodetic inversion (Global Navigation Satellite Systems (GNSS) and interferometric synthetic aperture radar (InSAR) data). (a) shows slip model of the first segment (S1), (b) shows slip model of the second segment (S2), and (c) shows source time function for each separate inversion. The normalized color bar shows the amount of slip along dip on the y-axis and along strike on the x-axis.

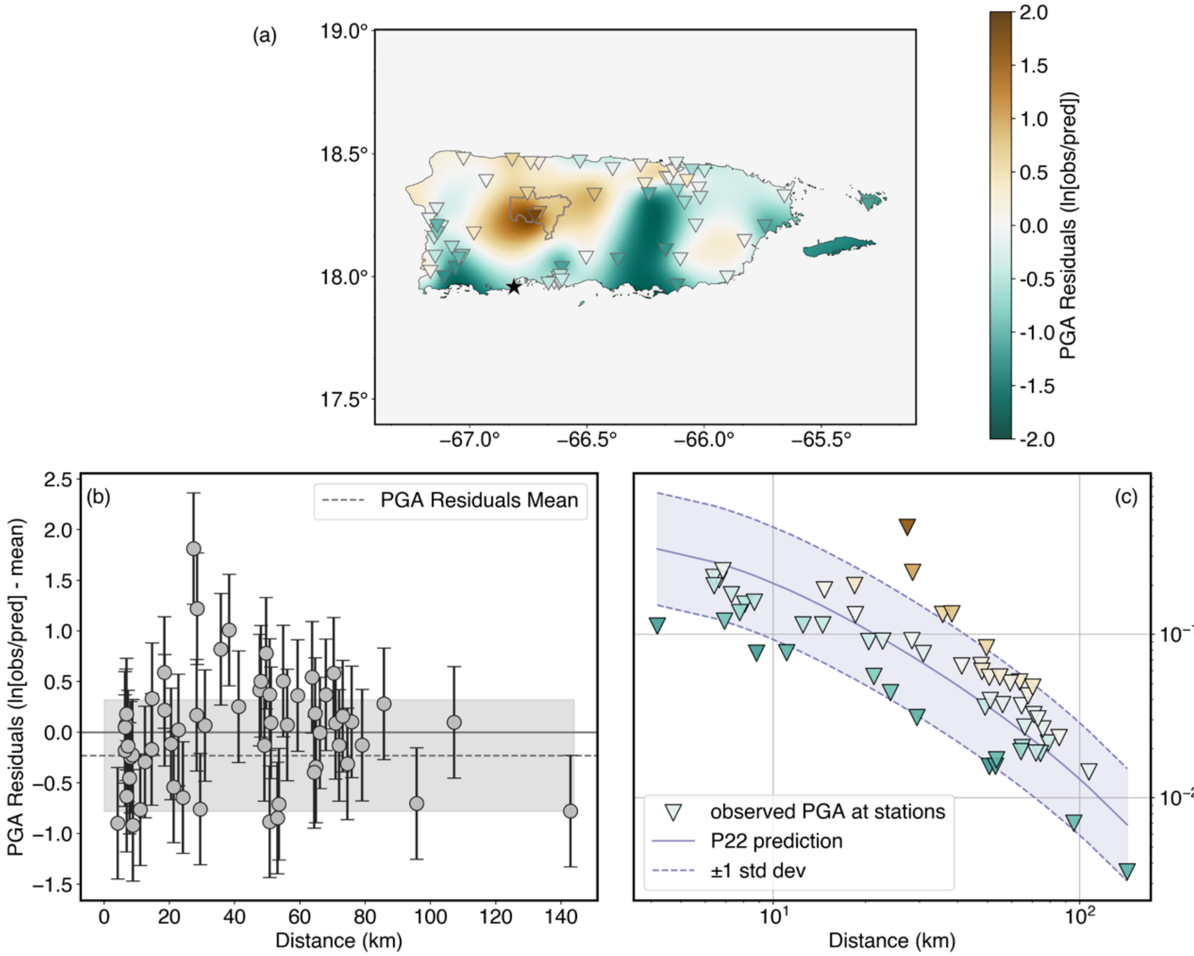

Figure 2.S4. Residuals analysis using the Parker et al. (2022) (P22) ground motion model (GMM). (a) Map shows the location of strong-motion rock sites with colored peak ground acceleration (PGA) residuals; the polygon within Puerto Rico shows the municipality of Utuado, and the black star denotes the mainshock epicenter. (b) PGA residuals assuming mean as a function of rupture distance using the closest distance from a site to the source (Rrup); gray dash line shows mean PGA value, and gray area shows mean plus or minus one standard deviation. (c) PGA observed values with colored PGA residuals as a function of rupture distance in natural log space; purple area shows predicted PGA values plus or minus one standard deviation as dashed lines from GMM assuming hard rock site.

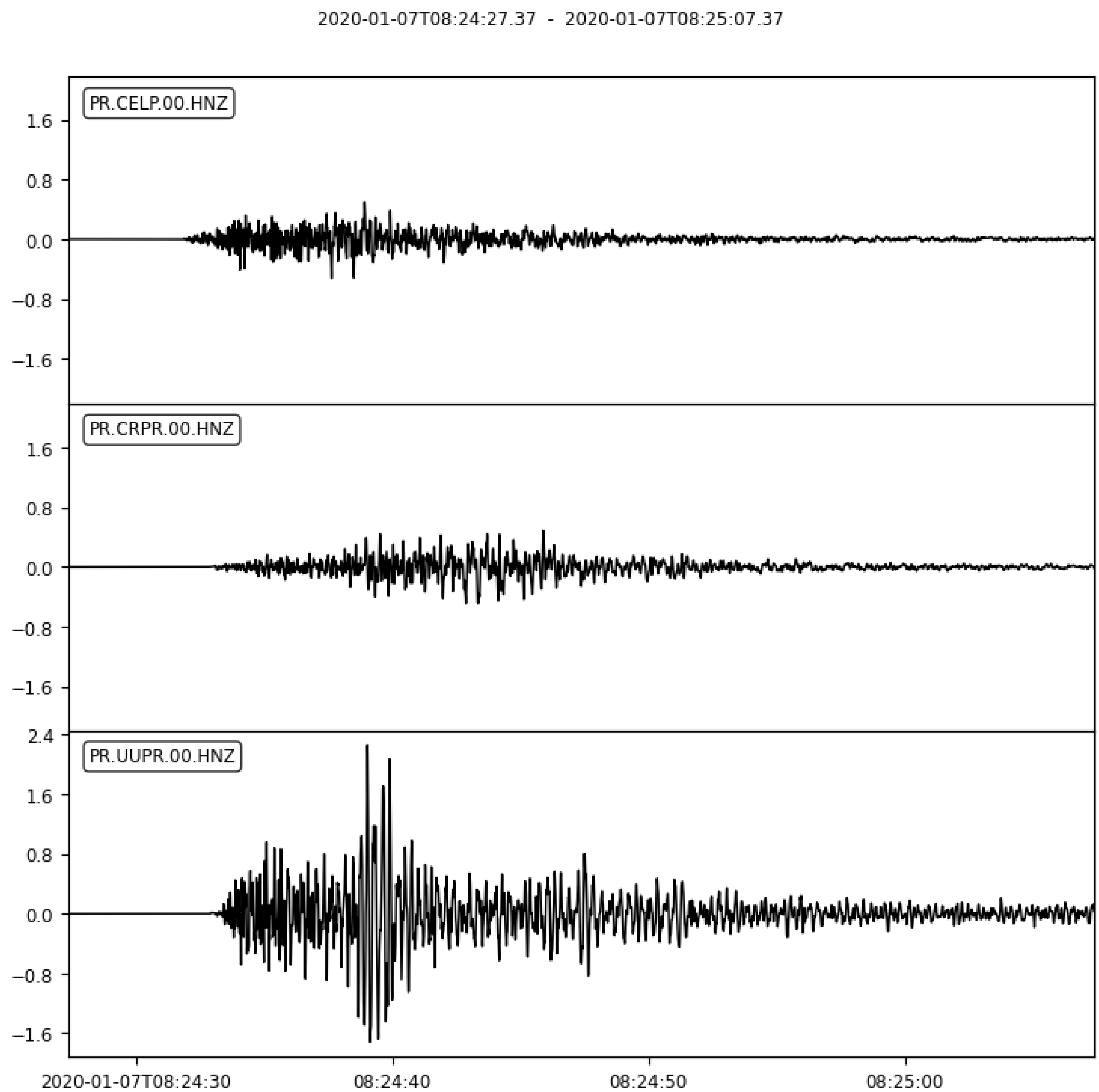

Figure 2.S5. Site amplification effect in central Puerto Rico. Each panel shows strong motion waveforms for three Puerto Rico Seismic Network (PRSN) accelerometers with the same instrument and at similar epicentral distances from the mainshock. Waveforms have instrument response removed and have been converted to acceleration (m/s^2). From top to bottom, distance from station to epicenter for CELP (Ponce, Puerto Rico) is 27.72 km, CRPR (Cabo Rojo, Puerto Rico) is 32.05 km, and UUPR (Utuado, Puerto Rico) is 33.98 km. The site amplification effect at the Utuado station is evident in the third panel, showing approximately 4 times higher amplitude than the other two stations.

Text 2.S1. Earthquake dimensions. We obtained the earthquake rupture length (*L*) and width (*W*) probabilistic scaling laws from Blaser et al. (2010) for each segment of the mainshock. The *L* and *W* for the segments were measured visually from the slip model, where slip is concentrated. For the oblique-normal fault segment, *L* is approximately 13.8 km (–1.4 standard deviations from the mean), and *W* is approximately 11.3 km (–0.1 standard deviations from the mean). For the strike-slip fault segment, *L* is approximately 22.5 km (0.5 standard deviations from the mean), and *W* is approximately 8.8 km (0.1 standard deviations from the mean). When calculating the aspect ratio (L/W) for both segments, we obtained $\log_{10}$ values of 1.1 and 1.43, respectively. These values indicate that the first segment exhibits a more circular, condensed rupture, while the second segment resembles an elongated feature, with the length being greater than the width.

CHAPTER 3

EARTHQUAKES SOURCE SCALING AT SUBFAULT SCALES

This chapter is in preparation to be submitted for publication in collaboration with my advisor, Diego Melgar, who helped conceptualize and design the study, and offered editorial feedback. I drafted the initial manuscript, conducted the analyses, and created figures shown here except for figures illustrating rupture styles and comparison that were modified from material provided by my advisor.

3.1. Introduction

Characterizing the relationships among earthquake source parameters and event size remains a fundamental pursuit in seismology (Somerville et al., 1999; Mai & Beroza, 2000; Ye et al., 2016; Melgar & Hayes, 2017). Scaling laws provide a framework for describing generalized rupture behavior, linking earthquake observations to underlying dynamics and potential predictability. A common working framework is self-similarity (Aki, 1967), which holds that earthquake sources are scale-invariant, meaning that the physical processes remain similar across magnitudes and scale by a constant factor. With the growing number of well-recorded earthquakes—from teleseismic (Ye et al., 2016; Melgar & Hayes, 2017) to strong motion (Mai & Thingbaijam, 2014) and geodetic observation (Shea & Barnhart, 2022), kinematic models of large earthquakes are often derived using heterogeneous datasets and methodologies. Such variability is unavoidable, as instrumentation evolves, analytical techniques improve, and data availability may be limited by tectonic setting (e.g., offshore trenches) or restricted access by local policies. As a result, establishing consistent scaling laws is increasingly challenging.

Building on this foundation, we analyze the global archive of finite-fault models produced by the U.S. Geological Survey–National Earthquake Information Center (USGS–NEIC), as initially explored by Melgar & Hayes (2017). We extend their work by incorporating 115 additional events, including those that occurred after their study, as well as events more recently processed by the USGS-NEIC (e.g., the **M**9.1 2004 Sumatra earthquake) or revisited as part of this analysis (e.g., the **M**9.1 2011 Tohoku earthquake). This expanded dataset enables us to identify general trends across the seismic spectrum (**Figure 3.1**) and examine rupture behavior at the subfault scale. We are particularly interested in the scaling of source parameters for moderate-to-large earthquakes, which are difficult to characterize because of the complexity and nonlinearity of rupture processes. In attempts to simplify or linearize the problem, it is often necessary to assume certain parameters to be constant, such as rise time or rupture velocity. Our goal is to evaluate source parameters such as slip, rise time, and slip rate that we can directly solve for using a nonlinear inversion method, and to test whether the data are consistent with self-similarity at general (i.e., mean values) scale and what happens at local (i.e., subfaults) scale.

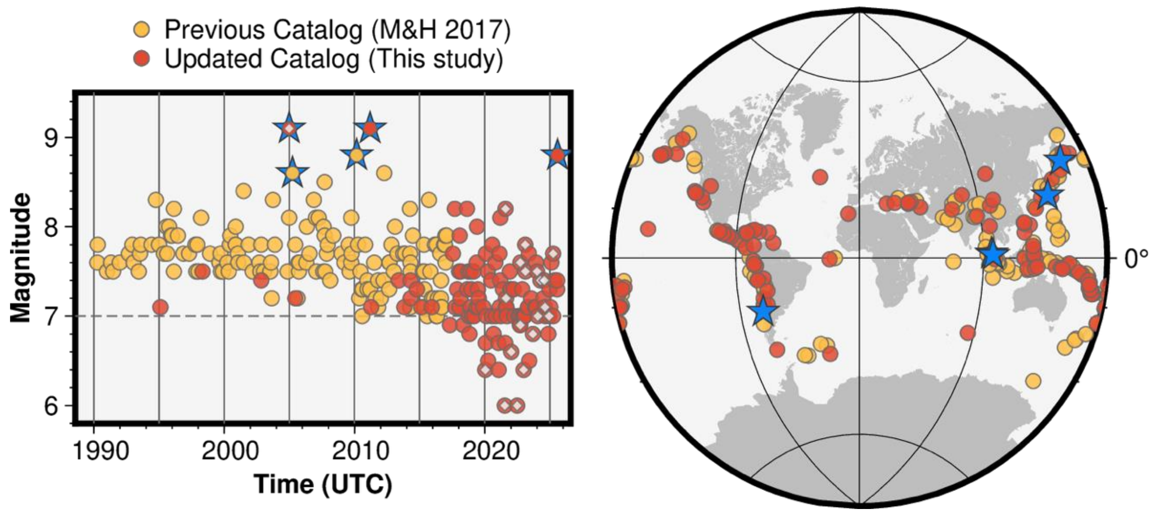

Figure 3.1. Magnitude time series and geographic view of the NEIC Finite-Fault model database. Events from the Melgar & Hayes (2017) catalog (yellow circles) and the expanded catalog presented in this study (red-orange circles) are shown. After the NEIC finite-fault code was upgraded to include regional data (i.e., strong motion, GNSS and InSAR observation), events with mixed datasets (light colored diamonds) are highlighted in the magnitude time series. Vertical gray lines indicate regular temporal intervals of every 5 years. Stars (blue) show the top five largest events recorded in the database.

The limitations of resolving rise time in finite-fault inversions have been explored from both methodological and physical perspectives. For instance, Konca et al. (2013) assessed how accurately kinematic inversions using seismic and geodetic data can recover slip, rise time, and rupture velocity from dynamic rupture simulations. Their results revealed strong trade-offs among these parameters, showing that rise time is difficult to resolve due to regularization effects, highlighting the non-uniqueness of kinematic solutions. Expanding on this, Somala et al. (2014) quantified the physical limits imposed by network geometry and rupture kinematics, demonstrating that for sub-Rayleigh ruptures, rise times shorter than about 2 s can only be resolved with station spacing of roughly ≤ 5 km, whereas supershear ruptures are better resolved at coarser spacing (up to few tens of kilometers) because the energy decay is much slower. Here, we use three independent studies as a validation step to evaluate the consistency of the recovered source parameters.

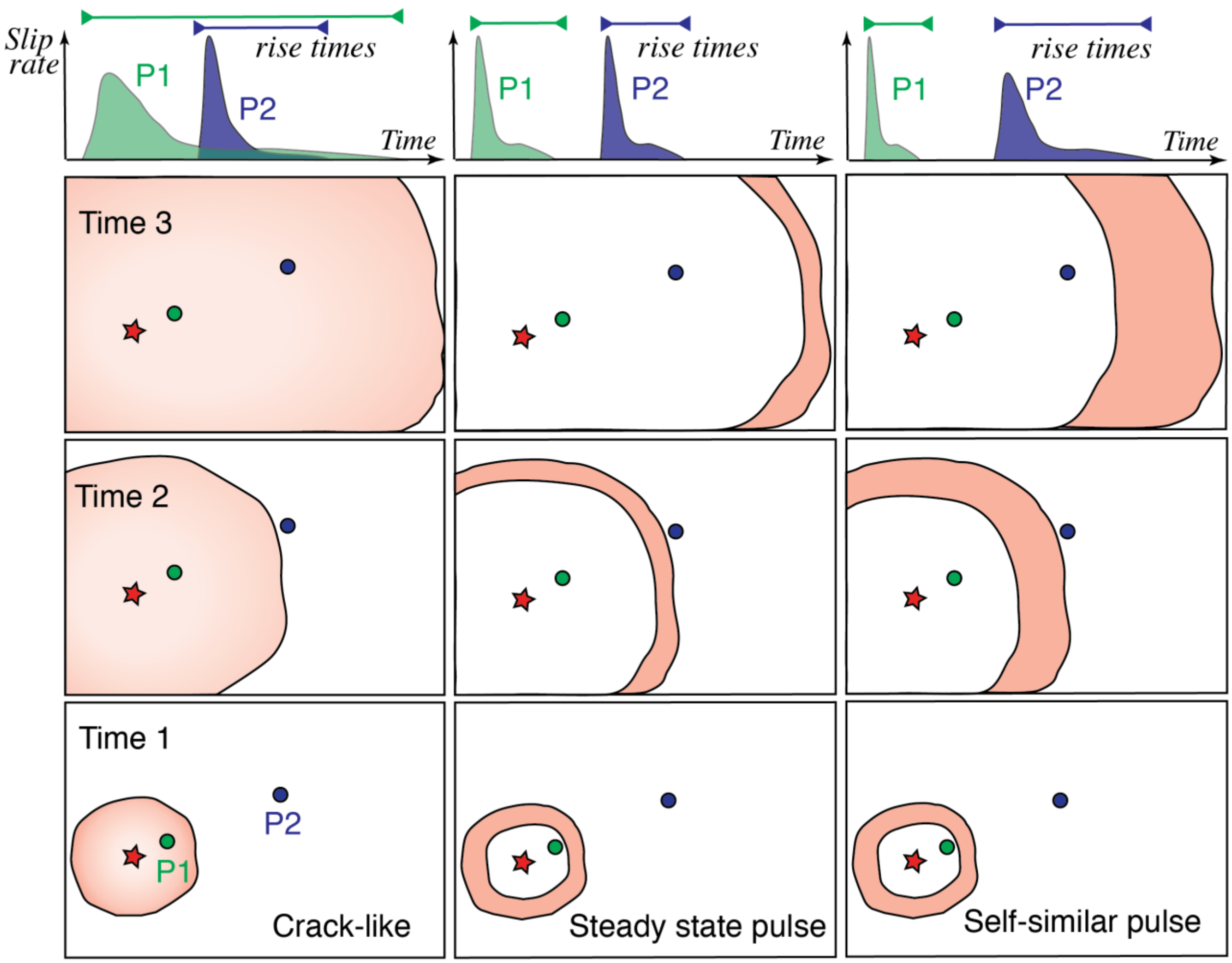

Figure 3.2. Earthquake rupture styles. Each column illustrates an end-member rupture behavior, ranging from crack-like to pulse-like: (1) crack-like, (2) steady-state pulse, and (3) self-similar pulse. The top row shows the slip-rate function and the corresponding time evolution of slip, with two reference time points (P1 and P2) indicated. The remaining three rows present snapshots of rupture propagation through time, from Time 1 (bottom) to Time 3 (top). In the crack-like case (first column), the rupture front expands continuously and terminates only when the earthquake ends. In contrast, the pulse-like ruptures (second and third columns) exhibit both a propagating front and a healing front: the steady-state pulse maintains a constant width, whereas the self-similar pulse grows as the rupture evolves.

Seismologists often distinguish between two rupture styles: crack-like (Kostrov, 1964) and pulse-like (Brune, 1970; Heaton, 1990). These models describe how slip evolves on the fault as rupture progresses (**Figure 3.2**). In a crack-like rupture, a single rupture front propagates along the fault until the earthquake terminates. The slip duration at a given point extends from the arrival of the rupture front until rupture arrest, lasting close to the total source duration. In contrast, a pulse-like rupture behaves as a “self-healing” slip pulse. The fault slips briefly as the rupture front passes, followed by a healing front that halts slip so that its duration at a point is only a fraction of the total source duration. Dynamic rupture simulations further demonstrate that pulse-like ruptures can occur in different forms (Gabriel et al., 2012). Decaying pulses weaken with distance, growing pulses strengthen as they propagate, and steady-state pulses maintain nearly constant properties. Which type develops depends primarily on the background stress and the size of the nucleation region.

Why does the distinction matter? Because it shapes both rupture dynamics and the characteristics of ground shaking (Heaton, 1990; Ben-Zion, 2001; Wang & Day, 2017). A crack-like rupture releases energy gradually over an extended interval, whereas a pulse-like rupture concentrates release into short bursts. These differences influence the amount, timing, and frequency content of the seismic energy radiated from the fault. Crack-like ruptures, by sustaining slip for most of the source duration, are associated with longer-period signals and generally lower ground motions. Pulse-like ruptures, in contrast, release energy in short bursts that radiate high frequencies, producing stronger ground motions.

3.2. Finite Fault Database and Modeling

Finite-fault models were obtained from the USGS–NEIC database, which includes events from 1990 to 2025, concluding with the **M**8.8 Kamchatka earthquake on 29 July 2025 (**Figure 3.1**). These models are routinely produced, with human oversight for general quality assurance and control. For large events, there can be several updates, sometimes weeks or months after the event, as new information and observations become available. The catalog of Melgar & Hayes (2017) is here expanded by ~77% (from 149 to 264 events), broadening the magnitude range to span **M**6 - **M**9. The augmented catalog incorporates 20 events with regional data (strong motion, GNSS and InSAR observations), thereby improving coverage at moderate magnitudes (**M**6s).

The legacy NEIC inversion code for finite-fault modeling initially relied solely on teleseismic data for earthquakes of **M** $\geq$ 7 (Hayes, 2017). In 2021, it was updated to integrate regional datasets—including static and high-rate GNSS, InSAR, and strong-motion, where available—by implementing WASP (Wavelet and Simulated Annealing SliP; Koch et al., 2024) software as described in Goldberg et al., (2022). WASP employs a nonlinear inversion approach based on Ji et al. (2002), as used in the legacy version, and the framework from Koch et al. (2019), to jointly invert teleseismic and regional observations. On the discretized fault plane, the inversion estimates slip amplitude, rake (slip direction), rise time, and rupture onset time for each subfault. The time history of slip is described by an asymmetric cosine source time function, which represents the slip-rate evolution. As a result of these innovations, the USGS–NEIC dataset now includes joint inversions of several significant recent and past events, such as the 2004 **M**9.1 Sumatra earthquake, which combined teleseismic data and GNSS static offsets to model the longest fault rupture on record (~570 s). For this study, we reprocessed the 2011 **M**9.1 Tohoku earthquake using teleseismic data only to investigate constraints in rise time values (more details in following section) and included the 2020 **M**6.4 southwestern Puerto Rico mainshock (Solares-Colón et al., 2025) inverted with WASP using teleseismic and regional data, filling a gap in the mid-**M**6 magnitude range.

3.3. Non-Linear Inversion Method Validation

In this work we present results of earthquake source scaling properties at sub-fault scales. An important question is whether these source properties retrieved by WASP are reliable and consistent with what is imaged using other independent approaches. To assess this, we selected three finite-fault models developed with independent methodologies for comparison. It is important to note that the vast majority of slip models in the literature are obtained through linearized inversion approaches, which do not reliably retrieve key kinematic parameters such as rise time. We therefore focus on models derived from fully non-linear approaches. Two of the selected finite-fault models follow Bayesian methods described in Minson et al. (2014) applied to the 2011 **M**9.1 Tohoku (Minson et al., 2014) and the 2014 **M**8.2 Iquique (Duputel et al., 2015) earthquakes. The third model implements the Bayesian Earthquake Analysis Tool (BEAT; Vasyura-Bathke et al., 2020), as applied to the 2021 **M**7.4 Maduo earthquake (Suhendi et al., 2025). In contrast to WASP's asymmetric cosine source-time function, the Minson et al. (2014) inversions adopt a triangular slip-velocity function, while the BEAT inversion used here assumes a half-cosine source-time function (Lay et al., 2010). These differences could potentially lead to distinct representations of slip-rate evolution across the three methods to evaluate.

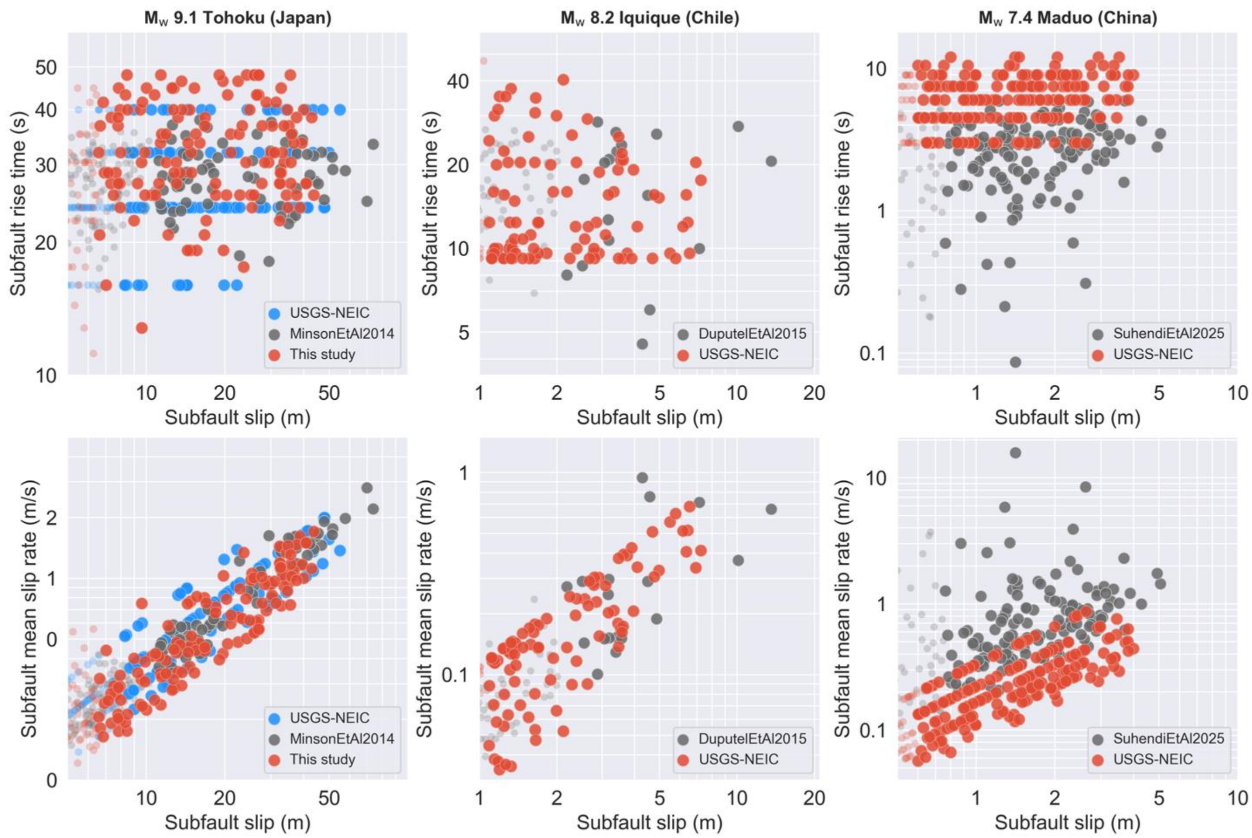

Figure 3.3. Comparison across independent rupture models for three earthquakes: **M**9.1 Tohoku 2011, **M**8.2 Iquique 2014, and **M**7.4 Maduo 2021. Each column corresponds to one event; the top row shows subfault slip versus rise time, and the bottom row shows subfault slip versus mean slip rate for the same datasets. Gray markers denote published models (Tohoku: Minson et al., 2014; Iquique: Duputel et al., 2015; Maduo: Suhendi et al., 2025), and red–orange markers show the USGS–NEIC products. For Tohoku, we also include a re-run (red–orange markers) of the NEIC (blue markers) inversion to assess striking artifacts related to restrictive rise-time bounds. Subfaults with slip ≥ 15% of the event peak slip are emphasized; lower-slip patches are shown smaller and with increased transparency for context.

Figure 3.3 shows the comparison of the NEIC finite-fault models from the catalog used in this study with corresponding models derived from alternative approaches for subfaults with ≥ 15% of the event maximum slip. While some variations are evident, the important result is that general trends remain consistent, with similar patterns observed for rise time (no correlation with slip) and slip rate (high correlation with slip). For the great Tohoku earthquake, one of only two **M**9 events in the catalog, the currently available USGS-NEIC model shows an evident streaking effect (blue circles in first column of **Figure 3.3**) due to the inversion being parametrized in a way that allowed only a limited set of rise-time values when it was carried out. To address this, we re-inverted this event with WASP, allowing for a broader range of rise-time values and using teleseismic data only, to be consistent with the original release (orange-red circles in first column of **Figure 3.3**). For the Maduo earthquake, discrepancies between the NEIC teleseismic-only solution and regionally constrained models are more apparent. However, if we further restrict the comparison to subfaults with rise time ≥ 1 s—below which teleseismic and InSAR data offer limited constraints due to their low-frequency sensitivity (as discussed in the introduction) and static nature (Funning et al., 2013), respectively—the rise time and slip rate patterns show closer agreement with those observed in the other two events. As noted by Funning et al. (2013), InSAR alone cannot constrain temporal of parameters of a rupture, though geodetic observations complement seismic observations in joint inversions as also demonstrated in Goldberg et al. (2022). Still, so short rise time values remain difficult to resolve without near-field strong-motion and sufficient station density (Somala et al., 2014) .

We emphasize that the NEIC models used for validation are teleseismic-only, whereas the comparison models more extensively examine and incorporate regional strong-motion, GNSS, InSAR, and even tsunami data in the case of Tohoku. Despite these differences in data coverage and uncertainties in fault plane geometry, the NEIC models still yields source parameter ranges consistent with independent models. Such consistency validates WASP results and supports the use of the catalog for first-order analyses of earthquake source scaling relations.

3.4. Results & Discussion

3.4.1 General Behaviors: Source Scaling with Seismic Moment and Self-Similar Assumption

In analyzing source parameters, we first revisit self-similar assumption that earthquakes are scalable by a constant factor, allowing prediction of source characteristics from event size. Each source parameter is modeled as a power-law function of seismic moment, as follows:

$$\log_{10}(Y) = a + b\log_{10}(M_0), \qquad (1)$$

where Y is the source parameter of interest, $M_0$is seismic moment, a is a constant, and b is the scaling exponent. The scaling exponent b is estimated as the slope of a linear fit in log–log space, based on the fault-averaged source parameter values for each parent earthquake. Self-similarity is assessed by comparing the fitted slope with the expected value ($b \approx 1/3$ for slip and rise time; $b \approx 0$ for slip rate).

Source parameters are plotted as a function of seismic moment for all subfaults within each parent earthquake (colored circles in **Figure 3.4**). Note that we used subfaults with ≥ 20% of the event slip maximum to minimize the influence of inversion artifacts and retained only nonzero values for rise time, onset time, and hypocenter distance. To highlight updated catalog from Melgar & Hayes (2017), hereafter referred to as M&H17, events added in this study are plotted in warm colors, while those that appear in both catalogs are shown in cool colors. Now, for the average over the entire fault area of a given earthquake (colored diamonds in **Figure 3.4**), rise time scales more weakly than the cube root of seismic moment (b = 0.263), indicating a more sublinear trend towards pulse-like behavior, and slip scaling remains self-similar (b = 0.343). Consequently, slip rate scaling flattens, and no longer scales with earthquake size in a meaningful way as in M&H17. Such scaling behavior is consistent with its dependence on both slip (s) and rise time (τ) under self-similarity assumptions, where slip rate is defined as $\dot{s} = s/\tau$. This relation assumes constant stress drop and rupture geometry: as seismic moment increases, fault length grows, and both slip and rise time increase in proportion to that length (Somerville et al., 1999). As a result, the observed slight increase in slip rate indicates that rise time grows more slowly (i.e., shorter τ) relative to slip, as the proportionality between slip and rise time is no longer preserved. This observation does not necessarily imply slower rupture propagation but rather a more pulse-like character on average, in which larger earthquakes release slip more rapidly at each point, even though the total rupture duration could last longer.

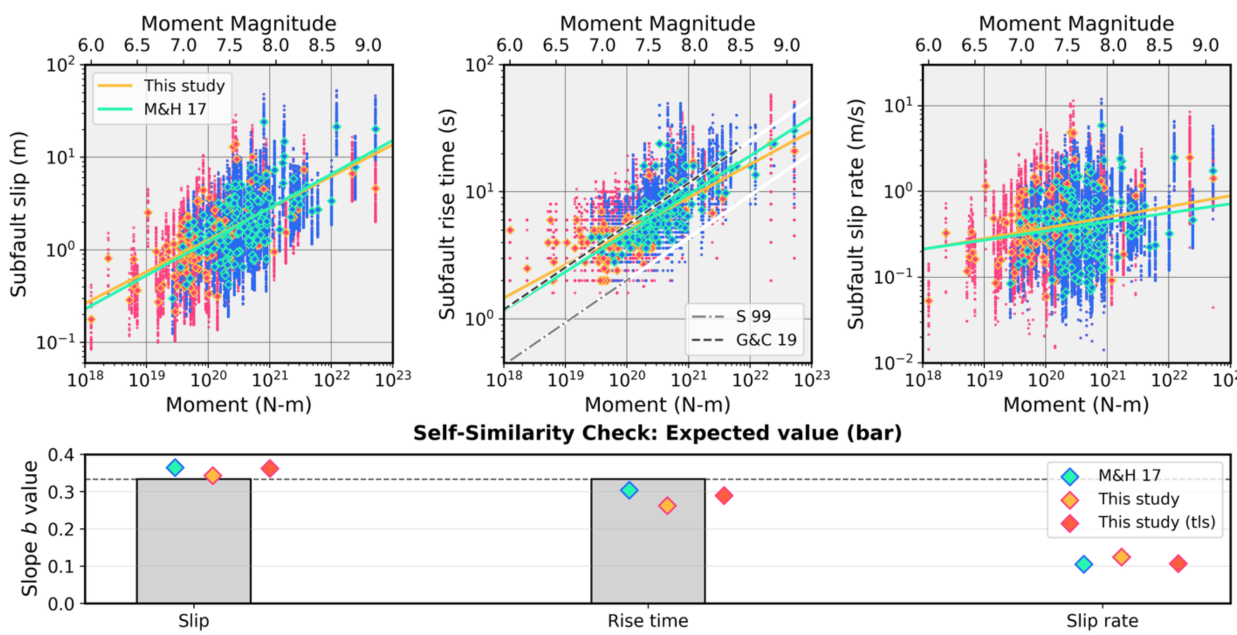

Figure 3.4. Testing self-similarity of earthquake source parameters. Top row: log–log scatter plots of subfault slip (left), rise time (middle), and slip rate (right) versus seismic moment of the NEIC finite-fault database. Melgar & Hayes (2017) catalog is shown in cool colors (blues, cyan), while newly added events in this study are shown in warm colors (dark pink and yellow). Circles represent subfaults with >20% of the maximum slip of each parent earthquake, lines show fitted linear trends through all subfaults, and diamonds indicate mean values. Rise-time scaling from Somerville et al. (1999): S 99 and from Gusev & Chebrov (2019): G&C 19; white lines show extrapolated trends toward larger magnitudes. Bottom row: slope b value (scaling exponent) estimates

of the log–log regressions for each source parameter. Bars indicate the expected self-similar value (1/3 for slip and rise time; 0 for slip rate), and scatter markers show the slope b value for each catalog. This summary plot highlights how scaling behavior may deviate from self-similar expectations across different magnitude ranges and between catalogs.

Compared with the scaling of average rise time proposed by Somerville et al. (1999) (hereafter refer to as S99; gray line in middle panel of **Figure 3.4**) several nuances are worth noting. S99 used rupture models primarily inferred from low-pass filtered strong motion data, the proximity of these near-fault recordings provides finer temporal resolution than the teleseismic waveforms that predominate in the NEIC finite-fault models database. Their models thus yield and can capture smaller rise times than those inferred from teleseismic inversions. The differences in data bandwidth, magnitude range, and tectonic setting partly explain why trends do not overlap as discussed by M&H17 and by extension observed here. S99 findings correspond to the kinematics of crustal earthquakes recorded locally, whereas the global catalogs from the NEIC finite-fault models database represents longer-period behavior dominated by large subduction events.

However, Gusev & Chebrov (2019) later reanalyzed strong-motion derived finite-fault models from the SRCMOD catalog (Mai & Thingbaijam, 2014) and compared their results with both earlier studies (S99 and M&H17). By using a consistent measure of average rise time across source elements (i.e., subfaults) and expanding the magnitude range, they found that rise time estimates from modern strong-motion rupture models converge toward the longer rise times consistent with teleseismic analyses. This reconciliation implies that the offset between datasets likely reflects methodological choices instead of inherent physical differences, as noted by Gusev & Chebrov (2019), in how rise time is defined for asymmetric slip pulses. They observed that earlier inversions often inferred rise time based on the time to peak slip rate, providing a truncated measure of source duration and consequently yielding shorter rise time values. By comparison, newer analyses resolve the full slip-history evolution, from onset to arrest, producing longer rise time estimates that capture the temporal complexity of slip across the fault. In this context, the evolution from S99 to Gusev & Chebrov (2019) represents a methodological shift, finding consistency of the $\tau_r \propto M_0^{1/3}$ scaling across data types. Therefore, the catalogs are complementary rather than directly comparable, highlighting different portions of the earthquake spectrum, from near-field behavior to global rupture characteristics.

Overall, pulse-like ruptures remain favored over crack-like ruptures, with rise times generally shorter than the total source duration. This is consistent with the findings from M&H17, who also explored whether the WASP inversion framework tended to bias results toward pulse-like ruptures. As in this study, their normalized rise-time distributions were skewed toward the lower end of the allowed range (**Figure 3.S1** Supplementary Information). They further examined high-rate GNSS data and found that stations near large events consistently showed static offset growth durations shorter than the total source duration (refer to **Figure 3** in Melgar & Hayes, 2017), reinforcing the interpretation of predominantly pulse-like rupture behavior. However, departures from self-similar scaling do emerge, trending toward smaller scaling exponent b. The tendency is more pronounced when teleseismic and regional datasets are combined. The impact of incorporating regional data on inferred source-parameter scaling remains to be determined. Retrospective analyses of finite fault models, including regional observations where available, will provide a more complete picture.

3.4.2 Behaviors at Sub-Fault Scales: Source Scaling with Slip

Local variations are important when modeling earthquakes. A popular assumption, especially for kinematic and semi-stochastic modeling, is that the local rise time τ_r is proportional to the square root of slip s scaled by a constant k, and expressed as

$$\tau_r = k\sqrt{s}. \qquad (2)$$

In this formulation, larger slip patches are expected to exhibit longer rise times. This slip–rise time correlation was first introduced by Aagaard et al. (2008) as a physically based assumption calibrated against observations of the 1989 Loma Prieta earthquake to simulate ground motions. It was later adopted by Graves & Pitarka (2010) in stochastic and kinematic simulations to reproduce those physical constraints in synthetic ruptures and subsequently implemented in finite-fault modeling frameworks (e.g., Melgar et al., 2016). Here, we examine whether this empirical relationship holds across the NEIC finite-fault catalog and how it manifests across magnitudes and subfault scale.

Figure 3.5 shows rise time and slip rate as a function of slip for all subfaults in the database. If we focused on the subfaults of the largest events (**M** ≥ 8.8; green stars in scatterplots of **Figure 3.5**): (1) rise times shows no evident dependence on slip and (2) slip rates increase linearly with slip. The patterns observed here are consistent with those in **Figure 3.3**: rise time shows no clear correlation with slip, whereas slip rate correlates strongly with slip. Although the rise time scatter plot offers limited clarity, the expected slip–rise time correlation ($\tau \propto \sqrt{s}$) is notably absent.

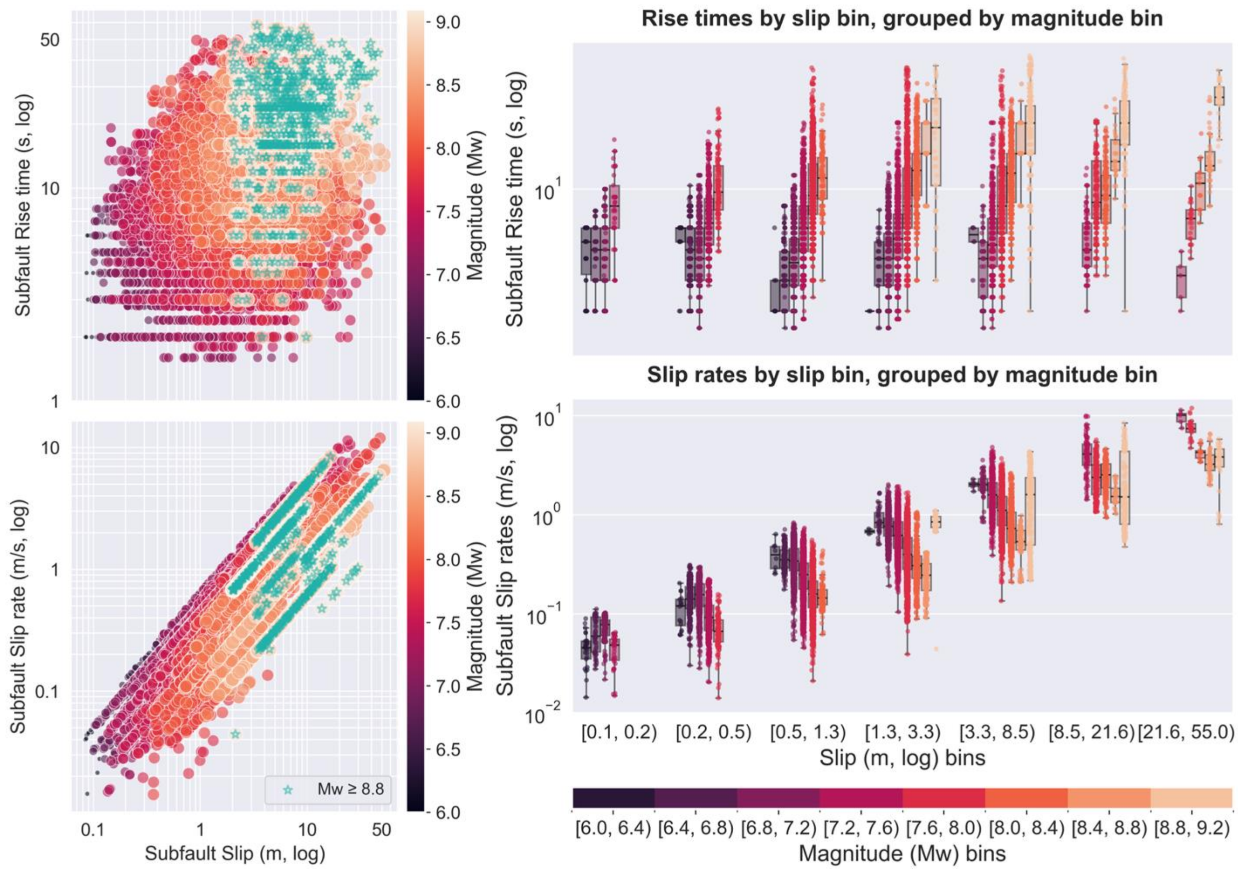

Figure 3.5. Local behaviors of source parameters at the subfault scale. The first panel shows rise time (top) and slip rate (bottom) as functions of slip, with markers colored by magnitude; green stars represent subfaults of the largest events ($M \geq 8.8$). The second panel presents boxplots of the same parameters, where subfaults are first binned by slip, and within each bin values are grouped by magnitude—corresponding to the scatter plots in the first panel.

To further examine these relationships, we mapped scatterplot data to boxplots, illustrating how rise time and slip rate vary with slip across magnitudes (**Figure 3.5**). Rise time distributions vary slightly with slip when comparing to same magnitude bin across slip bins, but within each slip bin, rise time grows with magnitude. This shows that self-similarity holds internally, with longer rise times and larger slip values continuing to scale with magnitude, yet it differs from the expected slip–rise time correlation that rise time scales with local slip. In contrast, slip rate distributions increase with slip when comparing to same magnitude bin across slip bins. More interestingly, slip rates show the opposite trend within slip bins, tending to decrease with magnitude, except for very large to great earthquakes that increases. On the local scale, observations indicate that larger slips are accommodated by higher slip rate (i.e., moving faster), rather than through longer slip durations (i.e., wider pulses). These findings depart from results of rupture-dynamic simulations, which show a strong correlation between slip and rise time but a weak correlation between slip and slip rate (e.g., Schmedes et al., 2010).

We also subdivided the dataset by fault type to assess potential biases and local processes in source parameters of interest as a function of slip for all subfaults in the database (refer to **Figures 3.S2** for rise times and **3.S3** for slip rates in Supporting Information). While WASP includes fault parameters derived from moment tensor solutions and a velocity model, it lacks explicit geological or topographic constraints. Even so, the results indicate that thrust events are characterized by higher slip and longer rise times than other fault types in the database. This is particularly true for subduction megathrust earthquakes, which have also been shown to exhibit depth dependence (Lay et al., 2012; Kurahashi & Irikura, 2011; Kiser & Ishii, 2012; Melgar et al., 2016; Cárdenas et al., 2023). The elongation of rise times is most pronounced in the shallow portion of the megathrust, where rupture tends to propagate more slowly and radiate less high-frequency energy than at greater depths. In contrast, strike-slip events generally display shorter rise times than thrust events and higher slip rates than other fault type in the database. The simpler geometry of large crustal strike-slip faults allows supershear rupture propagation (Bouchon et al., 2010), in which the rupture front moves faster than the shear-wave velocity and radiates high-frequency energy over greater distances from the source (Andrews, 2010), resulting in shorter rise times and faster slip. Lastly, normal events, smallest subset of the database (48 events), exhibit lower rise times and slip rates relative to other fault types. Quantitative studies of source properties for normal-faulting events are scarcer than for strike-slip events, which are generally easier to parameterize, and for megathrust events, which have received greater attention due to their earthquake size and hazard potential. Although several well-documented normal and normal-oblique events—such as the 2009 **M**6.1 L'Aquila in Italy (not in the database; Cirella et al., 2012) and the 2020 **M**6.4 Southwestern Puerto Rico Seismic Sequence mainshock (included in this database; Solares-Colón et al., 2025) events, demonstrate that moderate earthquakes can produce complex rupture processes, though broader generalizations remain limited.

Considering noise and artifacts inherent in finite-fault inversions, some subfaults exhibit very high slip velocity over 10 m/s across fault types. Dynamic and experimental studies indicate typical upper bounds on slip rate of ~6–10 m/s for crustal, sub-shear events, with higher values possible under supershear or extreme stress conditions (Andrews, 2005; Schmedes et al., 2010; Bizzarri, 2012; Gabriel et al., 2013). This peak slip rate limit emerges from the dynamic coupling between rupture velocity and growth of slip velocity, governed by the final slip, stress drop, and the fracture energy required to sustain propagation. A recent real-world example of a supershear crustal strike-slip earthquake is the 2025 **M**7.8 Myanmar event on the Sagaing Fault. The rupture extended for more than 450 km, with average slip of ~3–6 m, a source duration exceeding 80 s, and reaching rupture speeds of 4–6 km/s (Diao et al., 2025; Melgar et al., 2025; Vera et al., 2025; Wei et al., 2025; Xu et al., 2025; Ye et al., 2025). Closed-circuit television (CCTV) footage from a camera located ~20 m east of the Sagaing Fault and ~120 km south of the hypocenter captured surface rupture and allowed direct estimation of earthquake source properties (Kearse & Kaneko, 2025; Latour et al., 2025). Independent analyses of CCTV footage yielded consistent near-field estimates of fault slip during this event. Both studies found slip amplitudes of ~2.5–3 m, durations of ~1.3–1.4 s, and peak slip velocities of ~3.2–3.5 m/s, providing direct constraints on rupture kinematics. These findings represent a first benchmark for rupture evolution analyses and serve as ground truth for rupture model validation of large crustal earthquakes. They also reveal pulse-like characteristics in large earthquakes, consistent with the general sublinear trend toward pulse-like behavior observed in the NEIC finite-fault database (**Figure 3.4**). The onset or transition to supershear propagation in rupture models varies among studies; however, Latour et al. (2025) inferred that the portion of the rupture observed by the CCTV camera propagated at a locally sub-shear velocity. Based on this interpretation, we could infer that supershear propagation may produce higher peak slip rates than those observed at sub-shear velocity, approaching the upper bound of 6–10 m/s range proposed by dynamic rupture models.

3.4.3 Testing Slip-Rise Time Correlation with Slip

If we assume that rise time scales with local slip, then across magnitudes it remains consistent with the expectation that larger earthquakes exhibit longer rise times, indicating that pulse width increases with slip. However, the dataset at the subfault scale does not support this assumption. Rise time shows no dependence on local slip and remains roughly constant but increases with magnitude, indicating that pulses stay relatively steady (**Figure 3.5**). We then ran a kinematic rupture model with both assumptions to show case (1) with prescribed rise-time correlation (Eq. 2) using the scaling exponent from M&H17 and case (2) with no dependence of rise time on slip.

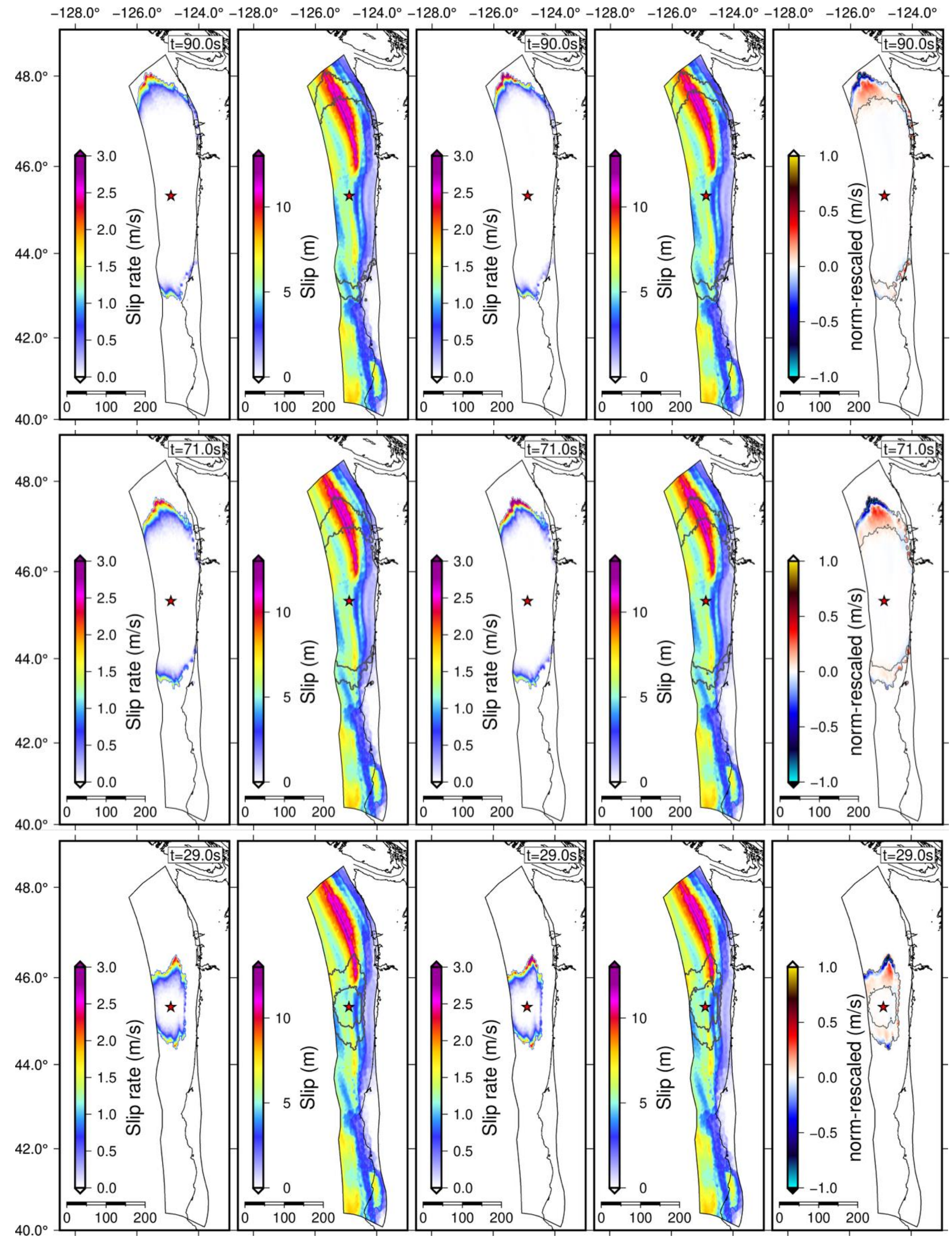

Figure 3.6. Snapshots of the same rupture simulated under two rise-time assumptions: case (1) includes a prescribed correlation between rise time and slip (Eq. 2; scaling exponent from Melgar & Hayes, 2017), whereas case (2) assumes no dependence of rise

time on slip. Each of the three rows shows a different time step in the rupture evolution, with five panels per row: the first two panels show slip rate and slip for case (1); the next two panels show the same quantities for case (2); and the last panel shows the slip-rate difference between them. Blue indicates areas where case (2) produces higher slip rates, and red indicates areas where case (1) produces higher slip rates.

Figure 3.6 shows snapshot of the rupture evolution for both cases side-by-side and difference in slip rates. We find that for case (1), pulse width increases when the rupture front passes through high-slip patches (northern part of the rupture) and decreases in lower-slip regions (more visible towards the southern region of the rupture). In contrast, for case (2), pulse width remains relatively constant when rupture front passes through high/low-slip areas. Although the differences may seem subtle at first, the most notable contrast arises in slip rates, which for case (2) reaches higher values when the rupture front encounters high-slip patches, rather than exhibiting a pulse-widening effect (i.e., longer rise times) as in case (1). High slip rates are linked to stronger ground shaking by generating high-frequency bursts that alter the frequency content of the seismic energy radiated from the fault. These differences are significant because pulse-like ruptures with higher slip rates and shorter pulses (i.e., shorter rise times) have implication for the resulting ground motions affecting regions farther from the source depending on where slip is concentrated and for how we model earthquakes, both of which require further investigation.

3.5. Conclusions

This study analyzes a catalog of 264 finite-fault models produced by the USGS-NEIC to evaluate source properties over a wider range of magnitudes (**M** 6.0–9.1) with a systematic inversion approach. As a validation step, we also compare to other independent finite-fault models for consistency in source parameters ranges. We focus on finite-fault models inferred from non-linear approaches to estimate not only slip distributions but also other source parameters of interest, such as rise time and onset, which allow us to examine rupture kinematics from general behaviors down to the subfault scale. Although these models do not directly resolve local stress or energy, spatial patterns in rise time and slip rate serve as useful kinematic proxies for underlying dynamic processes. Such information becomes increasingly important for downstream applications, including earthquake simulations and predictive frameworks. In describing the general behavior of earthquakes, self-similarity remains broadly consistent, though deviations emerge, with pulse-like ruptures continuing to be favored over propagating-crack models, building on the work of

Melgar and Hayes (2017). However, at a local scale, the common assumption of rise time proportionality to the square root of slip is not sustained by the observations.

As new inversion techniques capable of jointly inverting teleseismic, geodetic, strong-motion, and tsunami data continue to advance reprocessing past well-recorded events remains essential to ensure that legacy earthquakes are represented with modern methods and extending to progressively smaller magnitudes. Retrospective analyses of slip distributions therefore remain essential for assessing the general characteristics of earthquake source parameters.

3.6. Acknowledgments

The material here is based on the U.S. Geological Survey's National Earthquake Information Center (USGS–NEIC) finite-fault products.

3.7. Open Research

The Wavelet and simulated Annealing SliP (WASP) inversion code to obtain slip models is publicly available at GitLab (Koch et al., 2024).

3.8. Supporting Information

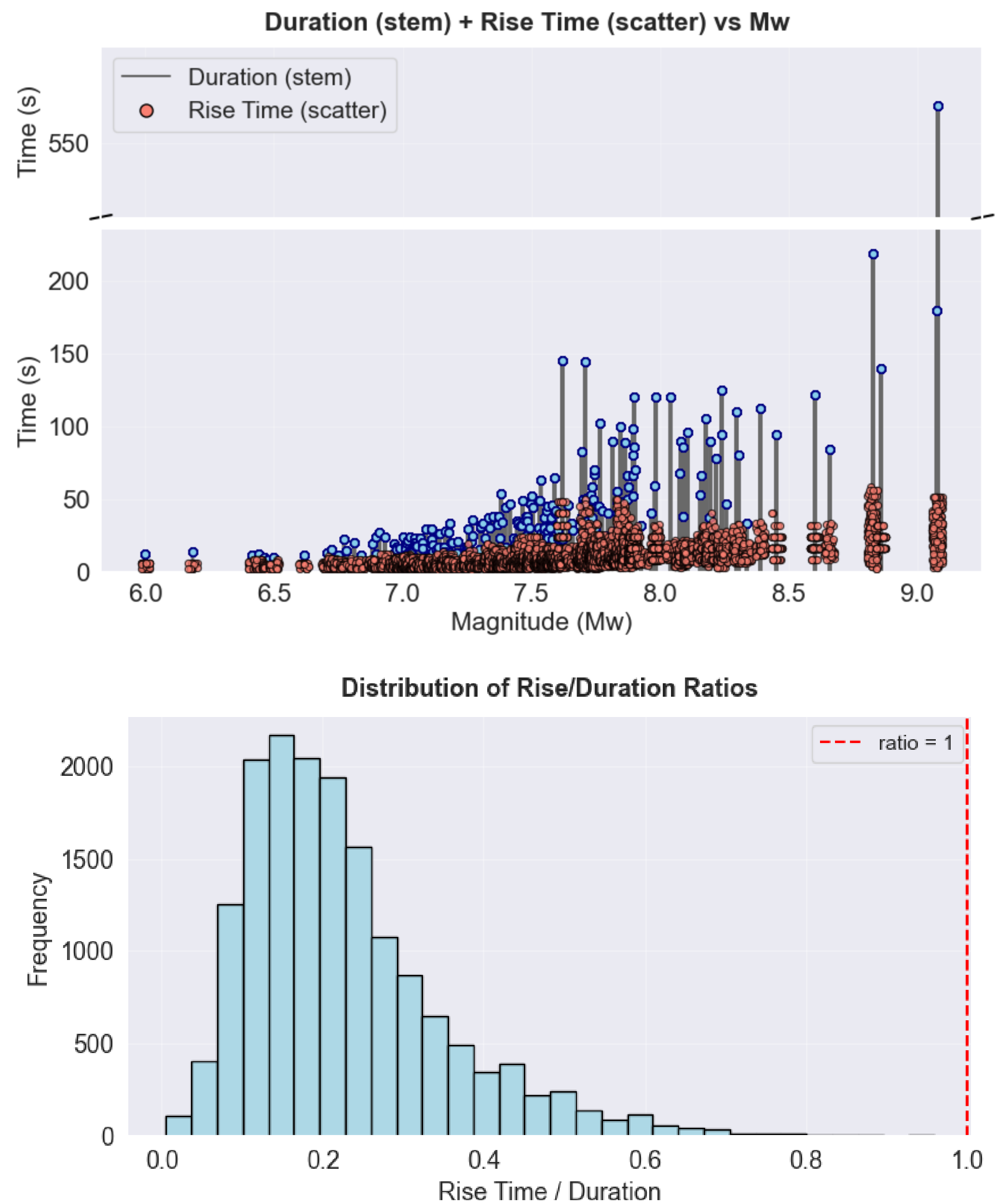

Figure 3.S1. Comparison between rupture duration and local rise time. Top panel shows rupture duration (blue stems) and local rise times (red circles) as a function of moment magnitude (Mw) for all events in the finite-fault model catalog. Both parameters increase with magnitude, though rise times remain systematically shorter than total rupture durations. (Bottom) Histogram of rise-time-to-duration ratios, showing that most subfaults rupture over a fraction (0.1–0.4) of the total event duration (red dashed line marks ratio = 1).

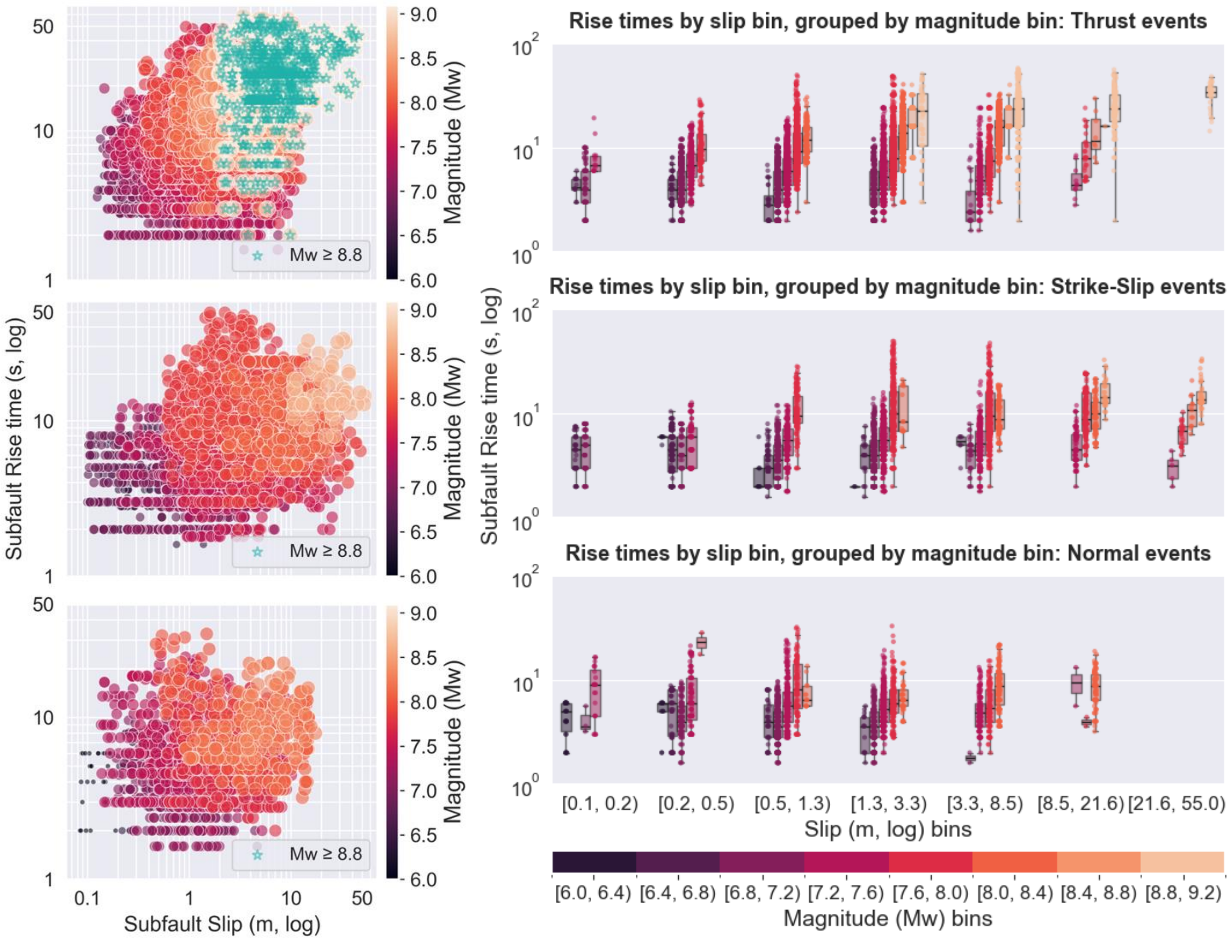

Figure 3.S2. Local behavior of rise time by fault type at the subfault scale. The first panel shows rise time by fault type as functions of slip, with markers colored by magnitude; green stars represent subfaults of the largest events (M ≥ 9). The second panel presents rise time boxplots by fault type, where subfaults are first binned by slip, and within each bin values are grouped by magnitude—corresponding to the scatter plots in the first panel. From top to bottom, rows show thrust, strike-slip, and normal events.

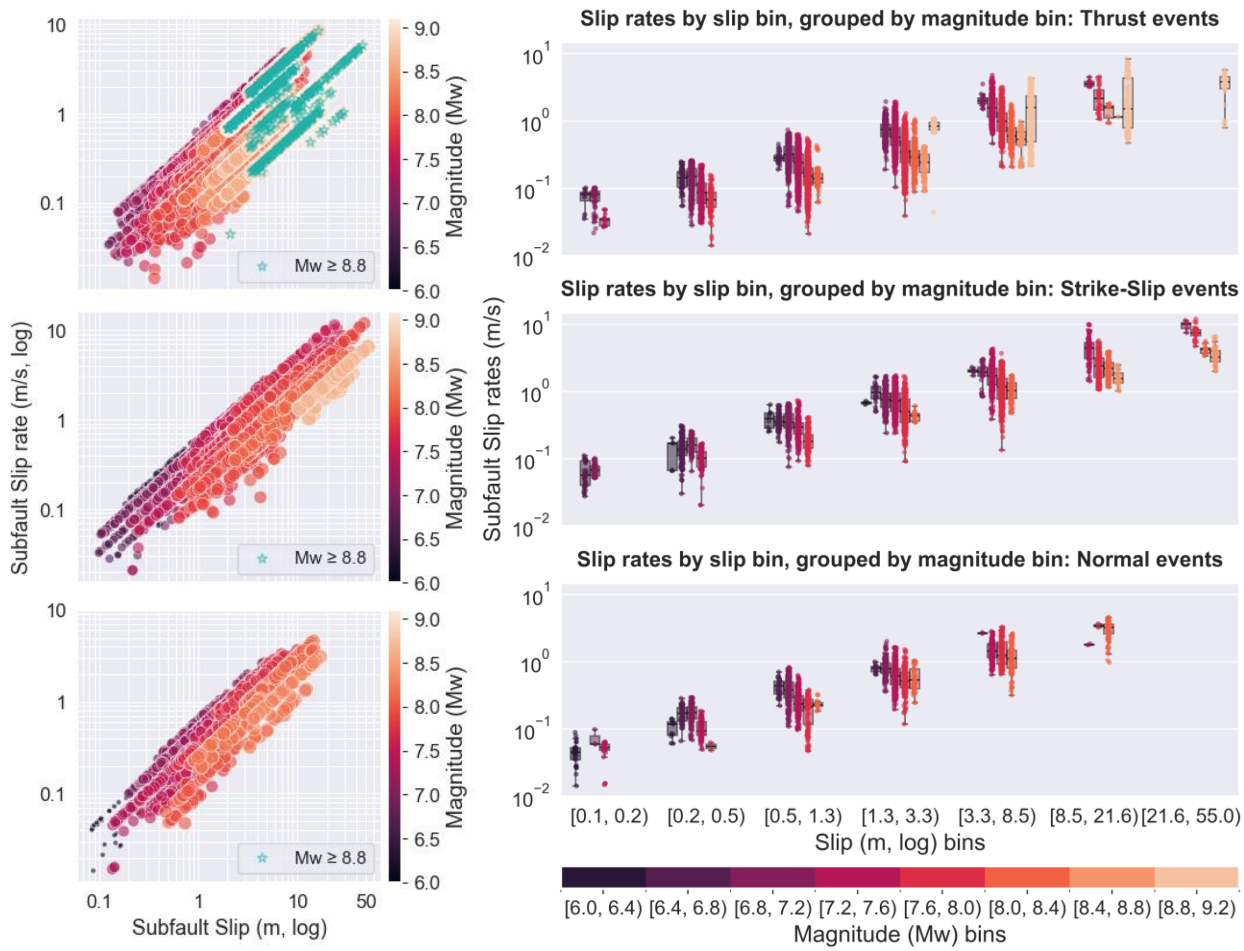

Figure 3.S3. Local behavior of slip rates by fault type at the subfault scale. The first panel shows rise time by fault type as functions of slip, with markers colored by magnitude; green stars represent subfaults of the largest events (M ≥ 9). The second panel presents slip rates boxplots by fault type, where subfaults are first binned by slip, and within each bin values are grouped by magnitude—corresponding to the scatter plots in the first panel. From top to bottom, rows show thrust, strike-slip, and normal events.

CHAPTER 4

USING RUPTURES FROM AN EARTHQUAKE CYCLE SIMULATOR TO TEST GEODETIC EARLY WARNING SYSTEM PERFORMANCE

From Solares-Colón, M. M., Melgar, D., Howell, A., Crowell, B., D'Anastasio, E., Caballero, E., and Fry, B. (2025). Using ruptures from earthquake cycle simulators to test geodetic early warning systems performance. Manuscript accepted for publication in *Seismica*.

4.1. Introduction

Subduction zones are defined by deep trenches, where megathrust events are expected to rupture along the plate interface as stress accumulates over time. While these large earthquakes occur less frequently, they can trigger catastrophic tsunamis that impact coastal communities (e.g., the 2004 Indonesia, 2010 Maule, and 2011 Tohoku earthquakes; Lay et al., 2005; Mori et al., 2011; Vargas et al., 2011), leading to loss of life, structural damage, and other geological hazards such as ground failure. Because large events (**M** > 7) are comparatively rare, the instrumental record contains only limited near-source observations. This makes it difficult to test the effectiveness of rapid-response systems. To address this, researchers either reconstruct historical events (Ammon et al., 2005; Yue et al., 2014; Lay, 2018) or generate synthetic rupture scenarios (Hok et al., 2011; Aguirre et al., 2018; Small & Melgar, 2023) to assess seismic and tsunami hazards in a region of interest. Here, we adopt the latter approach, using synthetic ruptures, which allow us to explore a wider range of magnitudes and specifically test the response of an earthquake early warning (EEW) algorithm in areas where large events are scarce or have yet to occur.

For this study we focused on the Hikurangi subduction zone in New Zealand (**Figure 4.1**), which is located offshore east of the North Island of New Zealand at the southern end of the Kermadec-Tonga subduction system and defined as the boundary between the Pacific plate and the Australian plate. This region is considered an active seismic zone and capable of hosting large earthquakes (Clark et al., 2019; Wallace, 2020). Thus, coastal communities are vulnerable to seismic and tsunami hazards due to their proximity to the fault zone and topography in the area. At the southern end of the Hikurangi subduction margin, it transitions into a strike-slip fault across the South Island. This is the Alpine Fault, a northeast-southwest striking dextral strike-slip fault in the west part of the South Island.

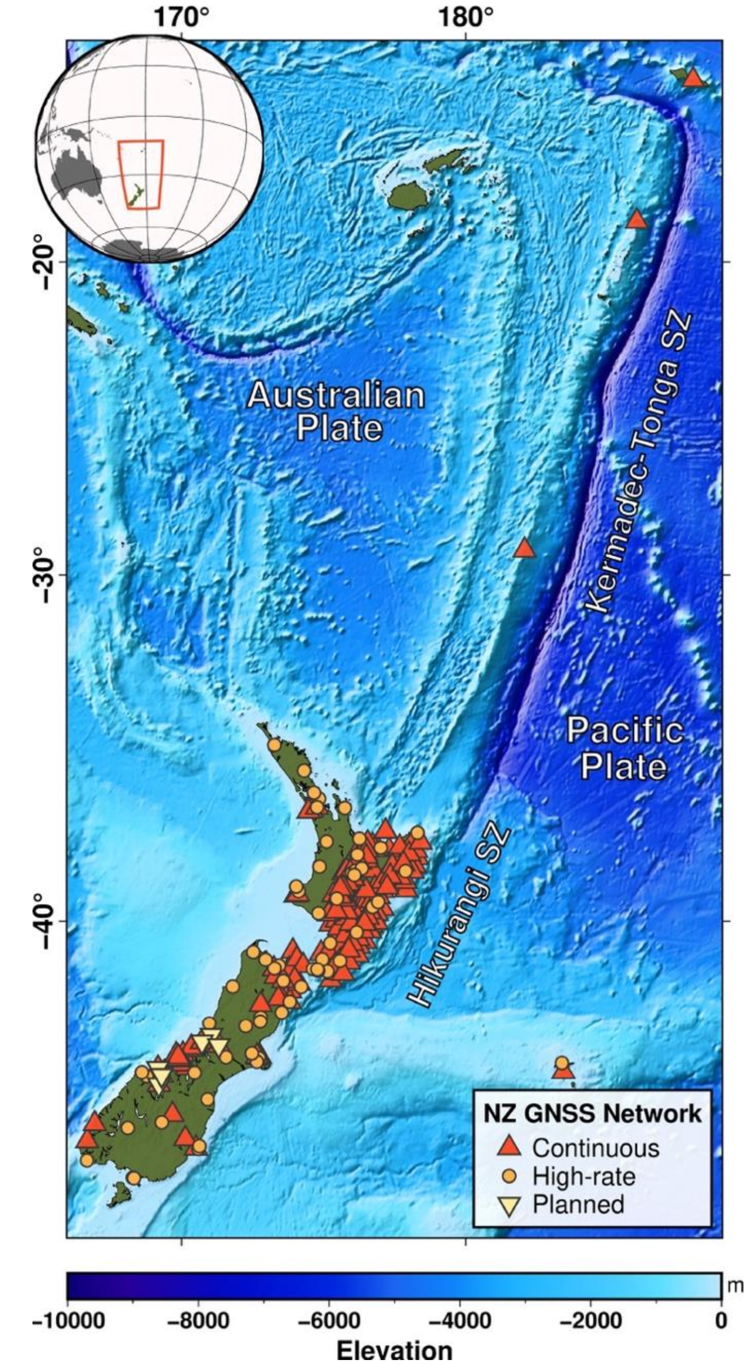

Figure 4.1. Tectonic Setting and Global Navigation Satellite System (GNSS) Network in New Zealand. Map highlights the Kermadec-Tonga and Hikurangi subduction zones. The color-shaded relief represents bathymetry, with labeled plate boundaries for the Australian and Pacific plates. The station locations are indicated by red triangles for continuous GNSS stations (30s data), orange circles for high-rate continuous GNSS stations (1s data), and pale yellow triangles for planned stations. The inset globe provides geographic context, showing the study area in red.

Given the potential for large subduction and crustal fault earthquakes, New Zealand is well equipped with a dense Global Navigation Satellite Systems (GNSS) network operated by GeoNet. A major multi-year public initiative led by GNS Science Te Pū Ao (now Earth Sciences New

Zealand), the RCET (Rapid Characterization of Earthquakes and Tsunami) program, is exploring new techniques for rapid estimation of earthquake rupture characteristics in New Zealand. The RCET program is testing real-time and rapid-response algorithms, such as those used in geodetic EEW systems (for a comprehensive overview of GNSS-based warning, see Crowell (2024)). Here, we specifically want to assess the performance of the Geodetic First Approximation of Size and Timing (G-FAST; Crowell et al., 2016, Crowell et al., 2018), for rapid source characterization of moderate-to-large earthquakes using synthetic ruptures and geodetic data. Geodetic algorithms are desirable because traditional approaches that rely on inertial instruments, such as seismometers and accelerometers, can be biased by magnitude saturation and baseline offsets, respectively (refer to review by Allen & Melgar, 2019). During an earthquake response, these factors could result in an inaccurate estimation of earthquake magnitude and an underestimation of seismic risks associated with the event. GNSS observations can address these issues but depend on the time required for slip to accumulate and for the signal to exceed the GNSS noise floor to detect an earthquake. For these reasons, we focus on evaluating large earthquakes (**M** ≥ 7) with geodetic data.

Due to the dearth of large earthquakes recorded with dense high-rate and real-time (HR) GNSS networks, the performance of geodetic EEW algorithms have been evaluated in previous studies using synthetic ruptures (e.g., Ruhl et al., 2017; Williamson et al., 2020; Nye et al., 2024). These approaches have relied on kinematic rupture models built using semi-stochastic simulations (e.g., LeVeque et al., 2016; Melgar et al., 2016), which represent "reduced-physics" approximations of the complexity of real large events. These models rely on statistical scaling laws and randomized slip generation techniques informed by historical finite-fault ruptures (e.g., Mai & Beroza, 2002; Melgar & Hayes, 2017). Kinematic parameterizations for rupture timing, velocity, and slip-rate are then applied using empirical relationships from dynamic rupture simulations (e.g., Graves & Pitarka, 2010, 2015). In this study, we instead explore an earthquake catalog of megathrust rupture scenarios generated using a physics-based earthquake cycle simulator (**Figure 4.2**).

Physics-based simulators like the Rate and State Earthquake Simulator (RSQSim; Richards-Dinger & Dieterich, 2012) provide an alternative to these semi-stochastic methods for generating synthetic earthquake ruptures. RSQSim models the earthquake cycle over tens to hundreds of thousands of years using simplified frictional laws. Slip initiates and propagates in response to the evolving stress state on the fault, together with its frictional properties and geometry, such that rupture extent, timing, and slip distributions emerge from physical processes and geometric complexity rather than imposed statistical assumptions. This approach enables the generation of complex events, such as joint subduction-crustal ruptures and multi-fault ruptures (Shaw et al., 2022; Delogkos et al., 2023), without imposing predefined rupture characteristics. These features suggest that RSQSim could serve as a valuable, and more physically consistent, alternative or complement to stochastic approaches—particularly in regions like New Zealand, where long-term deformation patterns are relatively well understood and geologic field data from paleoseismic records and slip rates are available. However, stochastic catalogs may remain preferable in contexts requiring a more comprehensive exploration of earthquake scenario variability (refer to **Figure 4.S1** showing the spatial distribution and magnitude range of events from both catalogs).

The potential use cases of multi-cycle physics-based simulators for probabilistic seismic and tsunami hazard assessment have been highlighted by recent proof-of-concept studies (Shaw et al., 2018; Rafiei et al., 2022; Hughes et al., 2023). In this study, we evaluate whether synthetic earthquakes generated by RSQSim are sufficiently realistic to calibrate early warning systems. Specifically, we address the following questions: *(i) Are RSQSim-generated ruptures realistic enough for EEW testing applications? (ii) How do the ruptures from an earthquake simulator compare to ones generated by stochastic kinematic modeling? And (iii) How well does G-FAST perform in estimating the moment magnitude of these synthetic earthquake scenarios?* To investigate these questions, we first compute synthetic displacement time series at the current continuous (HR) GNSS stations in New Zealand (GNS Science, 2019) for each rupture scenario, assuming those were all high-rate and real-time. We then compare the synthetic observations against known Peak Ground Displacement (PGD) estimates from published ground-motion models (GMMs) to validate our results. By applying this method, we can verify that these RSQSim ruptures mimic real earthquakes, at least to the extent that they produce realistic time-varying crustal deformation. We also perform the same PGD residual analysis using a second catalog of megathrust rupture scenarios, generated from semi-stochastic kinematic rupture models for the region of interest, to compare the results with those from an earthquake simulator. Finally, we ingest the synthetic GNSS data generated for RSQSim ruptures into an offline version of the G-FAST module in simulated real-time mode. G-FAST is an EEW module built for the ShakeAlert

EEW system in the U.S. (Given et al., 2018) that rapidly estimates magnitude, moment tensor, and slip distribution of earthquakes using GNSS observations. Ultimately, we aim to assess how accurately G-FAST estimates the magnitude of these synthetic megathrust events using the current operating GNSS network in New Zealand. This study will advance the inclusion of HR-GNSS in earthquake and local tsunami warning systems in New Zealand by identifying areas of strong ground shaking that can be affected by an earthquake in the Hikurangi subduction zone, one of the largest sources of earthquake and tsunami hazard in New Zealand.

4.2. Methods

In this section we detail the two approaches to rupture simulation, as well as the specifics of the waveform synthesis and EEW algorithm testing.

4.2.1. Finite-Rupture Models from an Earthquake Simulator

The first synthetic earthquake catalog of megathrust rupture scenarios was generated using RSQSim (Richards-Dinger & Dieterich, 2012), a quasi-static earthquake simulator that models long-term seismic cycles using rate-and-state friction laws (Dieterich, 1979). For reasons of computational efficiency, RSQSim simplifies the underlying fault physics more than modern multi-cycle earthquake simulators (Ozawa et al., 2022; Uphoff et al., 2023; Barbot, 2023; Zielke, 2023). Despite these simplifications, it can rapidly generate 10^5–10^6-year synthetic catalogs of earthquakes with slip distributions and magnitude–frequency characteristics that are realistic to first order.

We use synthetic ruptures from one of three synthetic earthquake catalogs generated by Hughes et al. (2025) for the Hikurangi-Kermadec subduction interface. This 30,000-year catalog includes 470 events ranging from **M**8.0 to **M**9.4 along the Hikurangi subduction zone (**Figure 4.2**). It uses the same subduction interface geometry as the New Zealand National Seismic Hazard Model 2022 Revision (NZSHM22; Gerstenberger et al., 2023), which was created by merging Slab 2.0 (Hayes, 2018) for the Kermadec portion with the Hikurangi interface geometry of Williams et al. (2013). Stressing rates and fault rake were derived from backslip loading, treating the geodetic slip-deficit rate distribution as representative of long-term slip in earthquakes (following Van Dissen et al., 2024). Following NZSHM22, present-day creeping sections were assumed not to host earthquake slip. We chose to use the "trench-locked" slip-deficit-rate distribution (Hughes et al., 2025), mainly because we wished to include ruptures that slip to the trench but also because that was the preferred slip model of NZSHM22. In terms of frictional parameters, the rate-and-state *a* and *b* values were set at 0.001 and 0.004 respectively, to give average stress drops that match the magnitude-area scaling preferred by NZSHM22 (Stirling et al., 2024). The remaining frictional parameters used in RSQSim are provided in **Table 4.S1** of the Supplementary Information and are discussed in detail by Hughes et al. (2025).

The earthquake simulator ruptures are "quasi-dynamic" because they do not resolve the full time history of slip at each subfault. Instead, it uses approximate rupture propagation governed by rate-and-state friction laws. In particular, slip-rate histories and rise times generated by RSQSim, required to describe the temporal evolution and duration of local slip on the fault, are not useful for our purposes—due to an assumption of constant rupture velocity by RSQSim. However, users can assign these parameters externally through kinematic assumptions when synthesizing waveforms. These are necessary to fully describe the rupture kinematics, and without them, it is not possible to generate waveforms directly from RSQSim ruptures. Following what is commonly done in kinematic rupture modeling, we can make some dynamically reasonable assumptions to add these parameters. We follow Graves & Pitarka (2010, 2015) to define rise times, where rise time scales with the square root of slip plus a magnitude scaling constant. As a result, patches with larger slip have longer rise times and larger ruptures have, on average, longer rise times as well. Additionally, each rise time receives a small stochastic perturbation so that similar amounts of slip have slightly different rise time values. For the slip-rate history, we assume the Dreger slip-rate function. Mena et al. (2010) and Melgar et al. (2016) showed that this function has the appropriate spectral decay, compared to other common assumptions such as the triangle or raised cosine, and is consistent with rupture dynamics findings. The full details of this implementation of rupture kinematics and how they have been modified from Graves & Pitarka (2010, 2015) for mega-thrust earthquakes is laid out in Melgar et al. (2016). Finally, with the full time history of each RSQSim rupture defined, we proceed to generate synthetic HR-GNSS data with FakeQuakes—which supports both rupture and waveform generation (described in the following sections), using a Green's function approach and velocity model from LITHO1.0 (Pasyanos et al., 2014).

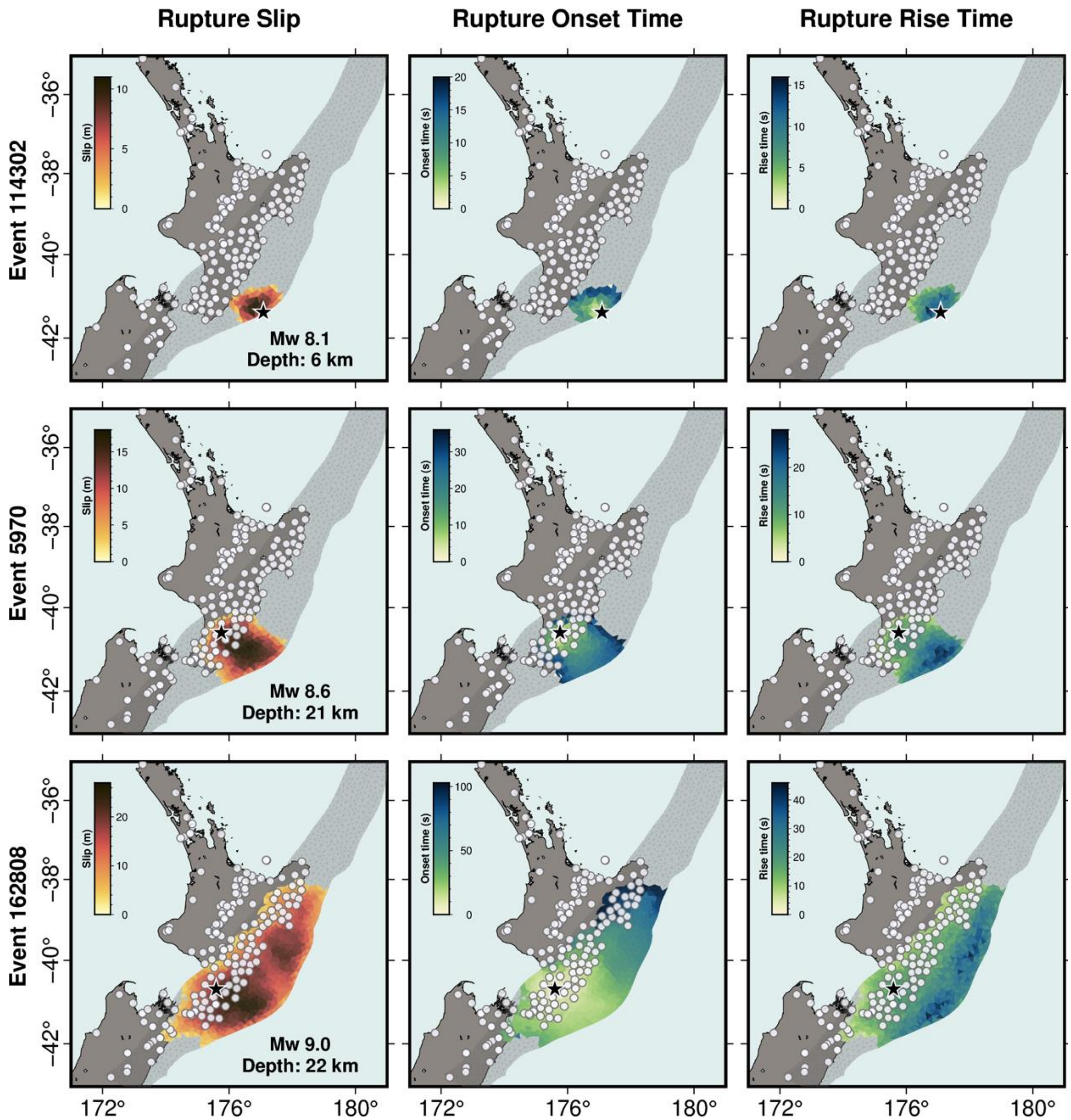

Figure 4.2. Three rupture scenarios generated by the RSQSim earthquake simulator. Rows represent individual events, and columns show: (1) rupture slip distribution, (2) rupture onset time, and (3) rise time for subfaults with slip greater than 10% of the maximum slip. White circles indicate the locations of GNSS stations, and the black star represents the event epicenter.

4.2.2. Finite-Rupture Models from Semi-Stochastic Kinematic Modeling

The second synthetic catalog of megathrust rupture scenarios, used for comparison with RSQSim, was generated using FakeQuakes, part of the MudPy suite for semi-stochastic earthquake source modeling described by Melgar et al. (2016) and summarized herein. Statistical parameters in FakeQuakes have been calibrated to match those measured in slip distributions of global events (Melgar & Hayes, 2017) and a systematic comparison against large earthquakes has been carried out to validate that the resulting slip distributions represent what is seen in megathrust ruptures (Small & Melgar, 2023). The final catalog consists of 731 synthetic events with target magnitudes ranging from **M**7.8 to **M**9.4 along the Kermadec-Tonga subduction zone. To focus on the Hikurangi subduction region, the catalog was filtered to retain 381 events in which slip occurs at or south of 37.5°S.

To generate these rupture scenarios, we first defined the fault geometry as before, but with a coarser spatial resolution, and used the same 1-D velocity model from LITHO1.0, with a maximum depth of 25 km and a maximum slip of 50 m. The fault plane was discretized into a 3D mesh of subfaults, each assigned a displacement (slip vector) along the strike and dip directions. Stochastic rupture dimensions (length and width) were determined using the probabilistic scaling laws of Blaser et al. (2010), with a randomly selected subfault as the hypocenter. Slip was distributed across the subfaults using a von Kármán correlation function, following the approach of Mai & Beroza (2002). This ensures consistency with the fault dimensions prescribed by the scaling laws to match the target magnitude. A Karhunen-Loève expansion (LeVeque et al., 2016) approach was then applied to model the spatial pattern of slip vectors, as it more accurately captures the complexity of observed earthquake slip distributions. From the resulting slip distribution, kinematic rupture parameters (i.e., rupture speed, rise time, and slip rate) were derived following the same methods used for the RSQSim ruptures in Section 2.1—recall that this follows from Graves & Pitarka (2010, 2015) and is calibrated to observations noted in Melgar et al. (2017). Finally, synthetic HR-GNSS data were generated with FakeQuakes, in a manner consistent with the RSQSim ruptures, using the same Green's function approach and velocity model.

4.2.3. Generating Synthetic HR-GNSS Data

The GeoNet GNSS network provides dense station coverage across the North Island and sparser coverage in the South Island (GNS Science, 2019). In this study, to evaluate the performance of G-FAST in New Zealand, we are using 239 existing continuous sites (including 56 high-rate stations delivering data in real-time), with an additional 6 sites planned for the South Island (**Figure 4.1**). Displacement data were synthesized for all stations using FakeQuakes. First, we calculated Green's functions using the method of Zhu & Rivera (2002) to obtain an impulse response for each station-subfault pair, thus relating ground motion at a site to slip on each subfault. We then convolved the Green's functions at each site with the slip-rate function of each sub-fault to synthesize waveforms at a sampling rate of 1Hz (**Figure 4.3**). Finally, we obtained GNSS time series that represent ground motion at a specific site for all rupture scenarios in our catalog. To simulate realistic observations, random noise that simulates the power spectrum of real-time GNSS position noise was added to the synthetic GNSS displacement time series following Melgar et al. (2020)—this allows us to mimic instrumental errors and environmental variability. We used four different noise levels defined by Melgar et al. (2020), ranging from the 1st percentile (representing very low noise) to the 90th percentile (representing very high noise).

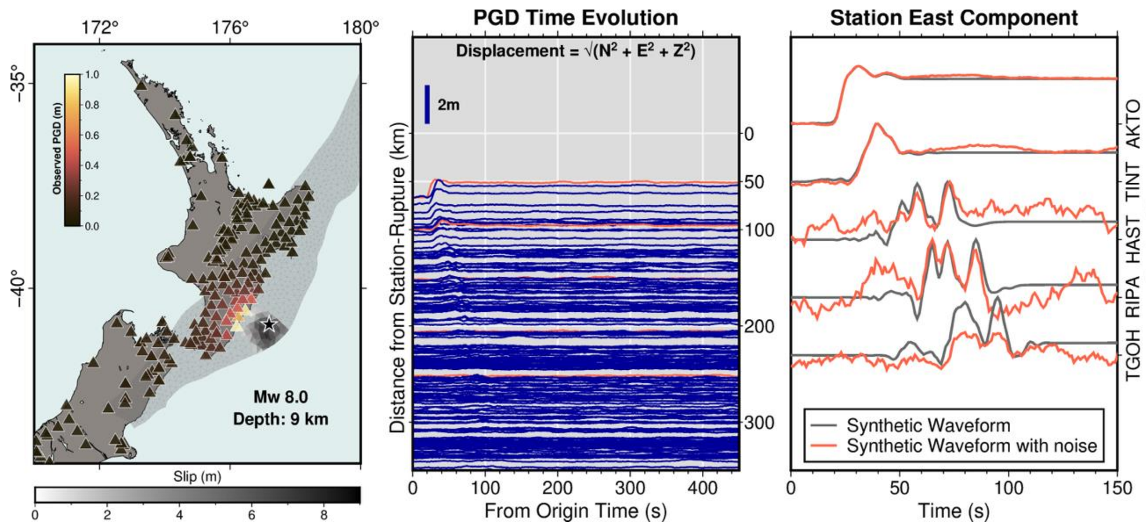

Figure 4.3. Synthetic high-rate Global Navigation Satellite System (HR-GNSS) data and waveforms. The left panel shows the observed peak ground displacement (PGD) values for a randomly selected rupture scenario, with black star indicating epicenter location and slip distributions shown in grayscale for reference. The center panel illustrates the time evolution of PGD for each station up to 350 km from the rupture; red lines indicate selected stations whose waveforms are shown in the right panel. The right panel presents synthetic waveforms with added noise examples.

4.2.4. Data Validation

The GNSS Peak Ground Displacement (PGD) value is obtained from the root sum square of the three components in a GNSS time series that recorded the highest ground motion (**Figure 4.3**). This is a useful metric for estimating the size of an earthquake. In this study, we use the relation between PGD and moment magnitude to calculate the predicted PGD value at each GNSS station for every rupture scenario (Eq. (1)). The GNSS Ground Motion Model (GMM) form is based on geodetic data and given by the following scaling law from Crowell et al. (2013):

$$log_{10}\,(PGD) = \mathrm{A} + \mathrm{B}\,\mathbf{M} + \mathrm{C}\,\mathbf{M}\,log_{10}(R)\,, \qquad \text{Eq. (1)}$$

where A, B, and C are the regression coefficients, **M** is the moment magnitude, and *R* is the distance between the GNSS station and the earthquake source (refer to **Table 4.S2** of the Supplementary Information for coefficient values). To validate the GNSS waveforms in this study, we used a modified version of the GNSS GMM described above, incorporating the most recent regression coefficients and replacing the hypocentral distance with the generalized mean rupture distance (R_p; Thompson & Baltay, 2018), as implemented in Goldberg et al. (2021). R_p is the distance from the station to the entire rupture plane weighted by the slip (*w*) on each sub-fault (*n*) and raised to the power of the mean (*p*), express as follow:

$$R_p = \left(\sum_{i=0}^{n} w_i\, R_i^p\right)^{1/p}, \qquad \text{Eq. (2)}$$

with a value of p = -2.3, suitable for a wide range of rupture styles, as demonstrated in Goldberg et al. (2021). The advantage of using R_p as a distance metric is that it allows for a more realistic treatment of a finite source as opposed to assuming a large rupture is a point source (e.g. as with the hypocenter distance). The modified GNSS GMM model is calibrated using observed PGD measurements from 33 earthquakes world-wide of magnitude **M** 6-9, including the 2016 Kaikōura earthquake in New Zealand (for more details refer to Goldberg et al., 2021).

We calculated the residuals between the observed and predicted PGD values for each station and rupture using Eq. (3). The observed values represent PGD from simulations, while the predicted values are derived from the modified GNSS GMM. To account for limitations in GMMs as we move away from the source, we filtered out PGD values for stations located more than 1000 km from the rupture. The residuals quantify how much the observed PGD deviates from the expected PGD for a given rupture scenario. This approach allows us to validate our results and assess whether RSQSim ruptures adequately simulate the behavior of real earthquakes.

$$\ln\left(\frac{PGD\ observed}{PGD\ predicted}\right), \qquad \text{Eq. (3)}$$

4.2.5. Testing EEW and Rapid Earthquake Characterization

EEW systems are designed to provide rapid alerts of ground shaking by detecting initial seismic waves. Depending on the location and magnitude of the event, EEW systems can reduce the impact of earthquake hazards by alerting nearby communities, though warning times decrease as proximity to the source increases. The effectiveness of such systems depends on the network (station coverage), processing center (real-time data processing) and infrastructure (e.g., communications component to deliver alerts). Ultimately, the success of these systems is determined by how end-users receive, understand, and act on those alerts. Traditional EEW systems rely primarily on seismometers to estimate earthquake location and magnitude. In real-time operation, G-FAST is triggered by seismic data, which provides an initial hypocenter, origin time, and magnitude of the event within seconds of seismic wave arrivals. G-FAST consists of three main modules: a first module that obtains the PGD to estimate a point-source magnitude, and a second module that computes a geodetic centroid moment tensor (gCMT) solution (Crowell et al., 2012) using the GNSS static offsets to determine fault orientations (strike and dip), location, and magnitude of the event (Crowell et al., 2013; Melgar, Crowell, et al., 2015; Crowell et al., 2018). From the gCMT nodal planes solution, a third module activates to invert for slip and produce a finite-fault model. For additional details about the operational version of G-FAST that is used within ShakeAlert, see Murray et al. (2023).

In this study, we use a modified offline version of G-FAST implemented in Python to process synthetic GNSS waveforms generated by FakeQuakes for the RSQSim ruptures, without relying on a seismic trigger. The production version of G-FAST was originally written in Python and later converted to C/C++, which is faster and more efficient for computing solutions. The hypocenter and magnitude from RSQSim rupture scenarios are used as the initial solution derived from seismic data. G-FAST begins with the first module to obtain PGD magnitude, as described in the previous section from Crowell et al. (2013), and applies exponential weighting as a function of epicentral distance to prioritize stations closer to the source, using a minimum of four stations and a 3 km/s travel-time mask to exclude those that have not yet experienced strong ground shaking (Crowell et al., 2016). Subsequently, G-FAST estimates GNSS static offsets and initiates the second gCMT module. This module performs a grid search to find the optimal centroid location and invert for fault orientation. Lastly, G-FAST uses the nodal plane orientations from the gCMT solution to estimate finite-fault slip. The system runs for 480 s and produces a solution every second. We then evaluate its performance in reproducing the magnitudes of rupture scenarios generated by RSQSim with the current operating GNSS network in New Zealand. We note that while G-FAST results could ultimately feed into EEW systems, this study does not test forecasting or alerting components. Instead, we focus on evaluating rapid source characterization using GNSS data. This approach aims to improve our understanding of earthquake processes in this region and, in combination with other complementary seismic EEW and rapid analysis tools (e.g. FinDer; Andrews et al., 2024), to better identify areas of strong ground shaking during future seismic events.

4.3. Results

Following is a description of the results with respect to validation for the GNSS waveforms and EEW performance.

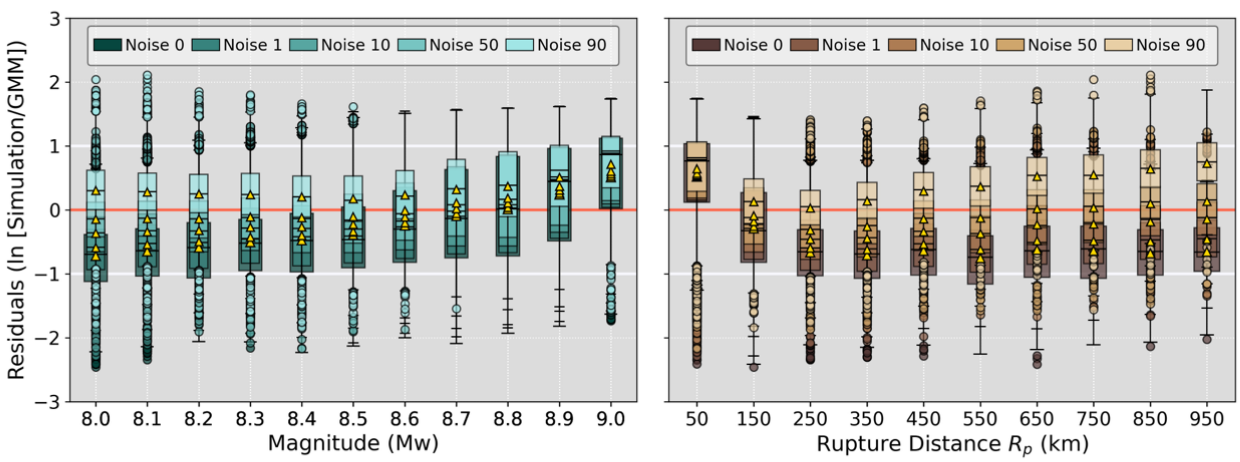

Figure 4.4. Boxplots of peak ground displacement (PGD) residuals for ruptures from the RSQSim catalog. The left panel shows residuals against magnitude (teal), while the right panel shows residuals against distance (brown). The red line represents zero, indicating the target residual value. Gold triangles denote the mean, and the horizontal black line represents the median per bin. The color shading corresponds to different Global Navigation Satellite System (GNSS) noise levels, ranging from the ideal scenario with no noise to the 90th percentile.

4.3.1. Synthetic HR-GNSS Data Validation Using Catalog of Megathrust Ruptures Scenarios

To validate our simulated data from synthetic ruptures, we performed a residuals analysis as defined in Eq. (3). In this context, residuals indicate the discrepancies between the simulated (observed) PGD values and those predicted by the modified GNSS GMM. For example, a positive residual means that the observed PGD value is higher than expected, or that the GNSS GMM is underpredicting the PGD value, a negative residual signifies the opposite behavior. Ideally, we aim for residuals to behave such that, on average, they trend towards zero, which means that the observed and predicted values are in agreement, without biases correlated to event magnitudes or source-station distances. To investigate any biases in our simulations for accurately predicting ground motion, we plotted residuals against magnitude (teal) and rupture distance (brown) in **Figure 4.4**. Poor performance is expected at larger distances, where the PGD value tends to zero, and at lower magnitudes, where the signal falls below the noise floor.

For this study, the synthetic HR-GNSS waveforms data were generated for an ideal scenario where all stations are functional and recording high-rate data continuously and in real-time. Given that the GMMs are derived from noisy data, we added noise to better approximate real-world conditions. In **Figure 4.4**, the boxplots represent the same dataset (i.e., PGD residuals using RSQSim rupture scenarios) but with increased noise levels. For the simulations, PGD values with no noise are lower than expected closer to -1 natural log unit, as shown in **Figure 4.4**. PGD values with no noise are critically underestimated at distances greater than ~150 km from the source to the station and for low to mid **M**8 events. Ultimately, we selected the 50th percentile over the 90th percentile, as the latter tends to overcorrect with positive residuals. The 50th percentile resulted in residuals closer to zero, aligning more closely with the predicted PGD values from the modified GNSS GMM (**Figure 4.4**).

PGD results are shown for a set of RSQSim ruptures in **Figure 4.5** (same ruptures shown in **Figure 4.2**). The first row in **Figure 4.5** compares simulated PGD values with noise (triangles indicating station locations) to predicted PGD values from the GMP (surface interpolation) as ground truth. We expect the colors to match, indicating that the simulated PGD values closely approximate the predicted PGD values. To better visualize the pattern, we normalized the PGD values. The colormap changes follow a similar pattern, highlighting the consistency between the simulated and predicted PGD values. As anticipated, the highest PGD values are observed at stations near the earthquake source, primarily due to their proximity to the rupture. The second row in **Figure 4.5** compares the residuals of simulated PGD values with noise (triangles indicating station locations) to simulated PGD values without noise (surface interpolation) highlighting spatially how the added noise adjusts lower-than-expected PGD values. For larger ruptures, the addition of noise has minimal impact. The noise added primarily helps adjust values that are lower than expected, as larger PGD values already exceed the noise threshold.

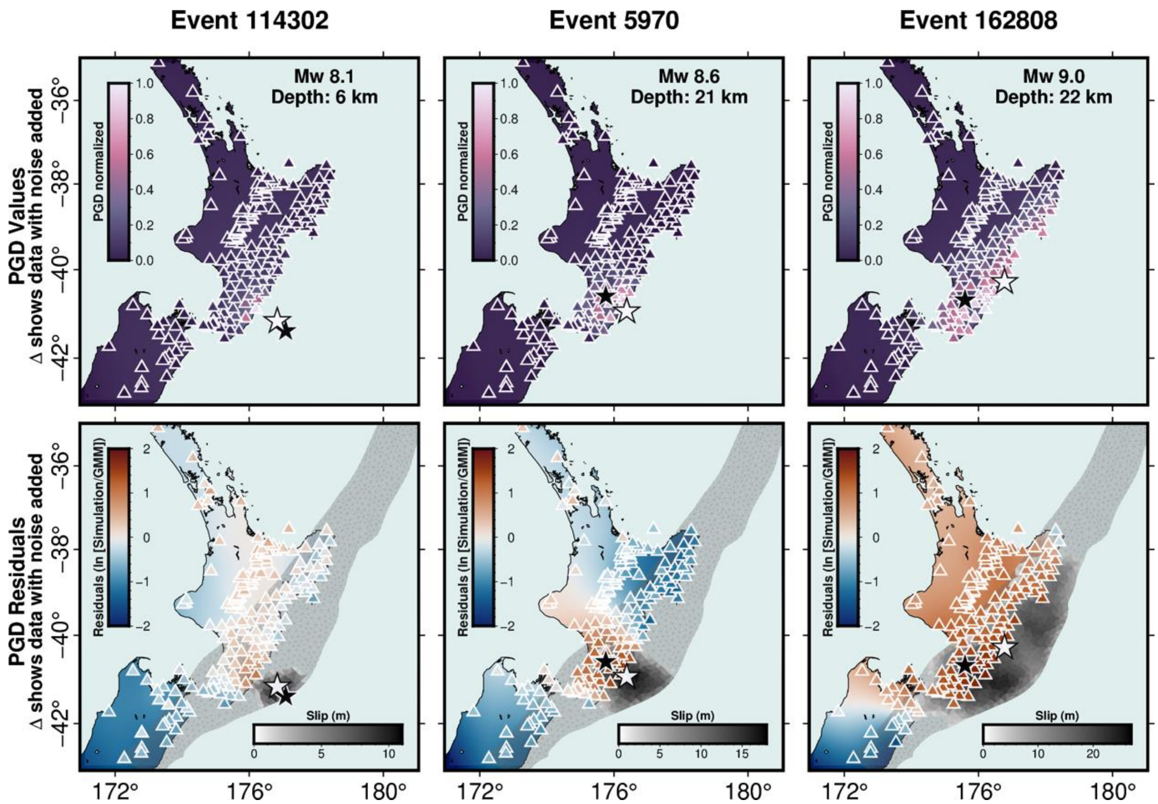

Figure 4.5. Spatial visualization of predicted and observed peak ground displacement (PGD) values and residuals for selected events. Each column represents a separate rupture scenario, with the black star indicating the epicenter location and the white star indicating the centroid location. The first row shows predicted PGD (surface grid) compared with observed PGD (color-filled triangles); labels indicate magnitude and depth of the event; vertical colormap indicates normalized PGD value. The second row shows PGD residuals without noise (surface grid) and PGD residuals with noise (color-filled triangles); vertical colormap indicates PGD residual and horizontal colormap indicates amount of slip for reference.

In addition to generating synthetic waveforms, FakeQuakes module can also generate ruptures scenarios using a kinematic modeling approach, which is not necessarily physics-informed but is more computationally efficient compared to an earthquake simulator. Although FakeQuakes can produce a catalog with as many events as the user specifies, RSQSim generates an earthquake cycle that is arguably more representative of the long-term seismic behavior and fault interactions in a region. Therefore, we expect that ruptures from RSQSim will perform better than those from FakeQuakes. We created a second synthetic catalog using FakeQuakes, with events in the M7.8 to M9.4 range targeted at the Hikurangi region and generated synthetic waveforms to obtain PGD values. We then compared PGD residuals between RSQSim and FakeQuakes ruptures scenarios as shown in **Figure 4.6**. RSQSim ruptures (boxplots with solid fill color in **Figure 4.6**) generally yield residuals closer to zero than FakeQuakes ruptures (boxplots with solid fill and hatch in **Figure 4.6**), indicating better agreement with the expected PGD values from the modified GNSS GMM based on observed earthquakes. While both approaches rely on user-defined parameters, these results indicate that the RSQSim rupture scenarios more closely represent real earthquake behavior, as supported by their consistency with expected ground motions.

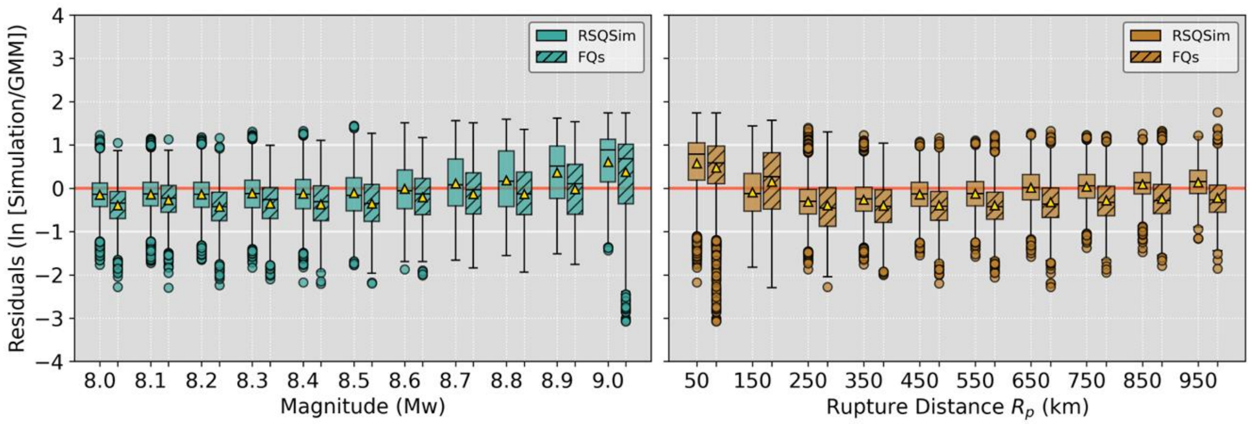

Figure 4.6. Boxplots of peak ground displacement (PGD) residuals for RSQSim ruptures (filled boxplots) and FakeQuakes ruptures (filled hatch boxplots). The left panel shows residuals against magnitude (teal), while the right panel shows residuals against distance (brown). The red line represents zero, indicating the target residual value. Gold triangles denote the mean, and the horizontal black line represents the median per bin.

4.3.2. Performance of EEW Magnitude Estimates

We conducted a final test using synthetic GNSS waveforms generated by RSQSim to evaluate G-FAST's ability to estimate event magnitudes. In **Figure 4.7a**, we compare the PGD and gCMT magnitudes produced by G-FAST to the target magnitude (i.e., the synthetic moment magnitude) of each RSQSim event. Successful performance by G-FAST would yield magnitudes within the uncertainty bounds of ±0.3 magnitude units of the true magnitude. This threshold reflects the expected uncertainty of PGD-based magnitude estimates, as defined by Crowell et al. (2016). Estimates within this range provide reliable initial earthquake characterization, supporting downstream modeling such as tsunami forecasting (Williamson et al., 2020). To assess G-FAST's performance, we categorize the results into three groups as shown in **Figure 4.7b**: (1) optimal performance, where estimates fall within ±0.3 magnitude units (low errors); (2) moderate performance, where estimates fall between ±0.3 and ±0.5 magnitude units (moderate errors); and (3) poor performance, where errors exceed ±0.5 magnitude units (high errors). G-FAST correctly estimated magnitudes with optimal performance ~90% of the cases for PGD magnitude and ~81% for gCMT magnitude. The gCMT results appear more stable than the PGD magnitudes when following the linear trend (**Figure 4.7b**); however, they exhibit the largest errors, with 16 out of 17 events categorized as poor performance. In contrast, while the PGD results tend to underestimate the target magnitude, they are overall more accurate than the gCMT results, with lower errors.

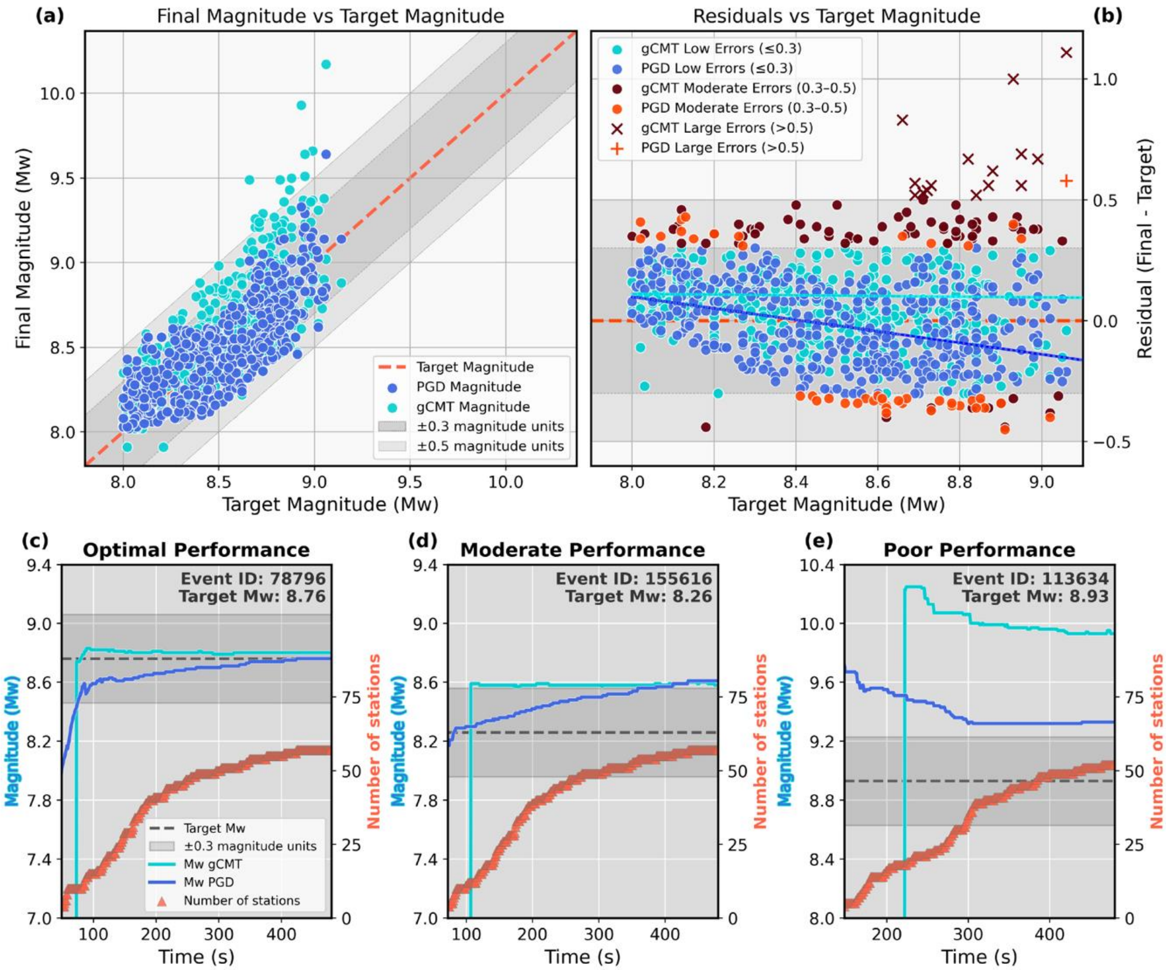

Figure 4.7. Comparison of G-FAST final magnitudes derived from peak ground displacement (PGD) and geodetic centroid moment tensor (gCMT) with target magnitudes for all rupture scenarios from RSQSim. Panel (a) shows PGD-derived magnitudes (blue) and gCMT-derived magnitudes (cyan) plotted against target magnitudes, with the red dashed line representing the true or target magnitude. Panel (b) shows magnitude residuals (Final – Target) for both PGD and gCMT modules, where markers highlight moderate errors (filled circles in warm colors) and large errors (symbols in warm colors). The red dashed line represents the zero residual baseline. In both panels, gray shaded regions indicate ±0.3 and ±0.5 magnitude deviations. Panels (c–e) illustrate examples of simulated real-time magnitude evolution for three events demonstrating optimal (c), moderate (d), and poor (e) performance based on magnitude residuals. Each panel shows the time evolution of PGD (blue) and gCMT (cyan) magnitudes compared to the target magnitude (gray dashed line), along with the number of GNSS stations contributing to the solution (orangered). The gray shaded area represents ±0.3 magnitude deviations from the target.

Events categorized as having poor performance were primarily associated with deeper hypocenters (≥30 km) located north of 36°S latitude (**Figure 4.8**). In most of these cases, the discrepancy between the hypocenter and centroid of the original rupture scenario was also large

(**Figure 4.9** shows discrepancies for PGD estimates and **Figure 4.S2** in the Supplementary Information for the gCMT estimates). These ruptures propagated south, with slip concentrated south of the hypocenter, extending into the Hikurangi subduction zone. The exception is an event east of the North Island, near the edge of the Hikurangi margin towards the trench, which was a shallow event (~5 km depth). For events categorized as moderate performance, we note that if an event occurs near the station network with good coverage but at a depth of ~20 km or more for PGD results and ~10 km or more for gCMT results, G-FAST may not perform optimally in most cases. Meanwhile, the gCMT results are more scattered, particularly struggling at shallower depths and for sources located farther offshore.

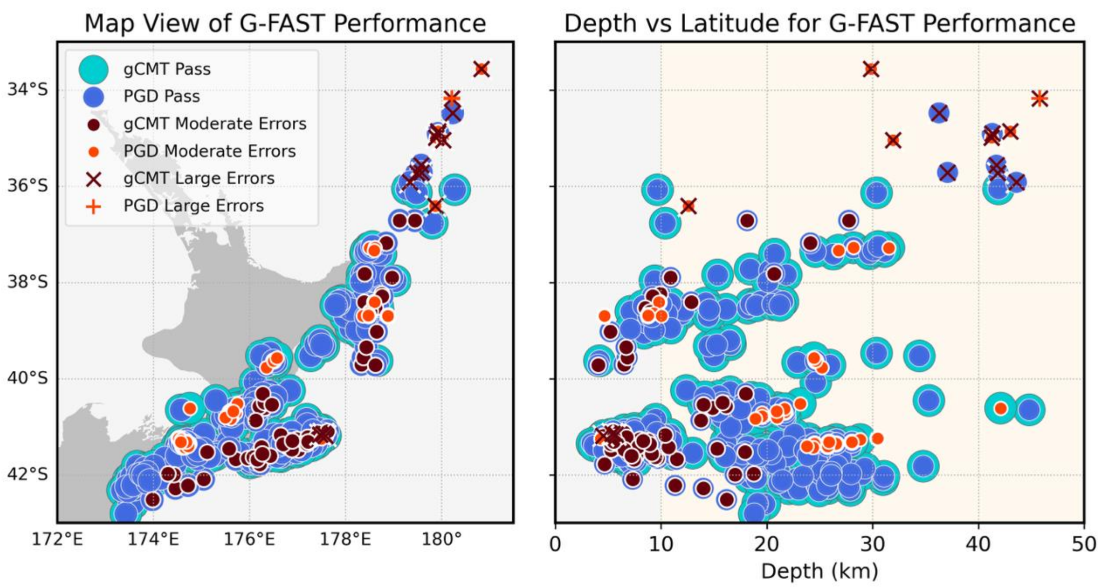

Figure 4.8. Spatial and depth distribution of G-FAST performance for all rupture scenarios from RSQSim. The left panel shows a map view of G-FAST performance. Peak ground displacement (PGD) and geodetic centroid moment tensor (gCMT) solutions are colored by accuracy: cool colors indicate solutions within ±0.3 magnitude units of the reference value, while warm colors denote moderate (filled circles) and large (other symbols) discrepancies in magnitude estimation. The right panel shows depth vs. latitude distribution of G-FAST performance, illustrating the relationship between event depth and estimation accuracy. The same color scheme is used to distinguish passing solutions from those with moderate and large errors.

An extraordinary case is a full rupture event in the Kermadec-Tonga subduction system, where G-FAST is unable to produce a solution (refer to **Figure 4.S3** in the Supplementary Information). This occurs because the stations are too far from the epicenter to compute a reliable solution. Although this event does not necessarily occur in the Hikurangi subduction region, it shows substantial slip in this area, which could potentially cause strong ground shaking and/or pose a tsunami threat.

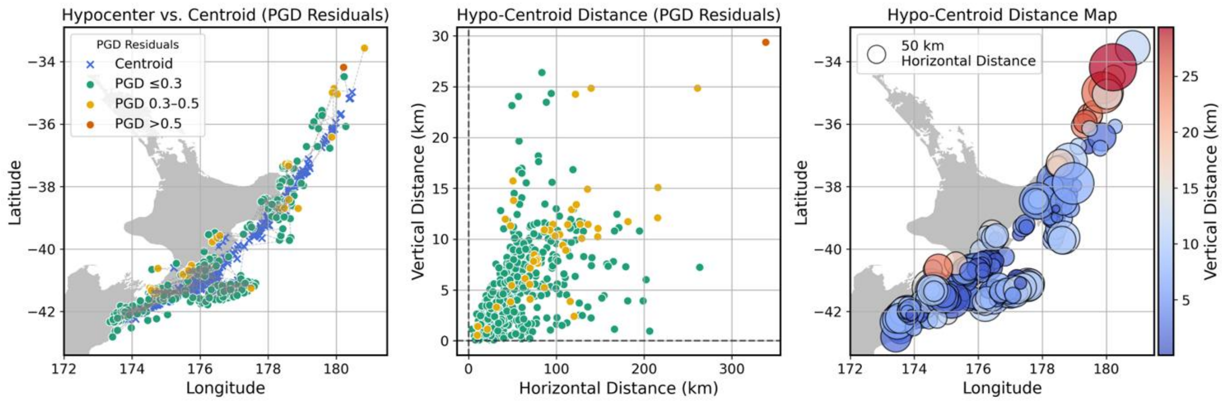

Figure 4.9. Comparison of hypocenter and centroid locations with magnitude residual (Final – Target) categories for peak ground displacement (PGD) solutions. The left panel shows hypocenter locations (circles) and centroid locations (blue crosses) for PGD residuals. Hypocenter locations are color-coded by error magnitude: green for low errors (≤0.3), yellow for moderate errors (0.3–0.5), and red for large errors (>0.5), corresponding to varying residual magnitudes. The middle panel presents hypocenter vs. centroid locations for PGD residuals, following the same residual categorization. The right panel displays a hypocenter map, where marker size and color represent the horizontal and vertical distances, respectively, between the hypocenter and centroid.

4.4. Discussion

This study provides a framework to evaluate G-FAST performance using simulations rather than real earthquakes and geodetic observations. As Earth Sciences New Zealand moves toward more timely and accurate earthquake characterization and tsunami forecasting, these simulations provide valuable insights into system behavior across a range of earthquake magnitudes and locations. Studies similar to the one presented here can help identify potential gaps in the current GNSS events that are more challenging to characterize, ultimately contributing to scientific strategies to improve future decision-making during an earthquake response.

First, we analyzed a catalog of megathrust rupture scenarios generated using the RSQSim earthquake cycle simulator, which demonstrated better performance than semi-stochastic kinematic rupture models (**Figure 4.6**). Before ingesting simulated GNSS waveforms from these rupture scenarios into G-FAST, we validated the synthetic displacement data against a modified GNSS-based GMM (Crowell et al., 2013; Goldberg et al., 2021) derived from earthquake data. This step ensured that the simulated data produced ground motions comparable to those observed from real earthquakes, since not every rupture results in 30 meters of displacement. To better reflect real-world conditions, we added noise to the synthetic GNSS waveforms, accounting for the inherently noisy geodetic data and improving the robustness of our results (**Figures 4.3** and **4.4**). This validation was essential, and further refinements could be made by incorporating real

GNSS noise characteristics from the region into the generation of synthetic waveforms. However, for this exercise, the residuals remained within an acceptable range, supporting the reliability of our synthetic displacement data (**Figures 4.5** and **4.6**).

The optimal performance of G-FAST is defined here by its ability to estimate the event magnitudes within ±0.3 units of the target magnitude (**Figure 4.7**), excluding one exceptional case involving a full-margin rupture along the Kermadec–Tonga subduction zone, where the hypocenter was too far from stations for G-FAST to resolve (**Figure 4.S3**). Under this criterion, PGD estimation proves to be a simple and reliable method, achieving this level of accuracy in 90% of RSQSim rupture scenarios. This is particularly notable when compared to Williamson et al. (2020), who used a larger set of rupture scenarios but with a stochastic modeling approach, achieving 82% accuracy in magnitude estimation. However, the gCMT module's grid search could be improved, as it meets this threshold in only 81% of cases and often fails to capture the true size of the event or identify the correct fault plane when using geodetic data alone. Factors contributing to moderate and poor G-FAST magnitude estimate include the predominantly unilateral behavior of ruptures in the catalog, as discussed by Williamson et al. (2020) and observed in this study (**Figure 4.S2**). The imposed thrust component, a characteristic of megathrust earthquakes, is prior knowledge that G-FAST does not inherently account for and must instead resolve independently. If the rupture directivity propagates in one direction, especially away from stations, it could create asymmetry in the observed PGD values, where stations at similar distances from the source record different PGD values. This variability could make it more challenging for a geodetic EEW system to resolve the rupture, as seismic energy decays at larger distances, reducing the signal strength above the GNSS noise level needed to detect an event or capture full slip distributions. Additionally, the complexity of the rupture (e.g., multiple faults and asperities) further complicates event characterization. Other contributing factors include the fact that many ruptures are one-sided, as the subduction interface is offshore, and the high density of stations is located inland on the overriding plate. These limitations highlight the need for a well-distributed and dense station network to improve event characterization. While this is not a major concern in the North Island—except at greater depths or farther offshore, it remains a constant challenge in subduction zone settings and other regions of New Zealand such as the Alpine Fault where the station coverage is more sparce.

State-of-the-art tools using seismic data can provide accurate and timely information about large earthquake magnitude and can encompass limitations of GNSS-HR techniques such as the ones presented in this paper. But GNSS-HR is still an invaluable and unique tool to rapidly assess the slip distributions of large events. This is provided by G-FAST and should be examined more closely to validate slip in relation to the gCMT module and slip inversion. Accurately determining magnitude is important but so is generating reliable slip models to gain deeper insight into rupture processes and better inform tsunami warnings. Improving slip models would enhance our ability to interpret rupture processes in real-time applications and better approximate ground motions and tsunami hazards, which depend on the concentration of slip and the earthquake source. However, both magnitude and slip estimates are sensitive to the initial earthquake location, which remains fixed in this study but can introduce errors in real-time applications where depth is uncertain. Building on this work, a forthcoming study (Caballero et al., *in preparation*) evaluates the impact of depth uncertainty and grid search on the stability and accuracy of G-FAST solutions. The framework presented here could also be extended to adapt the tsunami early warning approach used in Williamson et al. (2020) to the Hikurangi subduction zone. Their study focused on near-field tsunami forecasting in Cascadia using synthetic kinematic ruptures, and a similar methodology could be tailored for Hikurangi with RSQSim-generated ruptures to assess tsunami impact and complement offshore data (e.g., DART and tide gauge sensors). From this approach, coastal amplitude thresholds for different tsunami sizes could be explored for integration into tsunami forecasting systems. This has the potential to enhance the responsiveness of tsunami alerts for coastal communities within the critical first few minutes after an earthquake, bridging the gap between earthquake detection and tsunami arrival, as demonstrated by Williamson et al. (2020).

Having focused on megathrust events, our framework could also be applied to other fault types. Crustal faults, for example, pose significant geological hazards—including landslides and strong ground shaking, depending on the timing and location of the earthquake. In the future, it would be valuable to explore more complex scenarios, such as the Alpine and Wellington faults, which both exhibit dextral motion with a dip component. The Alpine Fault, given its more remote location and potential to host **M**7-8 earthquakes (Orchiston et al., 2018; Howarth et al., 2021), may be better suited for rapid characterization of the source. In contrast, the Wellington Fault, located near densely populated areas, presents greater challenges for rapid response due to short source-to-site distances, but offers an opportunity to test earthquake response strategies and identify zones of intense ground motion. Simulations of even more complex rupture scenarios, such as the multi-segment 2016 **M**7.8 Kaikōura rupture that extended offshore (Duputel & Rivera, 2017; Hamling, 2020), could also provide further insights, particularly when compared against real earthquake observations from GNSS records.

4.5. Conclusions

Are the ruptures generated by RSQSim realistic? Yes, to some extent. RSQSim ruptures mimic real earthquakes, validated using PGD as a metric to simulate ground motion and compare it to expected values from global earthquake statistics. *How do these ruptures compare to those produced by kinematic modeling*? RSQSim ruptures outperform kinematic modeling approach, which lack the (simple) physics-based constraints provided by earthquake simulators. *How well does G-FAST perform in estimating the moment magnitude of these synthetic earthquake scenarios?* Overall, PGD magnitude estimation demonstrates high reliability, outperforming gCMT-based estimates by providing accurate magnitudes in most rupture scenarios—assuming ideal conditions where all stations are operational. Further evaluation of the gCMT grid search and spatial slip distribution is needed for a comprehensive assessment of G-FAST's performance and its implementation in New Zealand. In brief, rupture scenarios generated by earthquake simulators are a valuable tool for assessing seismic and tsunami hazards associated with potential earthquakes in regions of interest (Crowell et al., 2016; Williamson et al., 2020; Hughes et al., 2025). They also provide a testing ground for implementing rapid earthquake characterization algorithms within regional seismic networks for rapid response and early warning purposes, particularly for large earthquakes, where prior knowledge is limited due to long recurrence intervals and/or data availability. In this study, we leveraged the dense GNSS network in North Island of New Zealand to showcase our approach by generating synthetic data for rupture scenarios that allow us to characterize earthquakes and understand how ground motion can impact different areas based on proximity to source. For this study, we utilized HR-GNSS synthetic observations, which have been shown to complement seismic data by avoiding saturation at larger magnitudes (Crowell et al., 2013; Melgar et al., 2015). This integration enhances our ability to analyze and assess seismic and tsunami hazards, further advancing our understanding of earthquake behavior and its impacts in the region of interest. As more data sources are available, better decisions can be made during an earthquake response in a timely manner to save lives.

4.6. Acknowledgments

We would like to express our gratitude to Earth Sciences New Zealand (formerly known as GNS Science Te Pū Ao) for providing the resources and support necessary for this research. A. Howell, E. D'Anastasio, E. Caballero and B. Fry are supported by New Zealand Ministry of Business, Innovation and Employment contract C05X2003 for the Rapid Characterization of Earthquakes and Tsunami (RCET) program. We also recognize funding from Aotearoa New Zealand National Tsunami Model support for B. Fry and the Natural Hazards Research Platform for support of A. Howell and B. Fry. The GeoNet GNSS network is sponsored by the New Zealand Government through its agencies: Natural Hazards Commission Toka Tū Ake (NHC), Earth Sciences New Zealand, Toitū Te Whenua Land Information New Zealand (LINZ) and the Ministry of Business, Innovation and Employment (MBIE). Finally, we thank Anna Kaiser, the editor Mathilde Radiguet, and two anonymous reviewers for their time and thoughtful comments, which helped improve the quality of this manuscript.

4.7. Data and Code Availability

Rupture models from both catalogs (RSQSim and FakeQuakes) and the simulated GNSS waveforms used in this study are publicly available in a Zenodo repository (Solares-Colón et al., 2025). FakeQuakes, which is part of the MudPy suite for source modeling, is available at https://github.com/UO-Geophysics/MudPy (release v1.3) and is also linked to our Zenodo repository. Additional scripts used to convert RSQSim outputs into FakeQuakes inputs for generating synthetic GNSS waveforms are available at https://github.com/mmsolares/rsqsim2fakequakes-tools . Figures were produced using the Python packages Matplotlib (Hunter, 2007), ObsPy (Beyreuther et al., 2010), and PyGMT (Tian et al., 2024).

4.8. Supporting Information

Model Parameter	**$Trench_{Lock}$ Value**
Rate and state (*a* value)	0.001
Rate and state (*b* value)	0.004
Coefficient of friction (μ_0)	0.6
Rate and state (D_c)	$1x10^{-5}$
Rate and state (α_0)	0.25
Rate and state (θ_0)	$2x10^{8}$
Initial shear stress (τ_0)	60
Initial normal stress (σ_0)	100
Slip-deficit Model (HSM)	Trench creep model used in the NSHM 2022
Slip-deficit Model (TKSZ)	20% of the plate rate between ~37˚S to ~29˚S, and 50% of the plate rate from ~29˚S to ~25˚S

Table 4.S1. Summary of the input parameters in RSQSim used to generate rupture scenario catalog (for details refer to Hughes et al., 2025); Hikurangi Subduction Margin (HSM); New Zealand National Seismic Hazard Model 2022 (NSHM 2022); Tonga-Kermadec Subduction Zone (TKSZ).

Study	A	B	C
Crowell et al. (2016)*	-6.687	1.500	-0.214
Goldberg et al. (2021)**	-3.841	0.937	-0.127

** Crowell et al. (2016) PGD scaling uses hypocentral distance and applies exponential distance weighting to favor stations closer to the source.*
*** Goldberg et al. (2021) PGD scaling uses generalized mean rupture distance.*

Table 4.S2. GNSS Ground Motion Model coefficients for waveform validation and G-FAST testing. For waveform validation we use Goldberg et al. (2021) using the generalized mean rupture distance, R_p, with a value of – 2.3 for the power of the mean (p). The advantage of using R_p as a distance metric is that it allows for a more realistic treatment of a finite source as opposed to assuming a large rupture is a point source (e.g. as with the hypocenter distance; for more details refer to Goldberg et al. 2021). G-FAST PGD scaling applies exponential weighting as a function of epicentral distance to prioritize stations closer to source, using a minimum of four stations and a 3 km/s travel-time mask to exclude those that have not yet experienced strong ground shaking, enabling rapid characterization of large events (for more details refer to Crowell et al., 2016).

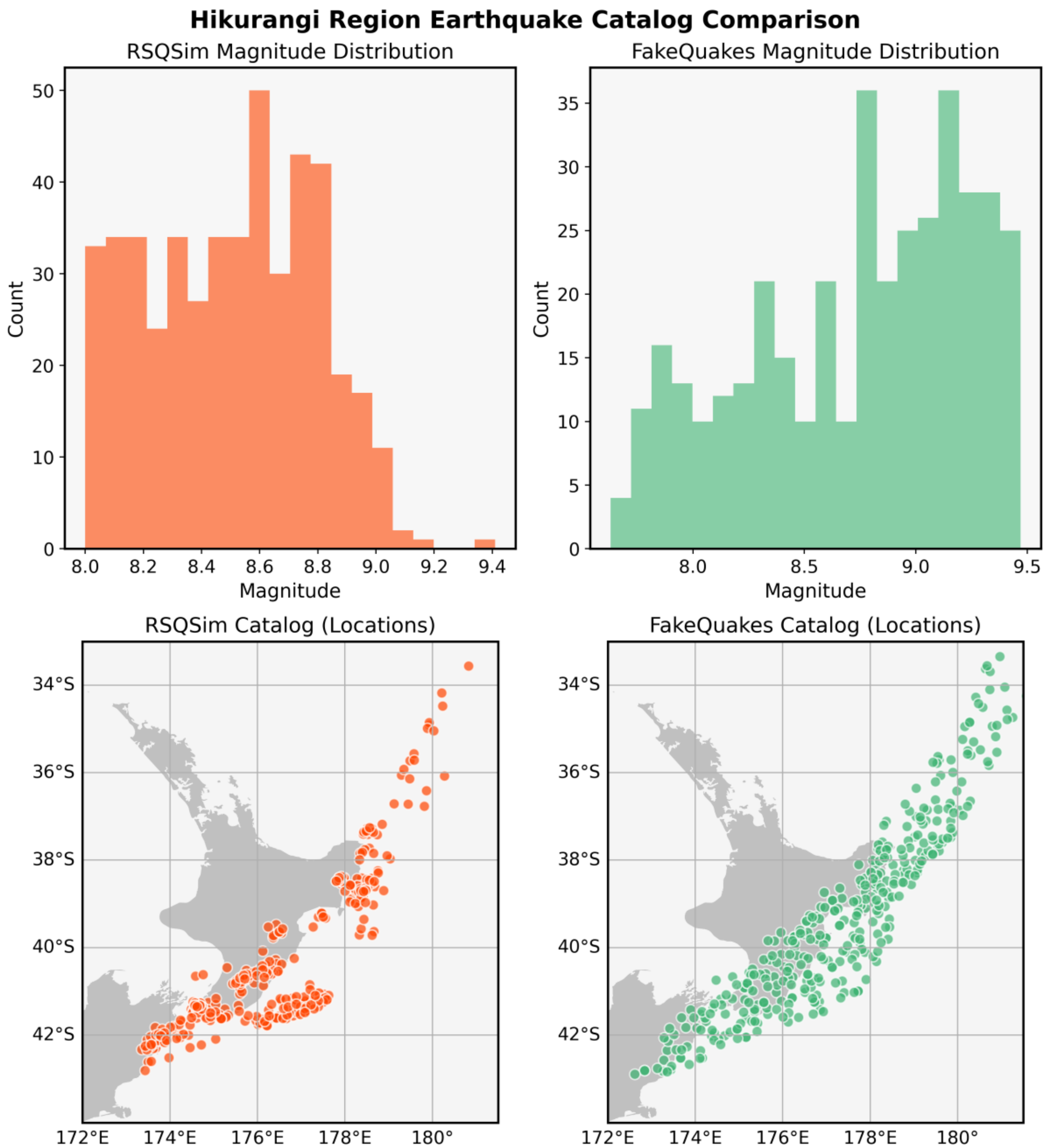

Figure 4.S1. Comparison of the two synthetic earthquake catalogs for New Zealand: RSQSim (in orange) and FakeQuakes (in green). Top panels show the magnitude distribution of earthquakes (histograms) for each catalog, while bottom panels show the spatial distribution of earthquakes (epicenters represented by circles) over the Hikurangi region. Both catalogs exhibit a similar geographic extent but show differences in event density and magnitude distributions that reflect variations in catalog generation methods. RSQSim represents a long-term synthetic seismicity history based on physics-based modeling, whereas FakeQuakes provides a more comprehensive suite of rupture scenarios designed to explore a wide range of magnitudes and locations.

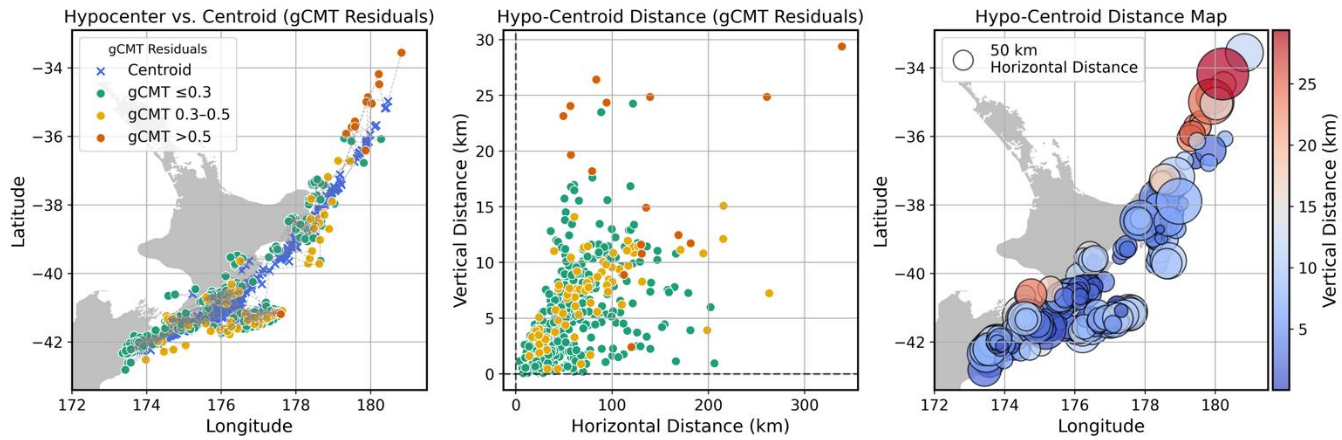

Figure 4.S2. Comparison of hypocenter and centroid locations with magnitude residual (Final – Target) categories for geodetic centroid moment tensor (gCMT) solutions. The left panel shows hypocenter locations (circles) and centroid locations (blue crosses) for gCMT residuals. Hypocenter locations are color-coded by error magnitude: green for low errors (≤0.3), yellow for moderate errors (0.3–0.5), and red for large errors (>0.5), corresponding to varying residual magnitudes. The middle panel presents hypocenter vs. centroid locations for gCMT residuals, following the same residual categorization. The right panel displays a hypocenter map, where marker size and color represent the horizontal and vertical distances, respectively, between the hypocenter and centroid.

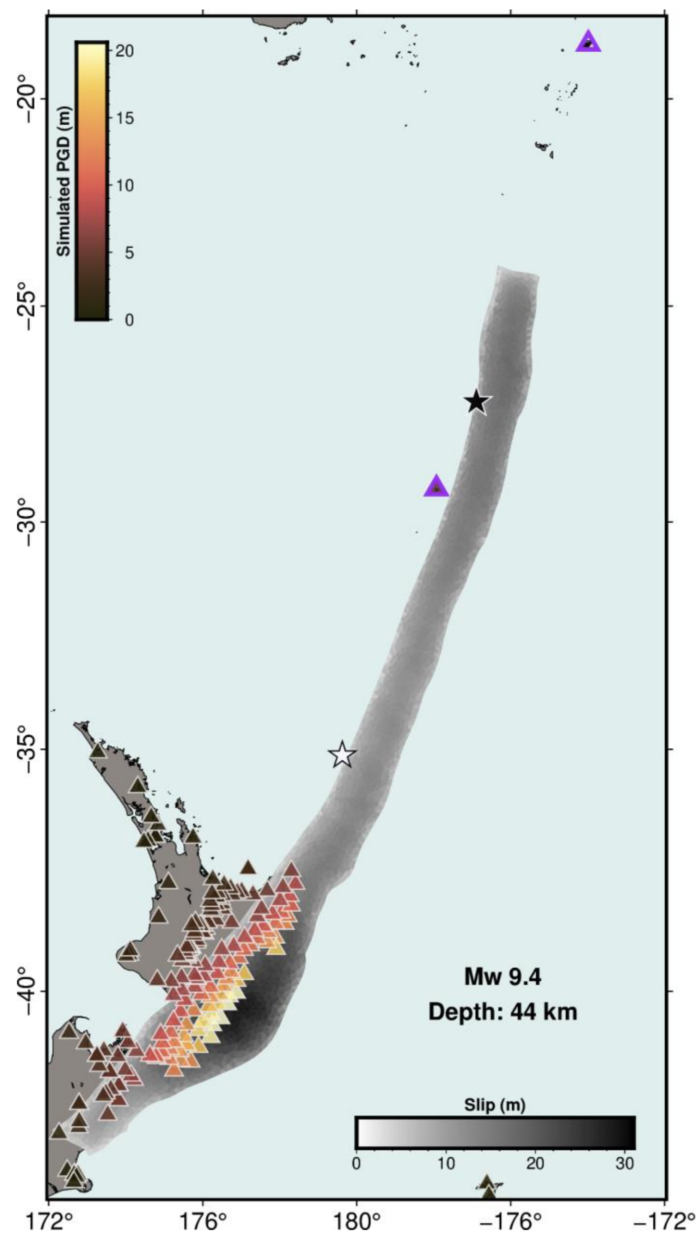

Figure 4.S3. An extraordinary case of a full-rupture M9.4 event in the Kermadec-Tonga subduction system, where G-FAST is unable to produce a solution because the stations are too far from the hypocenter to compute a reliable estimate. The map shows observed peak ground displacement (PGD) values at each station (color-filled triangles) within 1000 km, based on the distance from the station to the entire rupture plane (R_p), shown in warm colormap. The grayscale colormap represents the amount of rupture slip for reference. Triangles with thick purple borders indicate stations within 1000 km based on the distance from the station to the hypocenter (R_{hypo}). The black star shows the hypocenter, while the white star represents the centroid location. Labels indicate the magnitude and depth of the event.

CHAPTER 5

CONCLUSIONS AND FUTURE DIRECTIONS

This dissertation contributes to the advancement of earthquake science by improving our understanding of rupture processes, with emphasis on aspects that can be applied in real-world settings. From waveforms to source and back, the work presented here builds on finite fault models to refine scaling laws, generate realistic rupture scenarios, and evaluate early warning system performance—expanding our perspective on rupture complexity and variability. The findings presented in this dissertation, not only advances scientific knowledge, but also supports practical efforts in earthquake preparedness, hazard assessment, and response.

There is always something to learn about each earthquake. In Chapter 2, we modeled a moderate **M**6.4 earthquake in efforts to understand what it might reveal about future seismic events. This investigation focused on the seismic sequence in southwestern Puerto Rico during 2020. The mainshock stands as the most memorable event in the Island since the 1918 **M**7.2 tsunamigenic earthquake. It also challenged scientists to explain both its cause and unusually high productivity of aftershocks. Because this was the first major seismic sequence in the region to be recorded with modern instrumentation and given the wealth of available seismic and geodetic data, it presented an excellent opportunity to model the rupture in more detail. Our findings indicate a multi-segment rupture and a slow-evolving rupture process, both of which contribute to future seismic hazard assessments and help clarify the causative fault(s) of the mainshock. Could the long rupture duration of the mainshock reflect two independent sources? Was it a single slow rupture that triggered a second event? Or is this slow-evolving behavior unique to this mainshock, or perhaps characteristic of the region? These questions may not have definitive answers, but they are worth investigating. They also highlight the need to continue developing methods that can help us better resolve such complexities.

The timing and location of an earthquake are critical, destructive impacts are not limited to great earthquakes (**M**9s). Significant earthquakes, such as the **M**6.4 event discussed in Chapter 2, demonstrated that smaller earthquake can also be complex ruptures with substantial societal and infrastructure impact. As observational capabilities and modeling techniques continue to improve overtime, it becomes essential to revisit prior assumptions and update models accordingly. In Chapter 3, we expanded a finite-fault model catalog to explore rupture behavior across a wider range of events from general to local scale. What each type of datatype (i.e., seismic, strong motion and geodetic observations) contributes to the slip modes remains subject of investigation. Moving forward, retrospective analyses of slip models and the inclusion of regional data, where available, are crucial for advancing our understanding of source scaling.

Chapter 4 concludes this dissertation by presenting a framework to evaluate the performance of a geodetic early warning algorithm with synthetic data for large subduction earthquakes in New Zealand. Compared to similar studies, we used rupture scenarios from a physics-informed earthquake simulator, rather than simpler semi-stochastic approaches, to generate synthetic GNSS waveforms. These waveforms were validated against ground motion models that are based on geodetic observations from earthquakes worldwide. We tested whether ingesting synthetic waveforms from these scenarios would allow us to recover the original source characteristics. While the match was not always perfect, the approach proved to be a reliable method for evaluating the performance of earthquake early warning systems, identifying specific limitations in magnitude estimation, and highlighting where algorithmic refinements or network densification may be needed. While our case study focused on New Zealand, this work contributes to the continued development and integration of G-FAST into their operational systems. Future improvements to this framework could include incorporating real GNSS noise characteristics from the region into the generation of synthetic waveforms to better approximate ruptures scenarios in the relevant tectonic setting. Additional applications include using these ruptures scenarios to explore near-field tsunami forecasting and assess the impact of station dropouts and latency on early warning performance.

THE END.

This marks the end of my dissertation, but the journey continues. There will always be questions worth asking, and as scientists, we should seek them out and continue to reinvent ourselves in pursuit of more resilient communities and a better future.

REFERENCES CITED

Aagaard, B. T., Brocher, T. M., Dolenc, D., Dreger, D., Graves, R. W., Harmsen, S., Hartzell, S., Larsen, S., & Zoback, M. L. (2008). Ground-Motion Modeling of the 1906 San Francisco Earthquake, Part I: Validation Using the 1989 Loma Prieta Earthquake. *Bulletin of the Seismological Society of America*, *98*(2), 989–1011. https://doi.org/10.1785/0120060409

Adames-Corraliza, Á. R. (2017). *Geomorphic and geophysical characterization of the North Boquerón Bay-Punta Montalva fault zone: A capable fault system in southwestern Puerto Rico* [M.Sc. Thesis]. University of Puerto Rico at Mayagüez.

Addarich-Martínez, L. (2009). *The geologic mapping and history of the Guánica quadrangle, southwestern Puerto Rico* [M.Sc. Thesis]. University of Puerto Rico at Mayagüez.

Aguirre, P., Vásquez, J., Llera, J. C., González, J., & González, G. (2018). Earthquake damage assessment for deterministic scenarios in Iquique, Chile. *Natural Hazards*, *92*(3), 1433–1461. https://doi.org/10.1007/s11069-018-3258-3

Aki, K. (1967). Scaling law of seismic spectrum. *Journal of Geophysical Research*, *72*(4), 1217–1231. https://doi.org/10.1029/JZ072i004p01217

Allen, R. M., & Melgar, D. (2019). Earthquake early warning: Advances, scientific challenges, and societal needs. *Annual Review of Earth and Planetary Sciences*, *47*(1), 361–388. https://doi.org/10.1146/annurev-earth-053018-060457

Ammon, C. J., Ji, C., Thio, H.-K., Robinson, D., Ni, S., Hjorleifsdottir, V., Kanamori, H., Lay, T., Das, S., Helmberger, D., Ichinose, G., Polet, J., & Wald, D. (2005). Rupture process of the 2004 Sumatra-Andaman earthquake. *Science*, *308*(5725), 1133–1139. https://doi.org/10.1126/science.1112260

Andrews, D. J. (2005). Rupture dynamics with energy loss outside the slip zone. *Journal of Geophysical Research: Solid Earth*, *110*(B1), 2004JB003191. https://doi.org/10.1029/2004JB003191

Andrews, D. J. (2010). Ground motion hazard from supershear rupture. *Tectonophysics*, *493*(3–4), 216–221. https://doi.org/10.1016/j.tecto.2010.02.003

Andrews, J., Behr, Y., Böse, M., Massin, F., Kaiser, A., & Fry, B. (2024). Rapid earthquake rupture characterization for New Zealand using the FinDer algorithm. *Bulletin of the Seismological Society of America*, *114*(2), 775–793. https://doi.org/10.1785/0120230213

Asencio, E. (1980). *Western Puerto Rico seismicity* (U.S. Geological Survey Open-File Report No. 80-192; p. 144). https://doi.org/10.3133/ofr80192

Baltay, A. S., & Boatwright, J. (2015). Ground-motion observations of the 2014 South Napa earthquake. *Seismological Research Letters*, *86*(2A), 355–360. https://doi.org/10.1785/0220140232

Barbot, S. (2023). Motorcycle: A spectral boundary-integral method for seismic cycles on multiple faults. *Journal of Open Source Software*, *8*(91), 5097. https://doi.org/10.21105/joss.05097

Ben-Zion, Y. (2001). Dynamic ruptures in recent models of earthquake faults. *Journal of the Mechanics and Physics of Solids*, *49*(9), 2209–2244. https://doi.org/10.1016/S0022-5096(01)00036-9

Bertiger, W., Bar-Sever, Y., Dorsey, A., Haines, B., Harvey, N., & Hemberger, D. (2020). GipsyX/RTGx, a new tool set for space geodetic operations and research. *Advances in Space Research*, *66*(3), 469–489. https://doi.org/10.1016/j.asr.2020.04.015

Beyreuther, M., Barsch, R., Krischer, L., Megies, T., Behr, Y., & Wassermann, J. (2010). ObsPy: A Python toolbox for seismology. *Seismological Research Letters*, *81*(3), 530–533. https://doi.org/10.1785/gssrl.81.3.530

Bizzarri, A. (2012). Rupture speed and slip velocity: What can we learn from simulated earthquakes? *Earth and Planetary Science Letters*, *317–318*, 196–203. https://doi.org/10.1016/j.epsl.2011.11.023

Blaser, L., Kruger, F., Ohrnberger, M., & Scherbaum, F. (2010). Scaling relations of earthquake source parameter estimates with special focus on subduction environment. *Bulletin of the Seismological Society of America*, *100*(6), 2914–2926. https://doi.org/10.1785/0120100111

Blasweiler, M., Herman, M. W., Houtsma, F., & Govers, R. (2022). Tectonic context and possible triggering of the 2019–2020 Puerto Rico earthquake sequence. *Seismological Research Letters*, *93*(2A), 584–593. https://doi.org/10.1785/0220210224

Boore, D. M., Stewart, J. P., Seyhan, E., & Atkinson, G. M. (2014). NGA-West2 equations for predicting PGA, PGV, and 5% damped PSA for shallow crustal earthquakes. *Earthquake Spectra*, *30*(3), 1057–1085. https://doi.org/10.1193/070113EQS184M

Bouchon, M., Karabulut, H., Bouin, M.-P., Schmittbuhl, J., Vallée, M., Archuleta, R., Das, S., Renard, F., & Marsan, D. (2010). Faulting characteristics of supershear earthquakes. *Tectonophysics*, *493*(3–4), 244–253. https://doi.org/10.1016/j.tecto.2010.06.011

Brink, U. S., Marshak, S., & Bruña, J. -L. G. (2009). Bivergent thrust wedges surrounding oceanic island arcs: Insight from observations and sandbox models of the northeastern Caribbean plate. *Geological Society of America Bulletin*, *121*(11–12), 1522–1536.

Brink, U. S., Vanacore, E. A., Fielding, E. J., Chaytor, J. D., López-Venegas, A. M., & Baldwin, W. E. (2022). Mature diffuse tectonic block boundary revealed by the 2020 southwestern Puerto Rico seismic sequence. *Tectonics*, *41*(3), 2021 006896.

Brune, J. N. (1970). Tectonic stress and the spectra of seismic shear waves from earthquakes. *Journal of Geophysical Research*, *75*(26), 4997–5009. https://doi.org/10.1029/JB075i026p04997

Cárdenas, D. R., Miller, M., & Montalva, G. A. (2024). Subduction Interface Earthquake Rise-Time Scaling Relations. *Bulletin of the Seismological Society of America*, *114*(1), 278–290. https://doi.org/10.1785/0120230129

Chaytor, J. D., & Brink, U. S. (2010). Extension in Mona passage, northeast Caribbean. *Tectonophysics*, *493*(1–2), 74–92.

Cirella, A., Piatanesi, A., Tinti, E., Chini, M., & Cocco, M. (2012). Complexity of the rupture process during the 2009 L'Aquila, Italy, earthquake: Source complexity of the L'Aquila Earthquake. *Geophysical Journal International*, *190*(1), 607–621. https://doi.org/10.1111/j.1365-246X.2012.05505.x

Clark, K., Howarth, J., Litchfield, N., Cochran, U., Turnbull, J., Dowling, L., Howell, A., Berryman, K., & Wolfe, F. (2019). Geological evidence for past large earthquakes and tsunamis along the Hikurangi subduction margin. *New Zealand. Marine Geology*, *412*, 139–172. https://doi.org/10.1016/j.margeo.2019.03.004

Convers, J. A., & Newman, A. V. (2011). Global evaluation of large earthquake energy from 1997 through mid-2010. *Journal of Geophysical Research*, *116*(B8), 08304. https://doi.org/10.1029/2010JB007928

Copernicus Sentinel data. (2020). Retrieved from ASF DAAC (Last Accessed on August 30, 2024), Processed by ESA.

Cromwell, C. W., Furlong, K. P., Bergman, E. A., Benz, H. M., Yeck, W. L., & Herman, M. (2022). Seismotectonic analysis of the 2019–2020 Puerto Rico sequence: The value of absolute earthquake relocations in improved interpretations of active tectonics. *Seismological Research Letters*, *93*(2A), 544–554. https://doi.org/10.1785/0220210238

Crowell, B. W. (2024). Chapter 6—Earthquake and tsunami early warning with GNSS data. In Y. Aoki & C. Kreemer (Eds.), *GNSS monitoring of the terrestrial environment* (pp. 111–127). https://doi.org/10.1016/B978-0-323-95507-2.00004-9

Crowell, B. W., Bock, Y., & Melgar, D. (2012). Real-time inversion of GPS data for finite fault modeling and rapid hazard assessment. *Geophysical Research Letters*, *39*, 09305. https://doi.org/10.1029/2012GL051318

Crowell, B. W., Melgar, D., Bock, Y., Haase, J. S., & Geng, J. (2013). Earthquake magnitude scaling using seismogeodetic data. *Geophysical Research Letters*, *40*(23), 6089–6094. https://doi.org/10.1002/2013GL058391

Crowell, B. W., Schmidt, D. A., Bodin, P., Vidale, J. E., Baker, B., Barrientos, S., & Geng, J. (2018). G-FAST earthquake early warning potential for great earthquakes in Chile. *Seismological Research Letters*, *89*(2A), 542–556. https://doi.org/10.1785/0220170180

Crowell, B. W., Schmidt, D. A., Bodin, P., Vidale, J. E., Gomberg, J., Hartog, J. R., Kress, V. C., Melbourne, T. I., Santillan, M., Minson, S. E., & Jamison, D. G. (2016). Demonstration of the Cascadia G-FAST geodetic earthquake early warning system for the Nisqually, Washington, earthquake. *Seismological Research Letters*, *87*(4), 930–943. https://doi.org/10.1785/0220150255

Delogkos, E., Howell, A., Seebeck, H., Shaw, B. E., Nicol, A., Liao, Y. M., & Walsh, J. J. (2023). Impact of variable fault geometries and slip rates on earthquake catalogs from physics-based simulations of a normal fault. *Journal of Geophysical Research: Solid Earth*, *128*(11), 2023 026746. https://doi.org/10.1029/2023JB026746

DeMets, C., Gordon, R. G., & Argus, D. F. (2010). Geologically current plate motions. *Geophysical Journal International*, *181*(1), 1–80. https://doi.org/10.1111/j.1365

Diao, H., Ren, Y., Wen, R., Si, H., & Koketsu, K. (2025). Supershear rupture process of the 2025 Myanmar earthquake as derived from joint inversion of near-field and teleseismic waveforms. *Earthquake Engineering and Engineering Vibration*, *24*(4), 917–925. https://doi.org/10.1007/s11803-025-2347-z

Dieterich, J. H. (1979). Modeling of rock friction: 1. Experimental results and constitutive equations. *Journal of Geophysical Research: Solid Earth*, *84*(B5), 2161–2168. https://doi.org/10.1029/JB084iB05p02161

Dissen, R. J., Johnson, K. M., Seebeck, H., Wallace, L. M., Rollins, C., Maurer, J., Gerstenberger, M. C., Williams, C. A., Hamling, I. J., Howell, A., & DiCaprio, C. J. (2024). Upper plate and subduction interface deformation models in the 2022 revision of the

Aotearoa New Zealand National Seismic Hazard Model. *Bulletin of the Seismological Society of America*, *114*(1), 37–56. https://doi.org/10.1785/0120230118

Doser, D. I., Rodríguez, C. M., & Flores, C. (2005). Historical earthquakes of the Puerto Rico–Virgin Islands region. In P. Mann (Ed.), *Active tectonics and seismic hazards of Puerto Rico, the Virgin Islands, and offshore areas* (pp. 103–114). https://doi.org/10.1130/0

Duan, B., & Oglesby, D. (2005). The Dynamics of Thrust and Normal Faults over Multiple Earthquake Cycles: Effects of Dipping Fault Geometry. *Bulletin of the Seismological Society of America*, *95*(5), 1623–1636. https://doi.org/10.1785/0120040234

Duputel, Z., Jiang, J., Jolivet, R., Simons, M., Rivera, L., Ampuero, J. -P., Riel, B., Owen, S. E., Moore, A. W., Samsonov, S. V., Ortega Culaciati, F., & Minson, S. E. (2015). The Iquique earthquake sequence of April 2014: Bayesian modeling accounting for prediction uncertainty. *Geophysical Research Letters*, *42*(19), 7949–7957. https://doi.org/10.1002/2015GL065402

Duputel, Z., & Rivera, L. (2017). Long-period analysis of the 2016 Kaikoura earthquake. *Physics of the Earth and Planetary Interiors*, *265*, 62–66. https://doi.org/10.1016/j.pepi.2017.02.004

EarthScope Data Management Center. (2013). *Data services products: EQEnergy earthquake energy & rupture duration* [Dataset]. https://doi.org/10.17611/DP/18022068

Elst, N. J., Hardebeck, J. L., Michael, A. J., McBride, S. K., & Vanacore, E. (2022). Prospective and retrospective evaluation of the U.S. Geological Survey public aftershock forecast for the 2019–2021 southwest Puerto Rico earthquake and aftershocks. *Seismological Research Letters*, *93*(2A), 620–640. https://doi.org/10.1785/0220210222

Funning, G. J., Fukahata, Y., Yagi, Y., & Parsons, B. (2014). A method for the joint inversion of geodetic and seismic waveform data using ABIC: Application to the 1997 Manyi, Tibet, earthquake. *Geophysical Journal International*, *196*(3), 1564–1579. https://doi.org/10.1093/gji/ggt406

Gabriel, A. -A., Ampuero, J. -P., Dalguer, L. A., & Mai, P. M. (2012). The transition of dynamic rupture styles in elastic media under velocity-weakening friction. *Journal of Geophysical Research: Solid Earth*, *117*(B9), 2012JB009468. https://doi.org/10.1029/2012JB009468

Gabriel, A. -A., Ampuero, J. -P., Dalguer, L. A., & Mai, P. M. (2013). Source properties of dynamic rupture pulses with off-fault plasticity. *Journal of Geophysical Research: Solid Earth*, *118*(8), 4117–4126. https://doi.org/10.1002/jgrb.50213

Gerstenberger, M. C., Bora, S., Bradley, B. A., DiCaprio, C., Kaiser, A., Manea, E. F., Nicol, A., Rollins, C., Stirling, M. W., Thingbaijam, K. K. S., Dissen, R. J., Abbott, E. R., Atkinson, G. M., Chamberlain, C., Christophersen, A., Clark, K., Coffey, G. L., Torre, C. A., Ellis, S. M., … Wotherspoon, L. M. (2023). The 2022 Aotearoa New Zealand National Seismic Hazard Model: Process, overview, and results. *Bulletin of the Seismological Society of America*, *114*(1), 7–36. https://doi.org/10.1785/0120230182

Given, D. D., Allen, R. M., Baltay, A. S., Bodin, P., Cochran, E. S., Creager, K., Groot, R. M., Gee, L. S., Hauksson, E., Heaton, T. H., Hellweg, M., Murray, J. R., Thomas, V. I., Toomey, D., & Yelin, T. S. (2018). Revised technical implementation plan for the ShakeAlert system—An earthquake early warning system for the West Coast of the United States (Open-File Report No. 2018-1155. *U.S. Geological Survey*. https://doi.org/10.3133/ofr20181155

GNS Science. (2019). *GeoNet Aotearoa New Zealand stations metadata repository* [Dataset]. GNS Science, GeoNet. https://doi.org/10.21420/0VY2-C144

Goldberg, D. E., Koch, P., Melgar, D., Riquelme, S., & Yeck, W. L. (2022). Beyond the teleseism: Introducing regional seismic and geodetic data into routine USGS finite-fault modeling. *Seismological Research Letters*, *93*(6), 3308–3323. https://doi.org/10.1785/0220220047

Goldberg, D. E., Melgar, D., Hayes, G. P., Crowell, B. W., & Sahakian, V. J. (2021). A ground-motion model for GNSS peak ground displacement. *Bulletin of the Seismological Society of America*, *111*(5), 2393–2407. https://doi.org/10.1785/0120210042

Granja-Bruña, J. L., Ten Brink, U. S., Carbó-Gorosabel, A., Muñoz-Martín, A., & Gómez Ballesteros, M. (2009). Morphotectonics of the central Muertos thrust belt and Muertos Trough (northeastern Caribbean. *Marine Geology*, *263*(1–4), 7–33. https://doi.org/10.1016/j.margeo.2009.

Granja-Bruña, J. L., Ten Brink, U. S., Muñoz-Martín, A., Carbó-Gorosabel, A., & Llanes Estrada, P. (2015). Shallower structure and geo- morphology of the southern Puerto Rico offshore margin. *Marine and Petroleum Geology*, *67*, 30–56. https://doi.org/10.1016/j.marpetgeo.

Graves, R., & Pitarka, A. (2015). Refinements to the Graves and Pitarka (2010) broadband ground-motion simulation method. *Seismological Research Letters*, *86*(1), 75–80. https://doi.org/10.1785/0220140101

Graves, R., & Pitarka, A. (2010). Broadband ground-motion simulation using a hybrid approach. *Bulletin of the Seismological Society of America*, *100*(5A), 2095–2123. https://doi.org/10.1785/0120100057

Gusev, A. A., & Chebrov, D. (2019). On Scaling of Earthquake Rise-Time Estimates. *Bulletin of the Seismological Society of America*, *109*(6), 2741–2745. https://doi.org/10.1785/0120180214

Hamling, I. J. (2020). A review of the 2016 Kaikōura earthquake: Insights from the first 3 years. *Journal of the Royal Society of New Zealand*, *50*(2), 226–244. https://doi.org/10.1080/03036758.2019.1701048

Hanssen, R. F. (2001). *Radar interferometry: Data interpretation and error analysis* (Vol. 2). Springer Science & Business Media.

Hayes, G. P. (2018). *Slab2—A Comprehensive Subduction Zone Geometry Model* [Dataset]. U.S. Geological Survey. https://doi.org/10.5066/F7PV6JNV

Hayes, G. P. (2017). The finite, kinematic rupture properties of great-sized earthquakes since 1990. *Earth and Planetary Science Letters*, *468*, 94–100. https://doi.org/10.1016/j.epsl.2017.04.003

Heaton, T. H. (1990). Evidence for and implications of self-healing pulses of slip in earthquake rupture. *Physics of the Earth and Planetary Interiors*, *64*(1), 1–20. https://doi.org/10.1016/0031-9201(90)90002-F

Hok, S., Fukuyama, E., & Hashimoto, C. (2011). Dynamic rupture scenarios of anticipated Nankai-Tonankai earthquakes, southwest Japan. *Journal of Geophysical Research*, *116*(B12), 12319. https://doi.org/10.1029/2011JB008492

Howarth, J. D., Barth, N. C., & Fitzsimons, S. J. (2021). Spatiotemporal clustering of great earthquakes on a transform fault controlled by geometry. *Nature Geoscience*, *14*(4), 314–320. https://doi.org/10.1038/s41561-021-00721-4

Hughes, L., Lane, E. M., Power, W., Savage, M. K., Arnold, R., Howell, A., Liao, Y.-W. M., Williams, C., Shaw, B., Fry, B., & Nicol, A. (2025). Effects of subduction interface locking distributions on tsunami hazard: A case study on the Hikurangi/Tonga-Kermadec subduction zones. *Geophysical Journal International*, *240*(2), 1147–1167. https://doi.org/10.1093/gji/ggae441

Hughes, L., Power, W., Lane, E. M., Savage, M. K., Arnold, R., Howell, A., Shaw, B., Fry, B., & Nicol, A. (2023). A novel method to determine probabilistic tsunami hazard using a physics-based synthetic earthquake catalog: A New Zealand case study. *Journal of Geophysical Research: Solid Earth*, *128*(12), 2023 027207. https://doi.org/10.1029/2023JB027207

Hunter, J. D. (2007). Matplotlib: A 2D graphics environment. *Computing in Science & Engineering*, *9*(3), 90–95. https://doi.org/10.1109/MCSE.2007.55

Jansma, P. E., & Mattioli, G. S. (2005). GPS results from Puerto Rico and the Virgin Islands: Constraints on tectonic setting and rates of active faulting. *Active Tectonics and Seismic Hazards of Puerto Rico, the Virgin Islands, and Offshore Areas*, *385*, 13–30. https://doi.org/10.1130/0

Ji, C., Helmberger, D. V., Wald, D. J., & Ma, K. (2003). Slip history and dynamic implications of the 1999 Chi-Chi, Taiwan, earthquake. *Journal of Geophysical Research: Solid Earth*, *108*(B9), Article B9. https://doi.org/10.1029/2002JB001764

Ji, C., Wald, D. J., & Hemberger, D. V. (2002). Source Description of the 1999 Hector Mine, California, Earthquake, Part I: Wavelet Domain Inversion Theory and Resolution Analysis. *Bulletin of the Seismological Society of America*, *92*(4), Article 4. https://doi.org/10.1785/0120000916

Kanamori, H. (1972). Mechanism of tsunami earthquakes. *Physics of the Earth and Planetary Interiors*, *6*(5), 346–359.

Kearse, J., & Kaneko, Y. (2025). *Curved fault slip captured by CCTV video during the 2025 Mw 7.7 Mandalay earthquake*. Geophysics and Seismology. https://doi.org/10.31223/X5TF0B

Kiser, E., & Ishii, M. (2012). The March 11, 2011 Tohoku-oki earthquake and cascading failure of the plate interface. *Geophysical Research Letters*, *39*(7), 2012GL051170. https://doi.org/10.1029/2012GL051170

Koch, P., Bravo, F., Riquelme, S., & Crempien, J. G. F. (2019). Near-Real-Time Finite-Fault Inversions for Large Earthquakes in Chile Using Strong-Motion Data. *Seismological Research Letters*. https://doi.org/10.1785/0220180294

Koch, P., Goldberg, D. E., Hunsinger, H. E., Melgar, D., Riquelme, S., Yeck, W. L., & Haynie, K. L. (2024). *Wavelet and simulated Annealing SliP inversion (WASP)* [Computer software]. U.S. Geological Survey. https://doi.org/10.5066/P1EKKUNW

Konca, A. O., Kaneko, Y., Lapusta, N., & Avouac, J.-P. (2013). Kinematic Inversion of Physically Plausible Earthquake Source Models Obtained from Dynamic Rupture

Simulations. *Bulletin of the Seismological Society of America*, *103*(5), 2621–2644. https://doi.org/10.1785/0120120358

Kostrov, B. V. (1964). Selfsimilar problems of propagation of shear cracks. *Journal of Applied Mathematics and Mechanics*, *28*(5), 1077–1087. https://doi.org/10.1016/0021-8928(64)90010-3

Kurahashi, S., & Irikura, K. (2011). Source model for generating strong ground motions during the 2011 off the Pacific coast of Tohoku Earthquake. *Earth, Planets and Space*, *63*(7), 571–576. https://doi.org/10.5047/eps.2011.06.044

Latour, S., Lebihain, M., Bhat, H. S., Twardzik, C., Bletery, Q., Hudnut, K. W., & Passelègue, F. (2025). Direct estimation of earthquake source properties from a single CCTV camera. *Science*, *390*(6772), 463–467. https://doi.org/10.1126/science.adz1705

Laurencin, M., Marcaillou, B., Graindorge, D., Klingelhoefer, F., Lallemand, S., Laigle, M., & Lebrun, J. -F. (2017). The polyphased tectonic evolution of the Anegada passage in the northern Lesser Antilles subduction zone. *Tectonics*, *36*(5), 945–961.

Lay, T. (2018). A review of the rupture characteristics of the 2011 Tohoku-Oki Mw 9.1 earthquake. *Tectonophysics*, *733*, 4–36. https://doi.org/10.1016/j.tecto.2017.09.022

Lay, T., Ammon, C. J., Kanamori, H., Koper, K. D., Sufri, O., & Hutko, A. R. (2010). Teleseismic inversion for rupture process of the 27 February 2010 Chile (M_w 8.8) earthquake. *Geophysical Research Letters*, *37*(13), 2010GL043379. https://doi.org/10.1029/2010GL043379

Lay, T., Kanamori, H., Ammon, C. J., Koper, K. D., Hutko, A. R., Ye, L., Yue, H., & Rushing, T. M. (2012). Depth-varying rupture properties of subduction zone megathrust faults. *Journal of Geophysical Research: Solid Earth*, *117*(B4), 2011JB009133. https://doi.org/10.1029/2011JB009133

Lay, T., Kanamori, H., Ammon, C. J., Nettles, M., Ward, S. N., Aster, R. C., Beck, S. L., Bilek, S. L., Brudzinski, M. R., Butler, R., DeShon, H. R., Ekström, G., Satake, K., & Sipkin, S. (2005). The great Sumatra-Andaman earthquake of 26 December 2004. *Science*, *308*(5725), 1127–1133. https://doi.org/10.1126/science.1112250

LeVeque, R. J., Waagan, K., González, F. I., Rim, D., & Lin, G. (2016). Generating random earthquake events for probabilistic tsunami hazard assessment. In E. L. Geist, H. M. Fritz, A. B. Rabinovich, & Y. Tanioka (Eds.), *Global tsunami science: Past and future: Vol. I* (pp. 3671–3692). Springer International Publishing. https://doi.org/10.1007/978-3-319-55480-8_2

Liu, C., Lay, T., Wang, Z., & Xiong, X. (2020). Rupture process of the 7 January 2020, Mw 6.4 Puerto Rico earthquake. *Geophysical Research Letters*, *47*(12), 2020 087718. https://doi.org/10.1029/2020GL087718

Lohman, R. B., & Simons, M. (2005). Some thoughts on the use of InSAR data to constrain models of surface deformation: Noise structure and data downsampling. *Geochemistry, Geophysics, Geosystems*, *6*(1), 01007. https://doi.org/10.1029/2004GC000841

López-Venegas, A. M., Hughes, K. S., & Vanacore, E. (2020). Puerto Rico's winter 2019-2020 seismic sequence leaves the island on edge. *Temblor*, *19*(8), 41–61. https://doi.org/10.32858/temblor.064

López-Venegas, A. M., Mattioli, G. S., Solares-Colón, M., Mencin, D., & Jansma, P. E. (2022). Estimating coseismic deformation of southwestern Puerto Rico from the 7 January 2020 Mw 6.4 earthquake: Constraints from campaign and continuous GPS. *Bulletin of the Seismological Society of America*, *113*(1), 99–114. https://doi.org/10.1785/0120220115

Mai, P. M., & Beroza, G. C. (2000). Source Scaling Properties from Finite-Fault-Rupture Models. *Bulletin of the Seismological Society of America*, *90*(3), 604–615. https://doi.org/10.1785/0119990126

Mai, P. M., & Beroza, G. C. (2002). A spatial random field model to characterize complexity in earthquake slip. *Journal of Geophysical Research: Solid Earth*, *107*(B11), 2308. https://doi.org/10.1029/2001JB000588

Mai, P. M., & Thingbaijam, K. K. S. (2014). SRCMOD: An Online Database of Finite-Fault Rupture Models. *Seismological Research Letters*, *85*(6), 1348–1357. https://doi.org/10.1785/0220140077

McCann, W. R. (1985). On the earthquake hazards of Puerto Rico and the Virgin Islands. *Bulletin of the Seismological Society of America*, *75*(1), 251–262. https://doi.org/10.1785/BSSA0750010251

Melgar, D., Crowell, B. W., Geng, J., Allen, R. M., Bock, Y., Riquelme, S., Hill, E. M., Protti, M., & Ganas, A. (2015). Earthquake magnitude calculation without saturation from the scaling of peak ground displacement. *Geophysical Research Letters*, *42*(13), 5197–5205. https://doi.org/10.1002/2015GL064278

Melgar, D., Crowell, B. W., Melbourne, T. I., Szeliga, W., Santillan, M., & Scrivner, C. (2020). Noise characteristics of operational real-time high-rate GNSS positions in a large aperture network. *Journal of Geophysical Research: Solid Earth*, *125*(7), 2019 019197. https://doi.org/10.1029/2019jb019197

Melgar, D., Ganas, A., Geng, J., Liang, C., Fielding, E. J., & Kassaras, I. (2017). Source characteristics of the 2015 Mw 6.5 Lefkada, Greece, strike- slip earthquake. *Journal of Geophysical Research: Solid Earth*, *122*(3), 2260–2273. https://doi.org/10.1002/2016JB013452

Melgar, D., & Hayes, G. P. (2017). Systematic observations of the slip pulse properties of large earthquake ruptures. *Geophysical Research Letters*, *44*(19), 9691–9698. https://doi.org/10.1002/2017GL074916

Melgar, D., LeVeque, R. J., Dreger, D. S., & Allen, R. M. (2016). Kinematic rupture scenarios and synthetic displacement data: An example application to the Cascadia subduction zone. *Journal of Geophysical Research: Solid Earth*, *121*(9), 6658–6674. https://doi.org/10.1002/2016JB013314

Melgar, D., Weldon, R., Wang, Y., Bato, M. G., Aung, L. T., Shi, X., Wiwegwing, W., Khaing, S. N., Min, S., Thant, M., Speed, C., Zinke, R., Fielding, E., Meltzner, A., & Dawson, T. (2025). Supershear source model of the 2025 M7.8 Myanmar earthquake and paleoseismology of the Sagaing Fault: Regions of significant overlap with past earthquakes. *Seismica*, *4*(2). https://doi.org/10.26443/seismica.v4i2.1771

Mena, B., Mai, P. M., Olsen, K. B., Purvance, M. D., & Brune, J. N. (2010). Hybrid broadband ground-motion simulation using scattering Green's functions: Application to large-magnitude events. *Bulletin of the Seismological Society of America*, *100*(5A), 2143–2162. https://doi.org/10.1785/0120080318

Minson, S. E., Baltay, A. S., Cochran, E. S., McBride, S. K., & Milner, K. R. (2021). Shaking is almost always a surprise: The earthquakes that produce significant ground motion. *Seismological Research Letters*, *92*(1), 460–468. https://doi.org/10.1785/0220200165

Minson, S. E., Simons, M., Beck, J. L., Ortega, F., Jiang, J., Owen, S. E., Moore, A. W., Inbal, A., & Sladen, A. (2014). Bayesian inversion for finite fault earthquake source models – II: The 2011 great Tohoku-oki, Japan earthquake. *Geophysical Journal International*, *198*(2), 922–940. https://doi.org/10.1093/gji/ggu170

Mori, N., Takahashi, T., Yasuda, T., & Yanagisawa, H. (2011). Survey of 2011 Tohoku earthquake tsunami inundation and run-up. *Geophysical Research Letters*, *38*(7), 00 05. https://doi.org/10.1029/2011GL049210

Murray, J. R., Crowell, B. W., Murray, M. H., Ulberg, C. W., McGuire, J. J., Aranha, M. A., & Hagerty, M. T. (2023). Incorporation of real-time earthquake magnitudes estimated via peak ground displacement scaling in the ShakeAlert earthquake early warning system. *Bulletin of* *the Seismological Society of America*, *113*(3), 1286–1310. https://doi.org/10.1785/012022018

National Geophysical Data Center/World Data Service: NCEI/WDS. (2024). *Global historical tsunami database* [Dataset]. NOAA National Centers for Environmental Information. https://doi.org/10.7289/V5PN93H7

Newman, A. V., & Okal, E. A. (1998). Teleseismic estimates of radiated seismic energy: The E/M0 discriminant for tsunami earthquakes. *Journal of Geophysical Research*, *103*(B11), 26885–26898. https://doi.org/10.1029/98JB02236

Nye, T., Sahakian, V., & Melgar, D. (2024). Modeling ground motions and crustal deformation from tsunami earthquakes: Rupture parameter constraints from the 2010 Mentawai event. *Seismica*, *3*(2). https://doi.org/10.26443/seismica.v3i2.1152

Okal, E. A., & Newman, A. V. (2001). Tsunami earthquakes: The quest for a regional signal. *Physics of the Earth and Planetary Interiors*, *124*(1– 2), 45–70. https://doi.org/10.1016/S0031

Orchiston, C., Mitchell, J., Wilson, T., Langridge, R., Davies, T., Bradley, B., Johnston, D., Davies, A., Becker, J., & McKay, A. (2018). Project AF8: Developing a coordinated, multi-agency response plan for a future great Alpine Fault earthquake. *New Zealand Journal of Geology and Geophysics*, *61*(3), 389–402. https://doi.org/10.1080/00288306.2018.1455716

Ozawa, S., Ida, A., Hoshino, T., & Ando, R. (2022). Large-scale earthquake sequence simulations on 3-D non-planar faults using the boundary element method accelerated by lattice H-matrices. *Geophysical Journal International*, *232*(3), 1471–1481. https://doi.org/10.1093/gji/ggac386

Parker, G. A., Stewart, J. P., Boore, D. M., Atkinson, G. M., & Hassani, B. (2022). NGA-subduction global ground motion models with regional adjustment factors. *Earthquake Spectra*, *38*(1), 456–493. https://doi.org/10.1177/87552930211034889

Pasyanos, M. E., Masters, T. G., Laske, G., & Ma, Z. (2014). LITHO1.0: An updated crust and lithospheric model of the Earth. *Journal of Geophysical Research: Solid Earth*, *119*(3), 2153–2173. https://doi.org/10.1002/2013JB010626

Petukhin, A., Galvez, P., Somerville, P., Ampuero, J.-P., Mai, P. M., Pitarka, A., Yoshida, K., & Irikura, K. (2025). Insights into Slip-Rate Time Functions, Rupture Parameter Correlations, and Ground Motions from Validated Multicycle Earthquake Ruptures. *Bulletin of the Seismological Society of America*, *115*(4), 1591–1610. https://doi.org/10.1785/0120240235

Piety, L. A., Redwine, J. R., Derouin, S. A., Prentice, C. S., Kelson, K. I., Klinger, R. E., & Mahan, S. (2018). Holocene surface ruptures on the Salinas fault and southeastern great southern Puerto Rico fault zone, south coastal plain of Puerto Rico. *Bulletin of the Seismological Society of America*, *108*(2), 619–638. https://doi.org/10.1785/0120170182

Prentice, C. S., & Mann, P. (2005). Paleoseismic study of the South Lajas fault: First documentation of an onshore Holocene fault in Puerto Rico. *Active Tectonics and Seismic Hazards of Puerto Rico, the Virgin Islands, and Offshore Areas*, *385*, 215–222. https://doi.org/10.1130/0

Pugh, D. J., White, R. S., & Christie, P. A. F. (2016). Automatic Bayesian polarity determination. *Geophysical Journal International*, *206*(1), 275–291. https://doi.org/10.1093/gji/ggw146

Rafiei, M., Khodaverdian, A., & Rahimian, M. (2022). A probabilistic physics-based seismic hazard model for the Alborz Region, Iran. *Bulletin of the Seismological Society of America*, *112*(4), 2141–2155. https://doi.org/10.1785/0120210238

Richards-Dinger, K., & Dieterich, J. H. (2012). RSQSim earthquake simulator. *Seismological Research Letters*, *83*(6), 983–990. https://doi.org/10.1785/0220120105

Roig-Silva, C. M., Asencio, E., & Joyce, J. (2013). The northwest trending North Boqueron Bay-Punta Montalva fault zone; A through going active fault system in southwestern Puerto Rico. *Seismological Research Letters*, *84*(3), 538–550. https://doi.org/10.1785/0220120115

Rosen, P. A., Gurrola, E. M., Agram, P., Cohen, J., Lavalle, M., & Riel, B. V. (2018). The InSAR scientific computing environment 3.0: A flexible framework for NISAR operational and user-led science processing. *IGARSS 2018 - 2018 IEEE International Geoscience and Remote Sensing Symposium*, 4897–4900. https://doi.org/10.1109/IGARSS.2018.8517504

Rösler, B., & Stein, S. (2022). Consistency of non-double-couple components of seismic moment tensors with earthquake magnitude and mechanism. *Seismological Research Letters*, *93*(3), 1510–1523. https://doi.org/10.1785/0220210188

Ruhl, C. J., Melgar, D., Grapenthin, R., & Allen, R. M. (2017). The value of real-time GNSS to earthquake early warning. *Geophysical Research Letters*, *44*(16), 8311–8319. https://doi.org/10.1002/2017GL074502

Sahakian, V. J., Baltay, A., Hanks, T., Buehler, J., Vernon, F., Kilb, D., & Abrahamson, N. (2018). Decomposing leftovers: Event, path, and site residuals for a small-magnitude Anza region GMPE. *Bulletin of the Seismological Society of America*, *108*(5A), 2478–2492.

Sahakian, V. J., Melgar, D., & Muzli, M. (2019). Weak near-field behavior of a tsunami earthquake: Toward real-time identification for local warning. *Geophysical Research Letters*, *46*(16), 9519–9528. https://doi.org/10.1029/2019GL083989

Satake, K., & Tanioka, Y. (1999). Sources of tsunami and tsunamigenic earthquakes in subduction zones. *Pure and Applied Geophysics*, *154*(3–4), 467–483. https://doi.org/10.1007/s000240050240

Schmedes, J., Archuleta, R. J., & Lavallée, D. (2010). Correlation of earthquake source parameters inferred from dynamic rupture simulations. *Journal of Geophysical Research: Solid Earth*, *115*(B3), 2009JB006689. https://doi.org/10.1029/2009JB006689

Shaw, B. E., Fry, B., Nicol, A., Howell, A., & Gerstenberger, M. (2022). An earthquake simulator for New Zealand. *Bulletin of the Seismological Society of America*, *112*(2), 763–778. https://doi.org/10.1785/0120210087

Shaw, B. E., Milner, K. R., Field, E. H., Richards-Dinger, K., Gilchrist, J. J., Dieterich, J. H., & Jordan, T. H. (2018). A physics-based earthquake simulator replicates seismic hazard statistics across California. *Science Advances*, *4*(8), 0688. https://doi.org/10.1126/sciadv.aau0688

Shea, H. N., & Barnhart, W. D. (2022). The Geodetic Centroid (gCent) Catalog: Global Earthquake Monitoring with Satellite Imaging Geodesy. *Bulletin of the Seismological Society of America*, *112*(6), 2946–2957. https://doi.org/10.1785/0120220072

Small, D. T., & Melgar, D. (2023). Can stochastic slip rupture modeling produce realistic M9+ events? *Journal of Geophysical Research: Solid Earth*, *128*(3), 2022 025716. https://doi.org/10.1029/2022JB025716

Solares-Colón, M. M. (2019). *New constraints on crustal deformation within the Puerto Rico-Virgin Islands microplate using two decades of GPS data* [M.Sc. Thesis]. University of Puerto Rico at Mayagüez.

Solares-Colón, M. M., Goldberg, D. E., Melgar, D., Vanacore, E. A., Sahakian, V. J., & Yeck, W. L. (2024). *Supporting information for the 2020 Mw 6.4 southwestern Puerto Rico mainshock source model* [Dataset]. U.S. Geological Survey data release. https://doi.org/10.5066/P1VBFP8B

Solares-Colón, M. M., Goldberg, D. E., Melgar, D., Vanacore, E. A., Sahakian, V. J., Yeck, W. L., Hernández, F., & López-Venegas, A. M. (2025). Slow Rupture, Long Rise Times, and Multi-Fault Geometry: The 2020 M6.4 Southwestern Puerto Rico Mainshock. *Geophysical Research Letters*, *52*(8), e2024GL109740. https://doi.org/10.1029/2024GL109740

Solares-Colón, M. M., Melgar, D., Howell, A., Crowell, B., D'Anastasio, E., Caballero, E., & Fry, B. (2025). *Using ruptures from earthquake cycle simulators to test geodetic early warning systems performance (supplementary data)* [Dataset]. Zenodo. https://doi.org/10.5281/zenodo.15522298

Somala, S. N., Ampuero, J.-P., & Lapusta, N. (2014). Resolution of Rise Time in Earthquake Slip Inversions: Effect of Station Spacing and Rupture Velocity. *Bulletin of the Seismological Society of America*, *104*(6), 2717–2734. https://doi.org/10.1785/0120130185

Somerville, P., Irikura, K., Graves, R., Sawada, S., Wald, D., & Abrahamson, N. (1999). Characterizing crustal earthquake slip models for the prediction of strong ground motion. *Seismological Research Letters*, *70*(1), 59–80. https://doi.org/10.1785/gssrl.70.1.59

Stirling, M., Fitzgerald, M., Shaw, B., & Ross, C. (2024). New magnitude–area scaling relations for the New Zealand National Seismic Hazard Model 2022. *Bulletin of the Seismological Society of America*, *114*(1), 137–149. https://doi.org/10.1785/0120230114

Suhendi, C., Li, B., Vasyura-Bathke, H., Liu, J., Jónsson, S., & Mai, P. M. (2024). Bayesian inversion and quantitative comparison for bilaterally quasi-symmetric rupture processes on a multisegment fault in the 2021 *Mw* 7.4 Maduo earthquake. *Geophysical Journal International*, *240*(1), 673–695. https://doi.org/10.1093/gji/ggae398

Thompson Jobe, J. A., Briggs, R., Hughes, K. S., Joyce, J., Gold, R., & Mahan, S. (2024). *Datasets documenting neotectonic mapping of Puerto Rico* [Dataset]. U.S. Geological Survey data release. https://doi.org/10.5066/P13KZZAZ

Tian, D., Uieda, L., Leong, W. J., Fröhlich, Y., Schlitzer, W., Grund, M., Jones, M., Toney, L., Yao, J., Magen, Y., Tong, J.-H., Materna, K., Belem, A., Newton, T., Anant, A., Ziebarth, M., Quinn, J., & Wessel, P. (2024). *PyGMT: A Python interface for the Generic Mapping Tools (v0.12.0* [Software]. Zenodo. https://doi.org/10.5281/zenodo.11062720

Uphoff, C., May, D. A., & Gabriel, A.-A. (2023). A discontinuous Galerkin method for sequences of earthquakes and aseismic slip on multiple faults using unstructured curvilinear grids. *Geophysical Journal International*, *233*(1), 586–626. https://doi.org/10.1093/gji/ggac467

Vargas, G., Farías, M., Carretier, S., Tassara, A., Baize, S., & Melnick, D. (2011). Coastal uplift and tsunami effects associated with the 2010 Mw8.8 Maule earthquake in central Chile. *Andean Geology*, *38*(1), 219–238.

Vasyura-Bathke, H., Dettmer, J., Steinberg, A., Heimann, S., Isken, M. P., Zielke, O., Mai, P. M., Sudhaus, H., & Jónsson, S. (2020). The Bayesian Earthquake Analysis Tool. *Seismological Research Letters*, *91*(2A), 1003–1018. https://doi.org/10.1785/0220190075

Vera, F., Carrillo-Ponce, A., Crosetto, S., Kosari, E., Metzger, S., Motagh, M., Liang, Y., Lyu, S., Petersen, G., Saul, J., Sudhaus, H., Symmes-Lopetegui, B., Than, O., Xiao, H., & Tilmann, F. (2025). Supershear Rupture Along the Sagaing Fault Seismic Gap: The 2025 Myanmar Earthquake. *The Seismic Record*, *5*(3), 289–299. https://doi.org/10.1785/0320250025

Viltres, R., Nobile, A., Vasyura-Bathke, H., Trippanera, D., Xu, W., & Jónsson, S. (2022). Transtensional rupture within a diffuse plate boundary zone during the 2020 Mw 6.4 Puerto Rico earthquake. *Seismological Research Letters*, *93*(2A), 567–583. https://doi.org/10.1785/0220210261

Wald, D. J., Quitoriano, V., Worden, C. B., Hopper, M., & Dewey, J. W. (2012). USGS "Did You Feel It?" Internet-based macroseismic intensity maps. *Annals of Geophysics*, *54*(6), 688–707. https://doi.org/10.4401/ag

Wallace, L. M. (2020). Slow slip events in New Zealand. *Annual Review of Earth and Planetary Sciences*, *48*(1), 175–203. https://doi.org/10.1146/annurev-earth-071719-055104

Wang, Y., & Day, S. M. (2017). Seismic source spectral properties of crack-like and pulse-like modes of dynamic rupture. *Journal of Geophysical Research: Solid Earth*, *122*(8), 6657–6684. https://doi.org/10.1002/2017JB014454

Wei, S., Wang, X., Li, C., Zeng, H., Ma, Z., Shi, Q., Chen, H., Huang, Y., Lyu, M., Liao, J., Yang, S., Bai, Y., Maung, P. M., Oo, K., Htwe, Y. M. M., Zhang, J., Dal Zilio, L., Shan, X., & Chen, L. (2025). Supershear rupture sustained through a thick fault zone in the 2025 M_w 7.8 Mandalay earthquake. *Science*, *390*(6772), 468–475. https://doi.org/10.1126/science.adz2101

Weilert, L., & Laó-Dávila, D. A. (2023). Fault structure and segmentation of the Punta Montalva fault in southwestern Puerto Rico using high- resolution digital elevation models. *Tectonophysics*, *860*, 229921. https://doi.org/10.1016/j.tecto.2023.229921

Williams, C. A., Eberhart-Phillips, D., Bannister, S., Barker, D. H. N., Henrys, S., Reyners, M., & Sutherland, R. (2013). Revised interface geometry for the Hikurangi Subduction Zone, New Zealand. *Seismological Research Letters*, *84*(6), 1066–1073. https://doi.org/10.1785/0220130035

Williamson, A. L., Melgar, D., Crowell, B. W., Arcas, D., Melbourne, T. I., Wei, Y., & Kwong, K. (2020). Toward near-field tsunami forecasting along the Cascadia subduction zone using rapid GNSS source models. *Journal of Geophysical Research: Solid Earth*, *125*(8), 2020 019636. https://doi.org/10.1029/2020JB019636

Xu, L., Meng, L., Yunjun, Z., Yang, Y., Wang, Y., Hu, C., Weng, H., Xu, W., Su, E., & Ji, C. (2025). Bimaterial effect and favorable energy ratio enabled supershear rupture in the 2025 Mandalay earthquake. *Science*, *390*(6772), 476–481. https://doi.org/10.1126/science.ady6100

Ye, L., Lay, T., & Kanamori, H. (2025). The 28 March 2025 Mw 7.8 Myanmar Earthquake: Preliminary Analysis of an ~480 km Long Intermittent Supershear Rupture. *The Seismic Record*, *5*(3), 260–269. https://doi.org/10.1785/0320250021

Ye, L., Lay, T., Kanamori, H., & Rivera, L. (2016a). Rupture characteristics of major and great ($M_w \geq 7.0$) megathrust earthquakes from 1990 to 2015: 1. Source parameter scaling relationships. *Journal of Geophysical Research: Solid Earth*, *121*(2), 826–844. https://doi.org/10.1002/2015JB012426

Ye, L., Lay, T., Kanamori, H., & Rivera, L. (2016b). Rupture characteristics of major and great (Mw ≥ 7.0) megathrust earthquakes from 1990 to 2015: 2. *Depth Dependence. Journal of Geophysical Research: Solid Earth*, *121*(2), 845–863. https://doi.org/10.1002/2015JB012427

Yoon, C. E., Cochran, E. S., Vanacore, E. A., Huerfano, V., Báez-Sánchez, G., Wilding, J. D., & Smith, J. (2023). A detailed view of the 2020– 2023 southwestern Puerto Rico seismic sequence with deep learning. *Bulletin of the Seismological Society of America*, *113*(6), 2377–2415. https://doi.org/10.1785/01202202

Yue, H., Lay, T., Rivera, L., An, C., Vigny, C., Tong, X., & Báez Soto, J. C. (2014). Localized fault slip to the trench in the 2010 Maule, Chile (Mw 8.8) earthquake from joint inversion of high-rate GPS, teleseismic body waves, InSAR, campaign GPS, and tsunami observations. *Journal of Geophysical Research: Solid Earth*, *119*(10), 7786–7804. https://doi.org/10.1002/2014JB011340

Zhu, L., & Rivera, L. A. (2002). A note on the dynamic and static displacements from a point source in multilayered media: A note on the dynamic and static displacements from a point source. *Geophysical Journal International*, *148*(3), 619–627. https://doi.org/10.1046/j.1365-246X.2002.01610.x

Zielke, O., & Mai, P. M. (2023). MCQsim: A multicycle earthquake simulator. *Bulletin of the Seismological Society of America*, *113*(3), 889–908. https://doi.org/10.1785/0120220248